PLANET MIGRATION AROUND YOUNG MAGNETIZED STARS

A Dissertation

Presented to the Faculty of the Graduate School

of Cornell University

in Partial Fulfillment of the Requirements for the Degree of

Doctor of Philosophy

by

Megan Louise Comins

August 2015

© 2015 Megan Louise Comins
ALL RIGHTS RESERVED

PLANET MIGRATION AROUND YOUNG MAGNETIZED STARS

Megan Louise Comins, Ph.D.

Cornell University 2015

We investigate the migration of low-mass planets ($5M_\oplus$ and $20M_\oplus$) in accretion disks threaded with a magnetic field using a 2D magnetohydrodynamic (MHD) code in polar coordinates. We observed that, in the case of a strong azimuthal magnetic field where the plasma parameter is $\beta \sim 1 - 2$, density waves at the magnetic resonances exert a positive torque on the planet and may slow down or reverse its migration. However, when the magnetic field is weaker (i.e., the plasma parameter β is relatively large), then non-axisymmetric density waves excited by the planet lead to growth of the radial component of the field and, subsequently, to development of the magneto-rotational instability, such that the disk becomes turbulent. Migration in a turbulent disk is stochastic, and the migration direction may change as such. To understand migration in a turbulent disk, both the interaction between a planet and individual turbulent cells, as well as the interaction between a planet and ordered density waves, have been investigated.

BIOGRAPHICAL SKETCH

Megan Comins was born in Pontiac, Michigan on August 12, 1984. From there, she lived in Madison Heights, Waterford, and finally Oxford (all in Michigan). From a young age, she was active in music, playing piano, clarinet and bassoon by the time she finished high school. She was in the color guard in marching band, played in the pit band, and briefly participated in a youth orchestra in Southeast Michigan. Understandably, until her junior year of high school, she planned to attend music school. Then, she took a physics course for the first time with Kimberly DeBroka, and her life changed. She graduated with highest honors from Oxford High School in 2003, with plans to major in physics.

From there, she attended college at The Ohio State University in Columbus, Ohio from 2003-2008. She majored in physics and astronomy and gained a solid appreciation for football. Though she had taken Japanese classes at Oakland University for two years while in high school, she chose to minor in Russian language instead of passing on her language requirement. She was unhappy with the lack of research options available in the Astronomy Department and, in 2005, formed The Ohio State University Astronomical Society (OSUAS) with other undergraduates and with the blessing of the new department chair, Prof. Bradley Peterson. Between 2005 and 2008, several "town hall" style meetings were held where the undergraduate majors could discuss things with the department. A summer research program for OSU undergraduate majors was started in the summer of 2007, and an annual lecture was established that took into account the input of the undergraduates in the department.

Also as an undergraduate, Megan worked on two research projects. She worked in both the Nuclear Theory Group in the Physics Department under

Prof. Robert Perry, as well as under Prof. Peterson in the Astronomy Department. She ultimately graduated in June 2008 with two BS degrees, one in astronomy and one in physics, both Cum Laude and With Honors. She earned With Research Distinction in Astronomy for her work with Prof. Peterson, presenting an undergraduate thesis titled "Systematic Errors in Black Hole Mass Measurement Using Reverberation Mapping."

She went on to attend Pennsylvania State University's Astronomy & Astrophysics PhD program from 2008-2010, where she worked with Prof. Niel Brandt studying the X-ray properties of quasars. While there, she was an active member of the Nu Chapter of Graduate Women in Science (GWIS), she became Chair-Elect of the Forum on Graduate Student Affairs of the American Physical Society (APS), and she lobbied Congress for science funding with the APS. She then transferred to Cornell University to finish her PhD working in the Plasma Astrophysics Group under Prof. Richard Lovelace and Dr. Marina Romanova; she earned her MS in Astronomy in 2011. She acted as Chair and Past Chair of the APS Forum on Graduate Student affairs, and she served as President of the re-established Alpha Chapter of GWIS for several years, planning the 2011 90th Anniversary GWIS Meeting in Ithaca, NY.

She has been working as a programmer and project manager at Aperion Information Technologies, Inc., since February 2014. Following finishing her PhD at Cornell, she will become a mother in October 2015 and continue working at Aperion.

Dedicated to John Mergo and to our daughter, who we will meet in October.

ACKNOWLEDGEMENTS

First and foremost, I must thank Dr. Marina Romanova. Her constant support and encouragement were vital to both my progress in research and my well-being. Furthermore, her flexibility in allowing me to study Computer Science for my minor significantly supported my personal career desires, regardless of whether they were academic or not. Working with her and Prof. Richard Lovelace was the highlight of my 24 years of education. Furthermore, I must thank the other members of my research group, Dr. Patrick Lii and Dr. Sergei Dyda, for useful and enlightening discussions as well as well-deserved distractions from work.

I must also thank our Russian collaborators, Dr. Aleksandr Koldoba and Dr. Galina Ustyugova, for their work on both the simulation and analysis code, as well as their input on written work. Their expertise has been invaluable, and it has been my privilege to work with them.

While the list of people who have influenced me throughout my life is a long one, there are a few people who deserve special mention. My parents (Mark and Patricia Comins and Dawn Delong) and my siblings (Michael Staggs, Jessica Comins, and Stephen Comins) listened to my frustrations and encouraged me to not give up. They asked me about my research even if they didn't quite understand the details. My cousin, Jonathan Delong, constantly encouraged me to be the first in our family to graduate with a PhD. My high school physics teacher, Ms. Kim DeBroka, started me on a scientific and technical career path. Prof. Bradley Peterson and Prof. Robert Perry introduced me to research and provided me with much-needed mentoring as an undergraduate. Prof. Steinn Sigurdsson provided me with mentoring and support while I was at Penn State.

There were many friends who were and continue to be a valuable source

of support, including (but not limited to): Sharon Xuesong Wang, Emily Zur Linden, Samantha Houser, Jason Young, Amanda Lundberg, Sara Gettel, Brendan Mullan, Kamen Todorov, Tim Reber, Zach Lamberty, Joyce Byun, Brian Leahy, Alina and Bryan O'Connell, Lauren Jackson, Lena Bartell, Jil Szewski, Matt Warkentin, Garrett Elliott, Edward Golowacz, Jeanette Nguyen, Michael Roman, Dustin Madison, Jennifer Boggs, Paul Mergo, and Kimberly Niehaus.

Finally, I thank my partner in life, John Mergo. Since 2007, he has been a constant source of emotional, intellectual, and professional support, as well as a frequent supplier of fun and humor. I look forward to the future with him, our child(ren), and our four cats (Scipy, Numpy, Bit, and Wrex).

TABLE OF CONTENTS

CHAPTER 1

INTRODUCTION

In 1995, our understanding of the formation of planetary systems changed with the discovery of 51 Pegasi b (51 Peg b), which was the first exoplanet detection around a Solar-type star that withstood scrutiny. 51 Pegasi is a G dwarf, like the Sun, with $M_{51\text{ Peg}} \approx 1M_{\odot}$ and $R_{51\text{ Peg}} \approx 1R_{\odot}$. In 1995, the mass of 51 Peg b was constrained within $0.5 - 2M_{\text{Jup}}$; this mass estimate was updated to $0.5M_{\text{Jup}}$ in 1997. This mass places 51 Peg b within the realm of giant planets, and its orbital radius was determined to be only 0.05 AU, which is well within the orbital radius of Mercury about the Sun. As a result, 51 Peg b became the first planet to be known as a "hot Jupiter" (Mayor and Queloz 1995; Marcy et al. 1997).

Since then, especially thanks to the Kepler satellite, many more extrasolar planetary systems have been observed that are very different from our Solar System. A particularly good example of this is the Kepler-11 system. Kepler was designed to detect planets around Solar-type stars, and Kepler-11 is like 51 Peg, with an approximately Solar mass and radius. The Kepler-11 system has 6 planets, all of which orbit within Venus's orbital radius, and five of which orbit within Mercury's orbital radius. The masses of the planets in the Kepler-11 system are estimated to be between a few and 10 Earth masses (Lissauer et al. 2011, 2013).

A histogram showing the distribution of all exoplanets whose semimajor axes lie between 0.1 and 10 AU (as of July 12, 2015) is shown below in Fig. 1.1 (Wright et al. 2011). There are noticeable peaks in the distribution near 0.05 AU and near 1 AU. When considering planets with $M_{\text{p}} > 1M_{\text{Jup}}$, these peaks still exist, though the strength of the peak near 0.05 AU is diminished. The existence

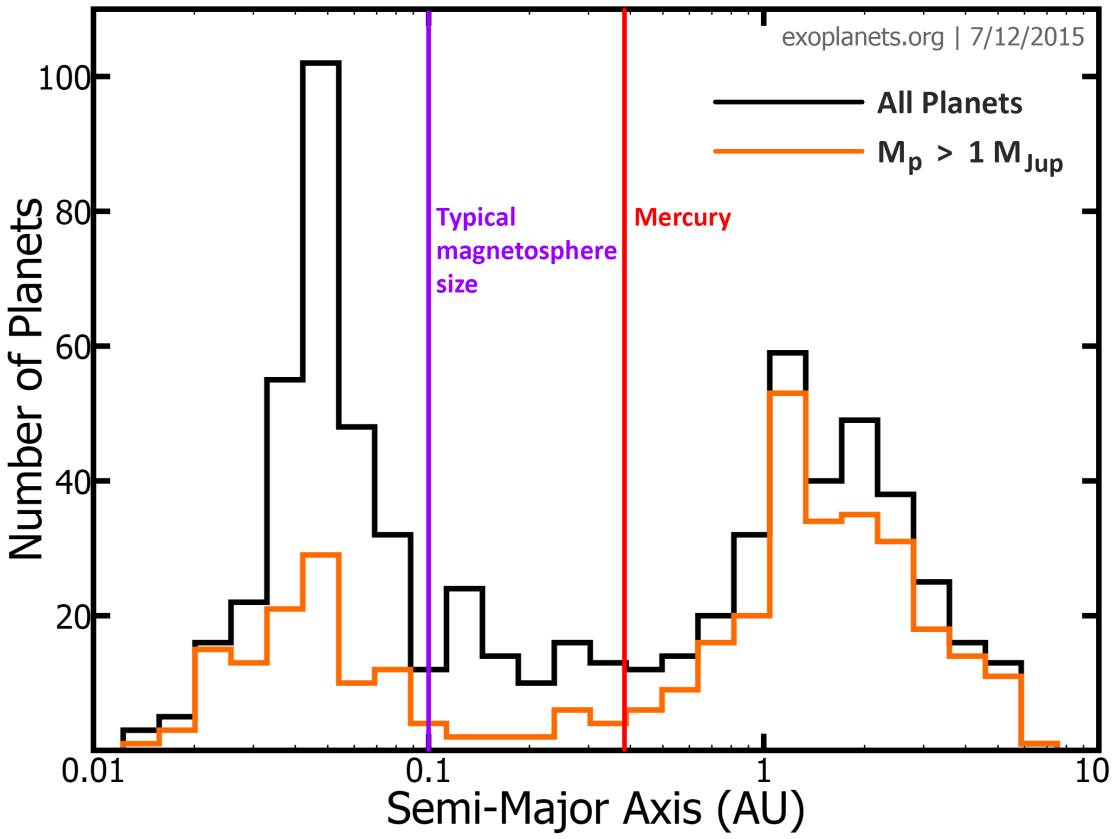

Figure 1.1 Semimajor axis distribution of confirmed planet observations as of July 12, 2015. The black line shows the histogram for all planets; the orange line shows the histogram for planets with $M_p \sin i > 1 M_{Jup}$. $M \sin i$ is a measure of the minimum mass of the planet, where i is the planet's orbital inclination. The purple line shows the typical size of a young stellar magnetosphere. The red line shows the semimajor axis of Mercury for reference.

of close-in planets, such as 51 Peg b and those in the Kepler-11 system, does not appear to be an anomaly, but instead to be a common occurrence.

The existence of these planets, especially close-in giant planets like hot Jupiters, is troublesome. First, the temperature in a protoplanetary disk at such small radii exceeds 1000 K, which is far too hot to allow for *in situ* formation of these planets (Armitage and Rice 2008; Armitage 2010, 2011). This implies

that the planets must form at larger distances from their host stars and migrate inward to their observed orbital radii. Goldreich and W.R. (1973) and Goldreich and Tremaine (1979, 1980) showed that the interaction between the planet and the gaseous protoplanetary disk should always drive planet migration: the planet excites density waves in the disk at the disks Lindblad resonances that exert a torque on the planet, causing it to lose angular momentum and migrate inward This inward migration mechanism does not fully explain the observed locations of close-in giant planets, however. Specifically, the inward migration time scale for giant planets is $\sim 10^5$ years, which is shorter than both the disk lifetime and the required formation time for giant planets according to the core accretion model of planet formation (Armitage 2010, 2011).

To discern other sources of torque that could also affect planet migration, consider the environment in which these planets form. Young Solar-type stars have extremely strong magnetic fields: $B_\oplus \approx 0.5$ G, $B_\odot \approx 1$ G, and $B_\star \approx 1 - 5$ kG (e.g., Basri et al. 1992; Johns-Krull et al. 1999; Feigelson and Montmerle 1999; Johns-Krull and Valenti 2000; Gregory et al. 2010). This magnetic field opens a low-density gap in the disk around the star whose extent is determined by balancing the magnetic and matter pressures; the matter pressure consists of a combination of ram and thermal pressure in the disk: $P_{\rm mag} = P_{\rm ram} + P_{\rm thermal}$. The size of this magnetospheric gap, for a typical young Solar-type star, is $r_m \approx 0.1$ AU (also shown in Fig. 1.1). This implies that, not only are many planets orbiting too close to their host stars to have formed *in situ*, they are also orbiting within the extent of what was their host stars magnetosphere during the time when the gas disk was present. The interaction between the stellar magnetosphere and the protoplanetary disk is complicated (e.g., Goldreich and Tremaine 1978; Lubow 1981; Lai 1999; Terquem and Papaloizou 2000; Lai and Zhang 2008; Kato

2004, 2007, 2010; Meheut and Tagger 2009), and it can change the structure of the protoplanetary gas disk substantially. As a result, the mechanisms driving planetary migration can be substantially altered by the stellar magnetic field and should not be ignored when calculating the sources of torque on a forming and migrating protoplanet.

To this end, I worked with others in our research group on modifying our existing MHD simulation code that has been used to study varied physical processes around magnetized stars (see, e.g., Koldoba et al. 2002; Romanova et al. 2002, 2003a,b, 2004, 2008, 2011, 2012, 2013; Long et al. 2007, 2008, 2011; Ustyugova et al. 2006; Lii et al. 2014; Dyda et al. 2015; Koldoba et al. 2015 and references therein) to include a module for calculating a planet's orbital evolution within the MHD disk. I will first briefly outline the theory behind planet migration, including the sources of torque in both hydrodynamic and MHD disks. Following this, I will describe the code and the new planetary module. Finally, I will describe results from the first simulations with this new planetary module in two dimensions (Comins et al. 2015).

CHAPTER 2

PLANET MIGRATION THEORY

2.1 Migration Mechanisms

A planet's orbit can evolve as it interacts with its environment, both during and after the planet has formed. As its environment changes, so do the ways in which the planet's orbital evolution can occur (Armitage 2007). These interactions can include, but are not limited to:

1. Interaction between the planet and its gaseous protoplanetary disk, which results in angular momentum exchange between the disk and the planet occurs for both low-mass and high-mass planets (Goldreich and Tremaine 1980). The gas disk can be around while the planet is still forming.
2. Interaction between the planet and its remnant planetesimal disk, which results in angular momentum exchange between the planet and planetesimals that are left over after the planets are done forming. This mechanism is likely more important for high-mass than for low-mass planets, and there is evidence that this interaction could have caused orbital migration of the ice giants and possibly Saturn in our Solar System (Levison et al. 2007).
3. Planet-planet scattering, occurring between the planet and the other bodies orbiting unstably in the newly-formed planetary system. This has been suggested as the origin for the observed eccentric orbits of some exoplanetary systems (Lin and Ida 1997; Rasio and Ford 1996; Weidenschilling and Marzari 1996).

4. Interaction between the planet and a stellar binary companion that is significantly misaligned with that of the planet, which results in eccentricity excitation via the Kozai-Lidov mechanism (Kozai 1962; Lidov 1962). This interaction can drive the eccentricity high enough that energy is tidally dissipated upon the planet's closest approach to the star, possibly circularizing the orbit and providing a way to explain hot Jupiters as well (Wu and Murray 2003).

2.2 Migration Regimes

There are two primary migration regimes within a gaseous protoplanetary disk, delineated by the planet mass relative to that of the local disk (Ward 1997). Fig. 2.2 shows results from simulations done by Armitage and Rice (2008), highlighting the differences between these two regimes.

Type I migration occurs when the planets mass is low enough (generally $\sim M_{\oplus}$) that the interaction between the planet and the disk is relatively weak. The overall surface density profile of the disk remains relatively unchanged, although spiral density waves are excited by the planet, and angular momentum is exchanged between the disk and the planet. The migration timescale in this regime is very short, roughly 0.5 Myr for a typical protoplanetary disk (Armitage 2007).

Type II migration occurs when the planet is massive enough to open a gap in the disk, because the planets Hill radius exceeds the scale height of the disk.

The Hill radius is defined as

$$R_H = r_\mathrm{p}\left(\frac{M_\mathrm{p}}{3M_\star}\right)^{1/3}, \tag{2.1}$$

where $M_\star$ is the mass of the central star, M_p is the mass of the planet, and r_p is the orbital radius of the planet (assuming a circular orbit). This typically occurs for planet masses $\sim M_\mathrm{Saturn} - M_\mathrm{Jup}$ (Armitage 2007). Furthermore, the planet must be able to clear material from the gap faster than the disk can refill it. Once the gap is opened and is able to remain open, the planet's orbital evolution is coupled with the viscous evolution of the disk (Goldreich and Tremaine 1980; Lin and Papaloizou 1980; Papaloizou and Lin 1984).

2.3 Planet Migration in a Hydrodynamic Disk

In the absence of a magnetic field in the disk, the migration of the planet is determined by the Lindblad and corotation torques (Goldreich and Tremaine 1979; Ward 1986, 1997).

To calculate the torque from the Lindblad resonances, assume that the planet revolves about the star in a circular orbit with a period $P = 2\pi/\Omega_\mathrm{p}$, where Ω_p is the angular orbital frequency of the planet. The planet excites m waves in the disk with "orbital" frequencies

$$\omega = m\Omega_\mathrm{p}. \tag{2.2}$$

The dispersion relation for these waves is

$$(\omega - m\Omega)^2 = \kappa^2, \tag{2.3}$$

where $\Omega = \Omega(r)$ is the angular frequency of the disk rotation at radius r, $\omega - m\Omega$ is the Doppler-shifted frequency of the mth wave as seen by an observer orbiting

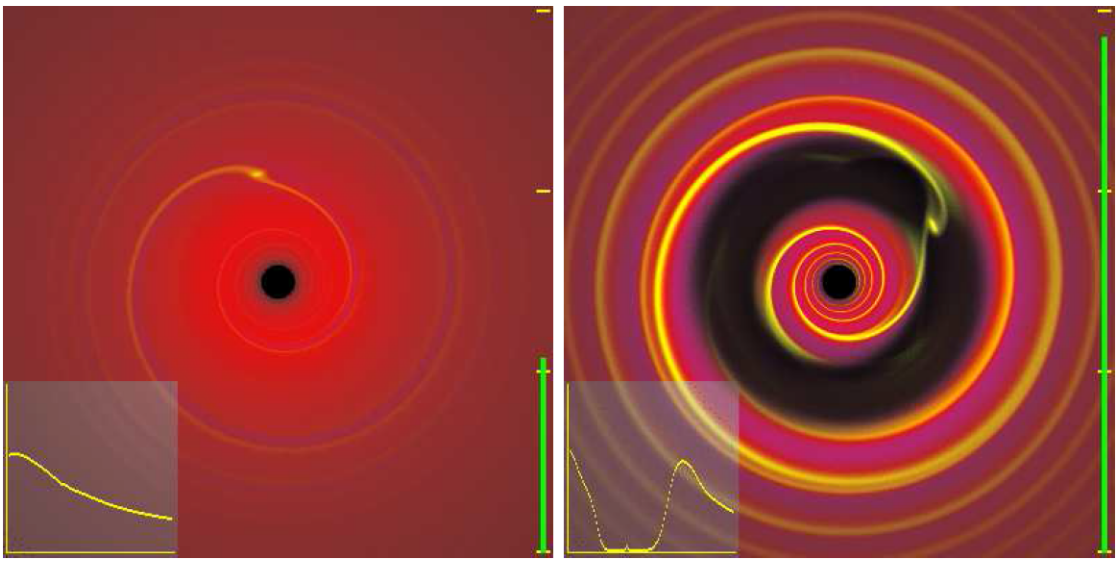

Figure 2.1 Simulations from Armitage and Rice (2008) showing the planet-disk interaction in a non-turbulent hydrodynamic disk with a locally isothermal equation of state; the planet is on a fixed circular orbit. *Left Panel:* An illustration of type I migration regime, in which a low-mass planet excites spiral density waves in the disk but does not significantly perturb the overall disk density profile (as seen in the inset graph). *Right Panel:* An illustration of type II migration regime, in which a $10 M_{\rm Jup}$ planet opens a gap in the disk and the overall density profile in the disk is significantly altered (as seen in the inset graph).

at the angular speed of the disk, and $\kappa = \Omega_{\rm Kep}$ is the epicyclic frequency in a Keplerian disk. Combining Eqn. 2.2 and Eqn. 2.3,

$$m^2 \left(\Omega - \Omega_{\rm p}\right)^2 = \kappa^2. \tag{2.4}$$

Substituting $\Omega(r) = \sqrt{GM_\star/r^3}$ and $\Omega_{\rm p} = \sqrt{GM_\star/r_{\rm p}^3}$, the locations of the Lindblad resonances are

$$r_{\rm LR} = r_{\rm p}\left(\frac{m \pm 1}{m}\right)^{2/3}. \tag{2.5}$$

For each value of m (except $m = 1$), there is one resonance located closer to (farther from) the star than the planet called the inner (outer) Lindblad resonance, denoted ILR (OLR). The ILRs exert a positive torque on the planet, pushing the

planet outward, while the OLRs exert a negative torque on the planet and push the planet inward. The torques exerted on the planet from each ILR and OLR are different in magnitude and opposite in sign; the sum of these torques is called the "differential Lindblad torque." In the absence of other torques, the sign of the differential Lindblad torque indicates the direction of migration. In general, this torque is negative and results in overall inward migration of the planet (e.g., Armitage 2010; Kley and Nelson 2012).

However, there is typically a corotation torque exerted on the planet as well. A corotation resonance exists in the disk where $\Omega = \Omega_p$. In an two-dimensional isothermal disk, both the magnitude and sign of the corotation torque depend on the gradient of the surface density at the corotation radius (Goldreich and Tremaine 1979; Tanaka et al. 2002; Armitage 2007):

$$T_{\rm CR} \propto \frac{d}{dr}\left(\frac{\Sigma}{B}\right), \tag{2.6}$$

where B is the Oort parameter characterizing the local rotation properties of the disk,

$$B(r) = \Omega + \frac{r}{2}\frac{d\Omega}{dr}. \tag{2.7}$$

Explaining the torque due to the corotation resonances is not as straightforward as for the Lindblad resonances. As such, the physics of the corotation torque and its effect on planet migration has been studied by number of authors (e.g., Paardekooper and Mellema 2006; Baruteau and Masset 2008; Paardekooper and Papaloizou 2008; Kley et al. 2009; Masset and Casoli 2009, 2010; Paardekooper et al. 2010, 2011).

Tanaka et al. (2002) calculated the cumulative action of the differential Lindblad and corotation torques from the planet on the disk in two- and three-dimensional semi-analytical calculations and obtained the torque from the

planet on the disk in the forms:

$$\Gamma_{\text{total,3D}} = -(1.364 + 0.541\alpha)\left(\frac{M_\text{p}}{M_\star}\frac{r_\text{p}\Omega_\text{p}}{c_s}\right)^2 \Sigma(r_\text{p}) r_\text{p}^4 \Omega_\text{p}^2 \tag{2.8}$$

$$\Gamma_{\text{total,2D}} = -(1.160 + 2.828\alpha)\left(\frac{M_\text{p}}{M_\star}\frac{r_\text{p}\Omega_\text{p}}{c_s}\right)^2 \Sigma(r_\text{p}) r_\text{p}^4 \Omega_\text{p}^2, \tag{2.9}$$

where α defines the slope of the density distribution ($\Sigma \propto r^{-\alpha}$), and c_s is the isothermal sound speed in the disk at the orbital radius of the planet. This implies that the total torque on the planet in a two-dimensional disk is zero when $\alpha = -0.41$, suggesting that

1. the torque on the planet is positive, and the planet migrates outward, when $\alpha < -0.41$;
2. the torque on the planet is zero, and the planet's migration halts, when $\alpha = -0.41$; and
3. the torque on the planet is negative, and the planet migrates inward, when $\alpha > -0.41$.

2.4 Planet Migration in a Laminar MHD Disk

In strongly magnetized laminar disks, magnetic waves can be excited, and the torques associated with these magnetic waves can affect the planet's migration. (e.g., Terquem 2003; Fromang et al. 2005; Fu and Lai 2011). Terquem (2003) investigated the propagation of waves in a magnetized disk in which the magnetic field is purely azimuthal and found that there are two singular radii at which the frequency perturbation in a frame rotating with the fluid matches that of a slow MHD wave propagating along the field lines; these radii define the locations of the magnetic resonances. The inner and outer magnetic resonances are

denoted similarly to Lindblad resonances, with the inner magnetic resonances $r_{\rm IMR} < r_{\rm p}$, and the outer magnetic resonances $r_{\rm OMR} > r_{\rm p}$. Terquem (2003) derived the following dispersion relation:

$$m^2(\Omega - \Omega_{\rm p})^2 = \frac{m^2 c_s^2 v_{\rm A}^2}{r^2(v_A^2 + c_s^2)}. \tag{2.10}$$

Here, $v_{\rm A}$ is the Alfvén speed, given by Terquem (2003) as $v_{\rm A}^2 = \langle B^2 \rangle / 4\pi\Sigma$, where $\langle B^2 \rangle = \int B^2 dz$ is the vertically-integrated square of the magnetic field. The sound speed $c_s^2 = d\langle P \rangle / d\Sigma$, where $\langle P \rangle = \int P dz$. Terquem (2003) determines the strength of the magnetic field via $\beta_{v_a} = c_s^2 / v_A^2$, which is evaluated at the location of the planet. [1]

The locations of the resonances when the disk is Keplerian ($\Omega \approx \Omega_{\rm K}$) and thin ($H/r \ll 1$) are given by

$$|r_M - r_{\rm p}| = \frac{2H}{3\sqrt{1 + \beta_{v_A}}}, \tag{2.11}$$

where the thickness of the disk H and the plasma parameter $\beta_{v_A} = c_s^2 / v_A^2$ are evaluated at $r = r_{\rm p}$. As the field becomes weaker (i.e., $\beta_{v_A} \to \infty$), the magnetic resonances converge toward the corotation radius. We suggest that $c_s/(r\Omega) \approx H/r$ and find the position of the inner and outer magnetic resonances to be

$$r_{\rm IMR} = r_{\rm p} - \frac{2H}{3\sqrt{1 + \beta_{v_A}}}, \quad r_{\rm OMR} = r_{\rm p} + \frac{2H}{3\sqrt{1 + \beta_{v_A}}}. \tag{2.12}$$

A schematic showing the positions of the $m = 1$ and $m = 2$ Lindblad resonances relative to the positions of the magnetic resonances is shown in Fig. 2.2. Terquem (2003) showed that the waves associated with the magnetic resonances can exert a positive torque on the planet that is larger in magnitude than the differential Lindblad torque if the magnetic field increases steeply toward the star.

[1] In our simulations, we use the standard definition of the plasma parameter, $\beta = 2\beta_{v_A} = 8\pi P / B^2$, where P and B are the pressure and magnetic field in the disk, respectively.

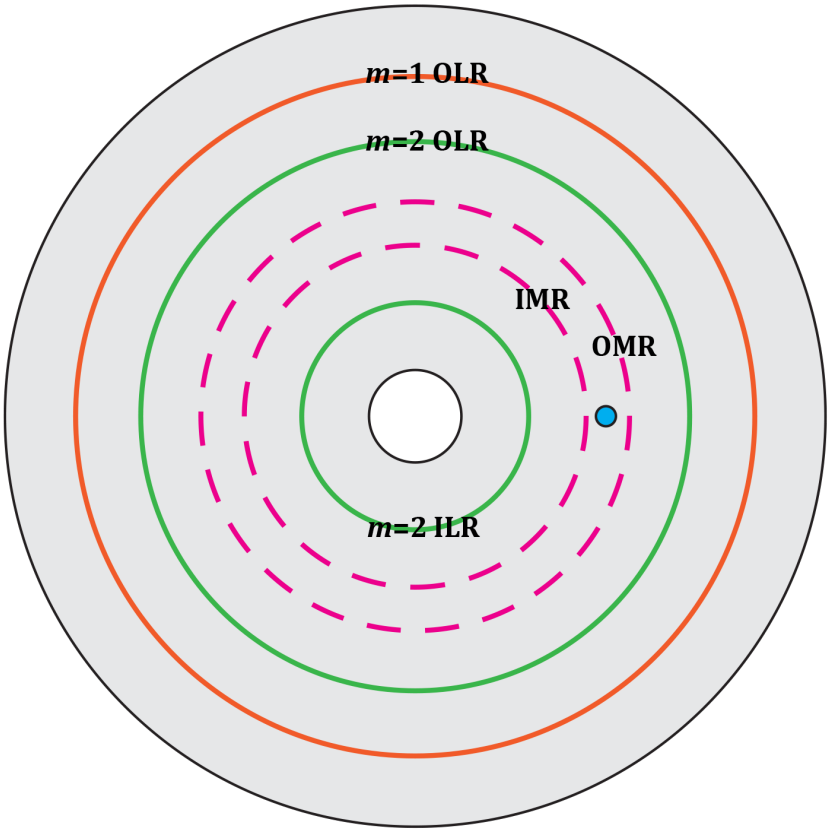

Figure 2.2 Schematic showing the locations of the $m = 1$ and $m = 2$ Lindblad resonances relative to the magnetic resonances. The planet is the blue circle. The magenta dashed lines indicate the Inner Magnetic Resonance (IMR) and Outer Magnetic Resonance (OMR). The orange solid line indicates the $m = 1$ Outer Lindblad Resonance (OLR). The green solid lines indicate the $m = 2$ Inner Lindblad Resonance (ILR) and OLR.

Fromang et al. (2005) performed simulations of a planet's migration in a magnetized disk and found that the magnetic resonances can slow or stop the migration of a planet. In particular, they investigated the migration of a $5M_\oplus$ planet embedded in a disk that is threaded with an azimuthal magnetic field with $B_\varphi \propto r^{-k}$ with Σ = const initially. They took an initial value of $\beta_{v_a} = 2$ at the planet's location and found that, depending on the steepness of the magnetic field distribution (defined by k), the planet's migration slowed or reversed in

direction. Later, Guilet et al. (2013) studied the effects of an MHD corotation torque on a low-mass planet in a 2D laminar disk with a weak azimuthal field threading the disk. The field was not strong enough to generate an appreciable torque from magnetic resonances, and it was not strong enough to dominate the hydrodynamic corotation torques, but a "torque excess" attributed to the presence of the magnetic field was found.

2.5 Planet Migration in a Turbulent MHD Disk

Work done by Baruteau et al. (2011) and Uribe et al. (2011) showed the existence of additional MHD corotation torques in MRI-turbulent disks using 3D MHD simulations. Furthermore, Nelson and Papaloizou (2004) investigated planet migration in an MRI-turbulent disk and observed stochastic migration. However, the origin of the torque on the planet in a turbulent disk is not well studied.

The MRI arises under conditions in which a weak magnetic field threads the disk and the radial component of the field can be stretched and enhanced by the differential rotation in the disk. Such a seed field can either be an axial field, perpendicular to the disk (Balbus and Hawley 1991, 1998), or an azimuthal field (Terquem and Papaloizou 1996). Below, we briefly summarize the conditions for the onset of the MRI instability in these two cases.

2.5.1 Axial Seed Magnetic Field.

Balbus and Hawley (1991) considered the case in which an axial magnetic field, $B_0\hat{\mathbf{z}}$, threads a Keplerian disk that rotates with an angular speed Ω. For ax-

isymmetric perturbations of the disk, for which $\delta\mathbf{v} = [\delta v_r(z,t), \delta v_\varphi(z,t), 0]$ and $\delta\mathbf{B} = [\delta B_r(z,t), \delta B_\varphi(z,t), 0]$, and for perturbations proportional to $\exp(ik_z z - i\omega t)$, one finds the dispersion relation

$$\omega_\pm^2 = (k_z v_A)^2 + \frac{1}{2}\kappa_r^2 \pm \left[\frac{1}{4}\kappa_r^4 + 4(k_z v_A \Omega)^2\right]^{1/2}, \tag{2.13}$$

where $v_A \equiv B_0/\sqrt{4\pi\rho}$ is the Alfvén velocity, and

$$\kappa_r \equiv [4\Omega^2 + 2r\Omega d\Omega/dr]^{1/2} \tag{2.14}$$

is the radial epicyclic frequency of the disk. In order for the perturbation to fit within the vertical extent of the disk, one needs $k_z h \gtrsim 1$, where $h = c_s/\Omega$ is the half-thickness of the disk and c_s is the isothermal sound speed in the disk. For most conditions, the disk is thin, with $h \ll r$ or $c_s \ll r\Omega$. Evidently, instability can occur if $\omega_-^2 < 0$, which happens if $(k_z v_A)^2 < -r\Omega d\Omega^2/dr$. For a Keplerian disk, this corresponds to $(k_z v_A)^2 < 3\Omega^2$. Therefore, the above-mentioned condition that $k_z h \gtrsim 1$ implies that instability occurs only for $v_A < c_s$.

2.5.2 Toroidal seed magnetic field.

Terquem and Papaloizou (1996) studied the linear MHD stability/instability of a thin Keplerian disk with a toroidal magnetic field $B_\varphi(r,z)$. This case is more complicated than the case of a vertical field (Balbus and Hawley 1998).

The complication in the toroidal field case results from the presence of both the MRI instability and the buoyancy instability of the toroidal field (Hoyle and Ireland 1960; Parker 1966). The buoyancy instability is triggered by an azimuthally-dependent, radially-localized vertical displacement in the plasma and the toroidal field (Terquem and Papaloizou 1996). These authors find that

the MRI instability in a thin disk with an embedded toroidal magnetic field shows up in localized perturbations (i.e., whose wavelengths are small compared with r), $\propto \exp(ik_r r + im\varphi + ik_z z - i\omega t)$, under the conditions $k_z^2 \gg k_r^2$ and $(k_\varphi v_A)^2 < -rd\Omega^2/dr$, where $k_\varphi = m/r$. This is the same as the condition for the MRI instability in a disk threaded by a vertical field with $B_z \to B_\varphi$ and $k_z \to k_\varphi$. Therefore, perturbations of the azimuthal field may also lead to MRI turbulence.

CHAPTER 3

NUMERICAL METHOD

A number of numerical MHD codes have been developed for modeling plasma flows in astrophysics. Some of the most well-known codes are *ZEUS* (Stone and Norman 1992a,b), *FLASH* (Fryxell et al. 2000), *PLUTO* (Mignone et al. 2007), and *ATHENA* (Stone et al. 2008; Skinner and Ostriker 2010). Multiple different numerical algorithms have also been developed for the numerical integration of the MHD equations, including different approaches for the spatial and temporal approximations (Brio and Wu 1988; Cockburn et al. 1989; Dai and Woodward 1994a,b; Ryu and Jones 1995; Balsara and Spicer 1999; Gurski 2004; Ustyugov et al. 2009), as well as different algorithms for the approximate solution of the Riemann problem (Brio and Wu 1988; Li 2005; Miyoshi and Kusano 2005; Miyoshi et al. 2010).

Our group developed a code to numerically model astrophysical MHD flows. This code has been developed for use in several coordinate systems: (1) 2.5D axisymmetric cylindrical coordinates (r, z); (2) 2D polar coordinates (r, ϕ); (3) 3D cylindrical coordinates (r, ϕ, z); and (4) a Cartesian (x, y) geometry which is used to conduct tests of the ideal and non-ideal MHD modules. Each version of the code is based on the standard ideal MHD approach: the matter flow can be described with the one-fluid approximation.

The difference between our code and the above-mentioned codes lies in the specifics of the astrophysical problems that we solve. Most importantly, in the astrophysical regimes that we study, strong shocks (where the energy dissipation cannot be neglected) are not expected to occur. This permits the use of the entropy conservation equation instead of the full energy equation. The advan-

tage of this approach is that the entropy conservation equation does not contain terms that differ significantly in magnitude. For example, in the energy equation, the largest terms are the gravitational energy and the kinetic energy of the azimuthal motion; these can be much larger than the internal energy and the energy of the poloidal motion near a gravitating body. Additionally, in the vicinity of a magnetized star, the magnetic energy density can significantly exceed the matter pressure (and the energy-density of thermal energy), leading to significant errors when computing the energy conservation equation. This makes the use of the entropy equation particularly desirable.

To study planetary migration, w used the 2D polar version of the code. In this version of the code, the components of the velocity and magnetic field perpendicular to the plane of the flow are set to zero. Additionally, surface density and surface magnetic field are used instead of their volumetric counterparts. The formal structure of the MHD equations is the same but we make additional suggestions about the disk and the definitions of the (surface) magnetic field so that the conservation equations retain the same conservative form. Our codes use a Riemann solver based on methods developed by Miyoshi and Kusano (2005), modified to include the equation for the entropy balance. From this point forward, I will focus the discussion on the 2D polar version of the code, except when describing tests of the code (in which I will describe the Cartesian geometry).

3.1 Godunov methods

In order to numerically solve the ideal MHD equations, we use the Godunov method, in which the fundamental problem is to develop an exact or approxi-

mate algorithm to solve the Riemann problem. The Riemann problem is a special type of Initial Value Problem. Consider the following 1D partial differential equation describing the variable $u(x,t)$:

$$\frac{\partial u}{\partial t} + a\frac{\partial u}{\partial x} = 0. \tag{3.1}$$

The initial conditions are defined as

$$u(x,0) = u_0(x) = \begin{cases} u_{\mathrm{L}} & \text{if } \; x < 0 \\ \\ u_{\mathrm{R}} & \text{if } \; x > 0, \end{cases} \tag{3.2}$$

where u_{L} (left state) and u_{R} (right state) are constant. Fig. 3.1 shows the initial data for the Riemann problem, in which there is a discontinuity at $x = 0$. This discontinuity' propagates at some speed a, while the solution to the left of the discontinuity is given by u_{L} and the solution to the right of the discontinuity is given by u_{R}. The solution of the Riemann problem is just the solution to Eqn. 3.1, which is

$$u(x,t) = u_0(x - at) = \begin{cases} u_{\mathrm{L}} & \text{if } \; x - at < 0 \\ \\ u_{\mathrm{R}} & \text{if } \; x - at > 0, \end{cases} \tag{3.3}$$

A schematic showing the two possible solutions, separated by the wave propagating at speed a is shown in Fig. 3.2.

The construction of an exact solution to the Riemann problem can become numerically complex and is often computationally expensive. Exact solutions to the Riemann problem have been realized by Ryu and Jones (1995), and these exact solutions are used for the testing of our approximate Riemann solver. Consider a one-dimensional hyperbolic system of equations in conservative form:

$$\frac{\partial \mathcal{U}}{\partial t} + \frac{\partial \mathcal{F}(\mathcal{U})}{\partial x} = 0. \tag{3.4}$$

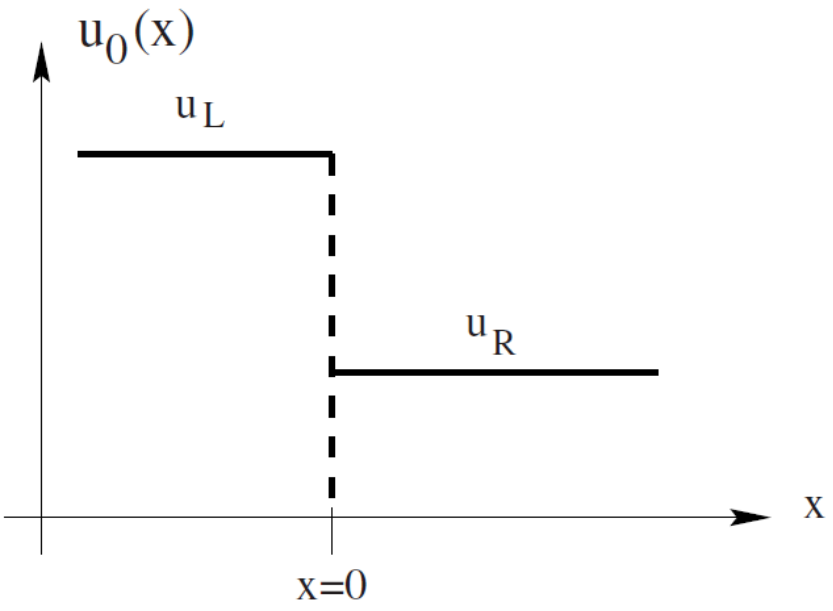

Figure 3.1 Initial data for the 1D Riemann problem described by the linear advection equation. Two states (left and right) are separated by a discontinuity at $x = 0$ (Toro 2009).

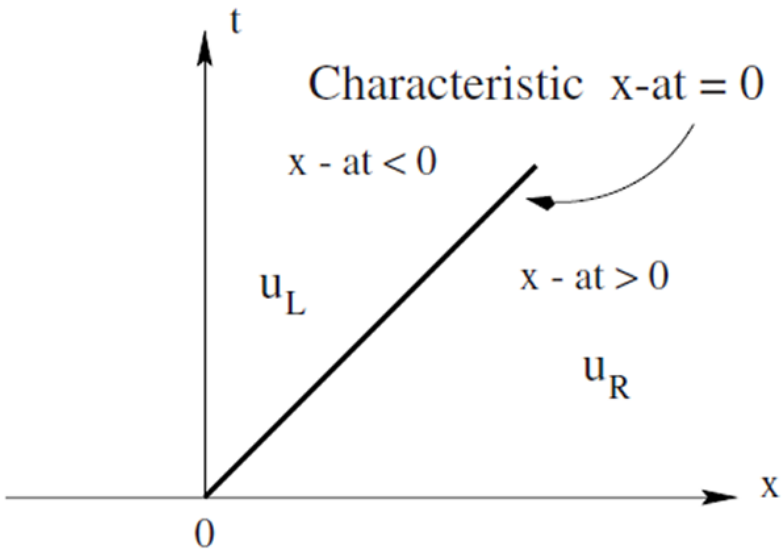

Figure 3.2 The solution to the 1D Riemann problem described by the linear advection equation with a wave speed of a (Toro 2009).

Here, $\mathcal{U} = \{U_1, \ldots, U_n\}$ is the vector of conservative variables and $\mathcal{F}(\mathcal{U}) = \{F_1, \ldots, F_n\}$ is the flux function which maps each conservative variable to its corresponding flux. Eqn. 3.4 can be rewritten in the integral form of the conservation laws

$$\int_{\Delta\xi} \mathcal{U}_{\mathrm{ex}}(\xi) d\xi = \int_{\Delta\xi} \mathcal{U}|_{t=0} d\xi + \mathcal{F}_{\mathrm{L}} - \mathcal{F}_{\mathrm{R}}, \tag{3.5}$$

where $\mathcal{U}_{\mathrm{ex}}(\xi; \mathcal{U}_{\mathrm{L}}, \mathcal{U}_{\mathrm{R}})$ represents the exact solution of the Riemann problem between the left and right states $\mathcal{U}_{\mathrm{L}}$ and $\mathcal{U}_{\mathrm{R}}$; $\xi = x/t$ is a self-similar velocity variable; $\Delta\xi$ is the interval along the variable ξ at which all of the waves are localized; and $\mathcal{F}_{\mathrm{L}} = \mathcal{F}(\mathcal{U}_{\mathrm{L}})$ and $\mathcal{F}_{\mathrm{R}} = \mathcal{F}(\mathcal{U}_{\mathrm{R}})$ are the fluxes for the left and right states, respectively.

The Riemann problem can be approximated by a number of discontinuities, each of which satisfies the Rankine-Hugoniot jump conditions[1]:

$$\dot{x}\,(\mathcal{U}_2 - \mathcal{U}_1) = \mathcal{F}_2 - \mathcal{F}_1. \tag{3.6}$$

Here, $\dot{x}$ is velocity of the discontinuity; $\mathcal{U}_1, \mathcal{U}_2$ are the conservative variables on either side of the discontinuity; and $\mathcal{F}_1, \mathcal{F}_2$ are the fluxes of the conservative variables across the discontinuity. In the general case, $\mathcal{F}_1 \neq \mathcal{F}(\mathcal{U}_1)$ and $\mathcal{F}_2 \neq \mathcal{F}(\mathcal{U}_2)$, excluding $\mathcal{F}_{\mathrm{L}} = \mathcal{F}(\mathcal{U}_{\mathrm{L}}), \mathcal{F}_{\mathrm{R}} = \mathcal{F}(\mathcal{U}_{\mathrm{R}})$. In this case, the condition for self-consistency of the conservation laws is evidently satisfied, while Eqn. 3.7 for the calculation of fluxes gives $\mathcal{F} = \mathcal{F}^*$, where $\mathcal{F}^*$ is the flux in the interval which includes the point $x = 0$. If the point $x = 0$ is located at the boundary between intervals (that is, *at* the discontinuity, where $\dot{x} = 0$), then the flux can be calculated for any two adjacent states. These fluxes are the same as the ones present in the Rankine-Hugoniot jump conditions.

[1]The Rankine-Hugoniot jump conditions describe the relationship between the states on the left and right sides of a discontinuity.

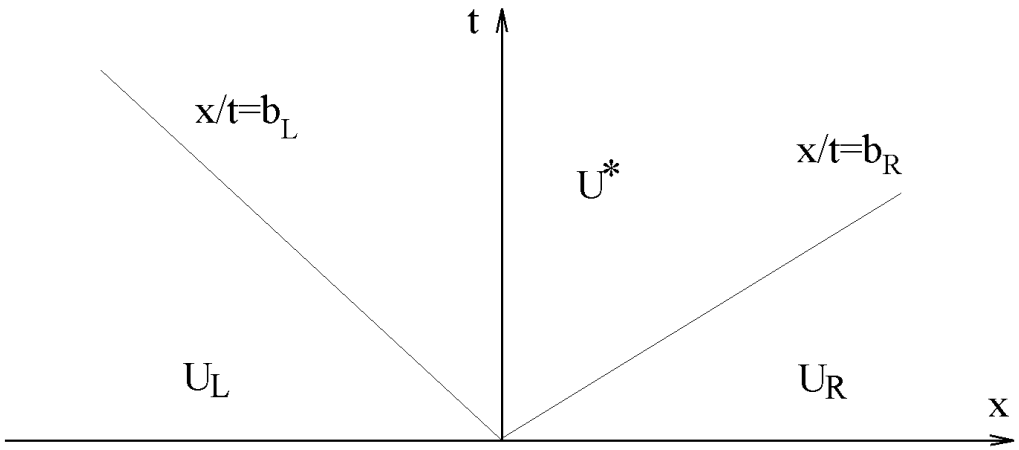

Figure 3.3 The wave propagation diagram for the HLL method in the (x, t)-plane.

The approximate solution of the Riemann problem is represented by the vector $\mathcal{U}(\xi)$ which approximates the same conservation laws in integral form. The flux between the left and right states is approximated by

$$\begin{aligned} FLUX(\mathcal{U}_{\mathrm{L}}, \mathcal{U}_{\mathrm{R}}) &= \mathcal{F}_{\mathrm{L}} + \int_0^{\infty} (\mathcal{U}(\xi) - \mathcal{U}_{\mathrm{L}})\, d\xi \\ &= \mathcal{F}_{\mathrm{R}} - \int_0^{\infty} (\mathcal{U}(\xi) - \mathcal{U}_{\mathrm{R}})\, d\xi. \end{aligned} \tag{3.7}$$

One of the simplest approximate Riemann solvers was proposed by Harten et al. (1983) is known as the HLL solver (named for its authors); it has two discontinuities separating three homogeneous states (as shown in Fig. 3.3). One discontinuity propagates to the left with velocity b_{L}, while the other propagates to the right with velocity b_{R}. The approximate solution is assumed to be homogeneous between these discontinuities: $\mathcal{U}(\xi) = \mathcal{U}^*$. More advanced approximate Riemann solvers include two or more intermediate states (Gurski 2004; Li 2005; Miyoshi and Kusano 2005).

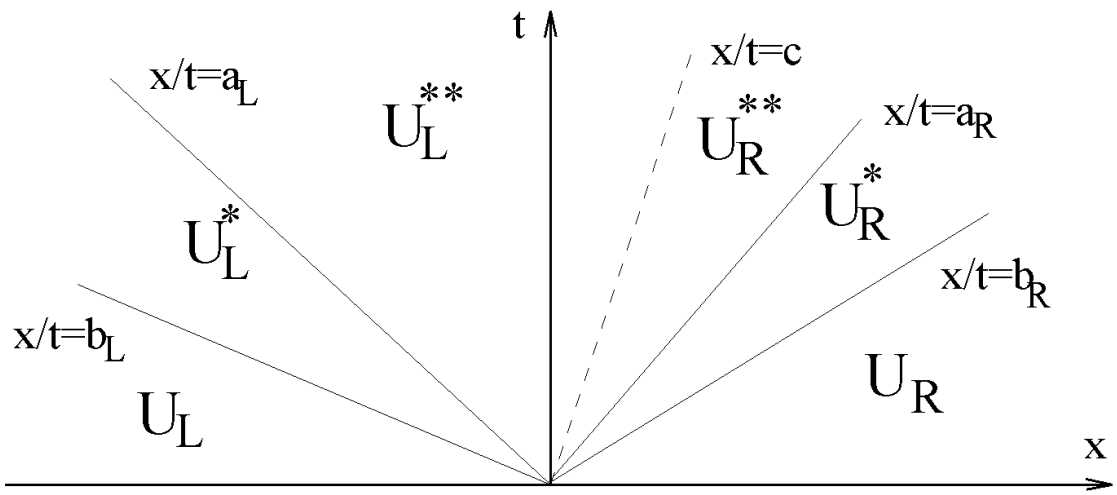

Figure 3.4 The wave propagation diagram for the HLLD method in the (x, t)-plane.

3.1.1 The Miyoshi & Kusano HLLD Solver

Here, we describe the construction of the Godunov method that we use to solve the ideal MHD equations. As noted earlier, we use the entropy conservation equation instead of the energy equation. The conservative variables and fluxes in Eqn. 3.4 take on the form:

$$\mathcal{U} = \begin{pmatrix} \rho \\ \rho s \\ \rho v_x \\ \rho v_y \\ \rho v_z \\ B_y \\ B_z \end{pmatrix} \qquad \mathcal{F} = \begin{pmatrix} \rho v_x \\ \rho s v_x \\ \rho v_x^2 + p + \frac{B_y^2 + B_z^2}{4\pi} \\ \rho v_y v_x - \frac{B_{x0} B_y}{4\pi} \\ \rho v_z v_x - \frac{B_{x0} B_z}{4\pi} \\ v_x B_y - v_y B_{x0} \\ v_x B_z - v_z B_{x0} \end{pmatrix}. \tag{3.8}$$

A newer version of the HLL method that includes the propagation of the central wave is known as the HLLC method. Li (2005) proposed a modification

of the HLLC approximate Riemann solver for the equations of MHD in which the transverse y, z-components of the velocity and magnetic field are assumed to be the same in both intermediate states. For this reason, in the limit $B_{x0} \to 0$, the HLLC solver does not convert to the HLLC algorithm with a purely transverse magnetic field; this is because arbitrary jumps of the y, z-components of velocity and magnetic field are still allowed at the contact discontinuity (as they are converted to the tangential component).

The choice of entropy conservation inhibits the modeling of MHD flows with strong shocks at which entropy production occurs. Our approximate solution uses the HLLD solver introduced by (Miyoshi and Kusano 2005). It has has four intermediate states, and the wave propagation in the HLLD algorithm is shown in Fig. 3.4. The initial discontinuity between the states $\mathcal{U}_{\rm L}$ and $\mathcal{U}_{\rm R}$ decays and the discontinuities appear, propagating away with velocities $b_{\rm L}, b_{\rm R}$ (fast magnetosonic waves), $a_{\rm L}, a_{\rm R}$ (Alfvén waves) and c (the contact discontinuity). These jumps separate the initial ($\mathcal{U}_{\rm L}, \mathcal{U}_{\rm R}$) and intermediate ($\mathcal{U}^{*}_{\rm L}, \mathcal{U}^{**}_{\rm L}, \mathcal{U}^{*}_{\rm R}, \mathcal{U}^{**}_{\rm R}$) states (see Fig. 3.4).

Calculation of the intermediate states

The calculation of the conservative variables and fluxes in the intermediate states is performed using the following scheme. The normal velocities across the Alfvén and contact discontinuities are assumed to be continuous

$$v^{*}_{x\rm L} = v^{**}_{x\rm L} = v^{*}_{x\rm R} = v^{**}_{x\rm R} = c, \tag{3.9}$$

which implies

$$\rho_{\rm L}^{*} = \rho_{\rm L}^{**} \qquad \text{and} \qquad \rho_{\rm R}^{*} = \rho_{\rm R}^{**}; \tag{3.10}$$

$$s_{\rm L}^{*} = s_{\rm L}^{**} \qquad \text{and} \qquad s_{\rm R}^{*} = s_{\rm R}^{**} \tag{3.11}$$

from the Rankine-Hugoniot jump conditions.

We write the Rankine-Hugoniot conditions for fast magnetosonic waves for all of the equations except the conservation equation for the $x-$component of the momentum. For the densities in states $\mathcal{U}_{\rm L}^{*}$ and $\mathcal{U}_{\rm R}^{*}$, we obtain the relations

$$\rho_{\rm L}^{*} = \rho_{\rm L}\frac{b_{\rm L} - v_{x\rm L}}{b_{\rm L} - v_{x\rm L}^{*}} = \rho_{\rm L}\frac{b_{\rm L} - v_{x\rm L}}{b_{\rm L} - c} \tag{3.12}$$

and

$$\rho_{\rm R}^{*} = \rho_{\rm R}\frac{b_{\rm R} - v_{x\rm R}}{b_{\rm R} - v_{x\rm R}^{*}} = \rho_{\rm R}\frac{b_{\rm R} - v_{x\rm R}}{b_{\rm R} - c}. \tag{3.13}$$

From Eqn. 3.12, Eqn. 3.13, and the x-component of the momentum equation we obtain

$$c = \frac{\chi}{\rho_{\rm L}(v_{x\rm L} - b_{\rm L}) + \rho_{\rm R}(b_{\rm R} - v_{x\rm R})}, \tag{3.14}$$

where

$$\chi \equiv \left[\left(\rho v_x^2 + p + \frac{B^2}{8\pi} - \frac{B_{x0}^2}{4\pi}\right)_{\rm L} - b_{\rm L}(\rho v_x)_{\rm L}\right] - \left[\left(\rho v_x^2 + p + \frac{B^2}{8\pi} - \frac{B_{x0}^2}{4\pi}\right)_{\rm R} - b_{\rm R}(\rho v_x)_{\rm R}\right]. \tag{3.15}$$

Combining Eqn. 3.12, Eqn. 3.13, and the Rankine-Hugoniot jump conditions for the entropy, we find

$$s_{\rm L}^{*} = s_{\rm L}^{**} = s_{\rm L} \qquad \text{and} \qquad s_{\rm R}^{*} = s_{\rm R}^{**} = s_{\rm R}. \tag{3.16}$$

To calculate the transverse components of the velocity and magnetic field in the intermediate states, we use the corresponding components of the momentum and induction equations. In the intermediate states, $\mathcal{U}_{\rm L}^{*}$ and $\mathcal{U}_{\rm R}^{*}$, these

values are determined from the jump conditions across the fast magnetosonic waves:

$$v_{y\mathrm{L}}^{*} = v_{y\mathrm{L}} + \frac{B_{x0}B_{y\mathrm{L}}}{4\pi}\frac{v_{x\mathrm{L}} - c}{\rho_{\mathrm{L}}^{*}(b_{\mathrm{L}} - c)^2 - \dfrac{B_{x0}^2}{4\pi}} \tag{3.17}$$

and

$$B_{y\mathrm{L}}^{*} = B_{y\mathrm{L}}\frac{\rho_{\mathrm{L}}(b_{\mathrm{L}} - v_{x\mathrm{L}})^2 - \dfrac{B_{x0}^2}{4\pi}}{\rho_{\mathrm{L}}^{*}(b_{\mathrm{L}} - c)^2 - \dfrac{B_{x0}^2}{4\pi}}. \tag{3.18}$$

Analogously, for the z component we have

$$v_{z\mathrm{L}}^{*} = v_{z\mathrm{L}} + \frac{B_{x0}B_{z\mathrm{L}}}{4\pi}\frac{v_{x\mathrm{L}} - c}{\rho_{\mathrm{L}}^{*}(b_{\mathrm{L}} - c)^2 - \dfrac{B_{x0}^2}{4\pi}} \tag{3.19}$$

and

$$B_{z\mathrm{L}}^{*} = B_{z\mathrm{L}}\frac{\rho_{\mathrm{L}}(b_{\mathrm{L}} - v_{x\mathrm{L}})^2 - \dfrac{B_{x0}^2}{4\pi}}{\rho_{\mathrm{L}}^{*}(b_{\mathrm{L}} - c)^2 - \dfrac{B_{x0}^2}{4\pi}}. \tag{3.20}$$

The values of $v_{y\mathrm{R}}^{*}, v_{z\mathrm{R}}^{*}, B_{y\mathrm{R}}^{*}, B_{z\mathrm{R}}^{*}$ are calculated using the same formulae, substituting the index $\mathrm{L} \to \mathrm{R}$.

The Rankine-Hugoniot jump conditions at the Alfvén waves (with $\rho_{\mathrm{L}}^{**} = \rho_{\mathrm{L}}^{*}$, $\rho_{\mathrm{R}}^{**} = \rho_{\mathrm{R}}^{*}$) can be solved, but only if

$$a_{\mathrm{L}} = c \pm \frac{B_{x0}}{\sqrt{4\pi\rho_{\mathrm{L}}^{*}}} \tag{3.21}$$

and

$$a_{\mathrm{R}} = c \pm \frac{B_{x0}}{\sqrt{4\pi\rho_{\mathrm{R}}^{*}}}. \tag{3.22}$$

In the first case, we adopt $a_{\mathrm{L}} = c - |B_{x0}|\Big/\sqrt{4\pi\rho_{\mathrm{L}}^{*}}$, which corresponds to an Alfvén wave propagating to the left along the state $\mathcal{U}_{\mathrm{L}}^{*}$. In the second case, we take $a_{\mathrm{R}} = c + |B_{x0}|\Big/\sqrt{4\pi\rho_{\mathrm{R}}^{*}}$, which corresponds to an Alfvén wave propagating to the right along the state $\mathcal{U}_{\mathrm{R}}^{*}$.

To compute the transverse components of the velocity and magnetic field in the intermediate states ($\mathcal{U}^{**}_{\rm L}$, $\mathcal{U}^{**}_{\rm R}$), we use the fact that, at the contact discontinuity,

$$v^{**}_{y\rm L} = v^{**}_{y\rm R} = v^{**}_{y}, \tag{3.23}$$

$$v^{**}_{z\rm L} = v^{**}_{z\rm R\mathit{R}} = v^{**}_{z}, \tag{3.24}$$

$$B^{**}_{y\rm L} = B^{**}_{y\rm R} = B^{**}_{y}, \tag{3.25}$$

and

$$B^{**}_{z\rm L} = B^{**}_{z\rm R} = B^{**}_{z}, \tag{3.26}$$

for $B_{x0} \neq 0$.

Plugging these into the integral conservation laws, we find that the transverse components of the velocity and magnetic field are

$$v^{**}_{y} = \frac{v^{*}_{y\rm L}\sqrt{\rho^{*}_{\rm L}} + v^{*}_{y\rm R}\sqrt{\rho^{*}_{\rm R}} + \dfrac{\sigma(B^{*}_{y\rm R} - B^{*}_{y\rm L})}{\sqrt{4\pi}}}{\sqrt{\rho^{*}_{\rm L}} + \sqrt{\rho^{*}_{\rm R}}}, \tag{3.27}$$

$$v^{**}_{z} = \frac{v^{*}_{z\rm L}\sqrt{\rho^{*}_{\rm L}} + v^{*}_{z\rm R}\sqrt{\rho^{*}_{\rm R}} + \dfrac{\sigma(B^{*}_{z\rm R} - B^{*}_{z\rm L})}{\sqrt{4\pi}}}{\sqrt{\rho^{*}_{\rm L}} + \sqrt{\rho^{*}_{\rm R}}}, \tag{3.28}$$

$$B^{**}_{y} = \frac{B^{*}_{y\rm L}\sqrt{\rho^{*}_{\rm R}} + B^{*}_{y\rm R}\sqrt{\rho^{*}_{\rm L}} + \sigma(v^{*}_{y\rm R} - v^{*}_{y\rm L})\sqrt{4\pi\rho^{*}_{\rm L}\rho^{*}_{\rm R}}}{\sqrt{\rho^{*}_{\rm L}} + \sqrt{\rho^{*}_{\rm R}}}, \tag{3.29}$$

and

$$B^{**}_{z} = \frac{B^{*}_{z\rm L}\sqrt{\rho^{*}_{\rm R}} + B^{*}_{z\rm R}\sqrt{\rho^{*}_{\rm L}} + \sigma(v^{*}_{z\rm R} - v^{*}_{z\rm L})\sqrt{4\pi\rho^{*}_{\rm L}\rho^{*}_{\rm R}}}{\sqrt{\rho^{*}_{\rm L}} + \sqrt{\rho^{*}_{\rm R}}}, \tag{3.30}$$

where $\sigma = \mathrm{sign}(B_{x0})$ (Miyoshi and Kusano 2005).

Note that the transverse components of the magnetic field B_t are not necessarily equal ($|B^{*}_{t\rm L}| \neq |B^{**}_{t}| \neq |B^{*}_{t\rm R}|$) due to the jump conditions for the Alfvén

waves in the complete system of MHD equations. Here, we remove the condition $\mathcal{F}^* = \mathcal{F}(\mathcal{U}^*)$ (in this case, for the $x-$component of the momentum equation) and hence lose the continuity of the magnetic pressure for the Alfvén waves.

The fluxes in the intermediate states are calculated from the jump conditions:

$$\mathcal{F}_{\mathrm{L}}^{*} = \mathcal{F}_{\mathrm{L}} + b_{\mathrm{L}}(\mathcal{U}_{\mathrm{L}}^{*} - \mathcal{U}_{\mathrm{L}}), \tag{3.31}$$

$$\mathcal{F}_{\mathrm{L}}^{**} = \mathcal{F}_{\mathrm{L}}^{*} + a_{\mathrm{L}}(\mathcal{U}_{\mathrm{L}}^{**} - \mathcal{U}_{\mathrm{L}}^{*}) = \mathcal{F}_{\mathrm{L}} + a_{\mathrm{L}}(\mathcal{U}_{\mathrm{L}}^{**} - \mathcal{U}_{\mathrm{L}}^{*}) + b_{\mathrm{L}}(\mathcal{U}_{\mathrm{L}}^{*} - \mathcal{U}_{\mathrm{L}}), \tag{3.32}$$

$$\mathcal{F}_{\mathrm{R}}^{*} = \mathcal{F}_{\mathrm{R}} + b_{\mathrm{R}}(\mathcal{U}_{\mathrm{R}}^{*} - \mathcal{U}_{\mathrm{R}}), \tag{3.33}$$

$$\mathcal{F}_{\mathrm{R}}^{**} = \mathcal{F}_{\mathrm{R}}^{*} + a_{\mathrm{R}}(\mathcal{U}_{\mathrm{R}}^{**} - \mathcal{U}_{\mathrm{R}}^{*}) = \mathcal{F}_{\mathrm{R}} + a_{\mathrm{R}}(\mathcal{U}_{\mathrm{R}}^{**} - \mathcal{U}_{\mathrm{R}}^{*}) + b_{\mathrm{R}}(\mathcal{U}_{\mathrm{R}}^{*} - \mathcal{U}_{\mathrm{R}}). \tag{3.34}$$

One does not need to calculate all of the fluxes. Rather, we determine which of the states appears at the point $x = 0$ (i.e., which interval $(-\infty, b_{\mathrm{L}}), ..., (b_{\mathrm{R}}, \infty)$ contains the point $x = 0$) and then calculate the corresponding flux using one of the formulae 3.31-3.34.

In the limit $B_{x0} \to 0$, the relationships in Eqn. 3.17 and Eqn. 3.18 give the results

$$v_{y\mathrm{L}}^{*} = v_{y\mathrm{L}} \tag{3.35}$$

and

$$B_{y\mathrm{L}}^{*} = B_{y\mathrm{L}} \frac{\rho_{\mathrm{L}}(b_{\mathrm{L}} - v_{x\mathrm{L}})^2}{\rho_{\mathrm{L}}^{*}(b_{\mathrm{L}} - c)^2} = B_{y\mathrm{L}} \frac{\rho_{\mathrm{L}}^{*}}{\rho_{\mathrm{L}}}. \tag{3.36}$$

Similar relationships can be derived for the z-component of velocity and magnetic field and for the fast magnetosonic wave which propagates to the right along $\mathcal{U}_{\mathrm{R}}$. Additionally since $a_{\mathrm{L}} = a_{\mathrm{R}} = c$ when $B_{x0} = 0$, the intermediate states $\mathcal{U}_{\mathrm{L}}^{**}, \mathcal{U}_{\mathrm{R}}^{**}$ disappear.

In the above derivations it is assumed that the following inequalities are satisfied:

$$b_{\mathrm{L}} \leq a_{\mathrm{L}} \leq c \leq a_{\mathrm{R}} \leq b_{\mathrm{R}}. \tag{3.37}$$

The case $a_{\rm L} = c = a_{\rm R}$, corresponding to $B_{x0} = 0$, has been considered above. The cases where $b_{\rm L} = a_{\rm L}$ or $a_{\rm R} = b_{\rm R}$ correspond to the switch-on waves propagating to the left or to the right, assuming $B_{t,{\rm L}} = 0$ or $B_{t,{\rm R}} = 0$ at $B_{x0} \neq 0$, and are not considered. The wave velocities $b_{\rm L}$ and $b_{\rm R}$ are estimated as

$$b_{\rm L} \leq (v_x - c_{\rm F})_{\rm L} \tag{3.38}$$

and

$$b_{\rm R} \geq (v_x + c_{\rm F})_{\rm R}, \tag{3.39}$$

where $c_{\rm F,L}, c_{\rm F,R}$ are the velocities of the fast magnetosonic waves that are propagating along the states $\mathcal{U}_{\rm L}, \mathcal{U}_{\rm R}$ respectively.

3.1.2 Correction of wave velocities

Eqns. 3.17, 3.18, 3.31, and 3.32 show the values of the tangential velocities and magnetic fields in the intermediate states $\mathcal{U}^*_{\rm L}, \mathcal{U}^*_{\rm R}$. The numerators on the right-hand sides of these formulae are non-negative, while the denominators have the form

$$\Delta = \rho^*_{\rm R}(b_{\rm R} - c)^2 - \frac{B^2_{x0}}{4\pi} = \rho_{\rm R}(b_{\rm R} - v_{x{\rm R}})(b_{\rm R} - c) - \frac{B^2_{x0}}{4\pi}. \tag{3.40}$$

The formula for the left state is analogous.

The physical sense of the last value is such that it should be positive because the Alfvén wave should always propagate slower than the fast MHD discontinuity. The case when this denominator is zero corresponds to the switch-on wave, in which a finite tangential field beyond the discontinuity appears from the zero tangential field in front of the discontinuity. In the approximate Riemann solver it is reasonable to retain this property (the positive sign of the denominator) in order to avoid a non-physical change of the sign of the tangential

field and the appearance of a singularity as $\Delta \to 0$. For that, we require that the inequality $b_{\rm R} \geq c + k|B_{x0}|\Big/\sqrt{4\pi\rho^*_{\rm R}}$ is satisfied, at some $k > 1$. In that case, we have

$$b_{\rm R} - c - \frac{k|B_{x0}|}{\sqrt{4\pi\rho^*_{\rm R}}} = b_{\rm R} - c - \frac{k|B_{x0}|\sqrt{b_{\rm R} - c}}{\sqrt{4\pi\rho_{\rm R}(b_{\rm R} - v_{x\rm R})}} \geq 0. \tag{3.41}$$

This can be rewritten as

$$\rho_{\rm R}(b_{\rm R} - c)(b_{\rm R} - v_{x\rm R}) \geq \frac{k^2 B^2_{x0}}{4\pi}. \tag{3.42}$$

Comparing this relationship with that for Δ, we conclude that if the condition in Eqn. 3.42 is satisfied then $\Delta > 0$. Analogously:

$$\rho_{\rm L}(b_{\rm L} - c)(b_{\rm L} - v_{x\rm L}) \geq \frac{k^2 B^2_{x0}}{4\pi}. \tag{3.43}$$

If the conditions in Eqn. 3.42 and/or Eqn. 3.43 are not satisfied (after computing c using Eqn. 3.14) then we perform a correction of $b_{\rm R}$ and/or $b_{\rm L}$, choosing the fast magnetosonic velocity to be the largest and/or the smallest of the roots of Eqn. 3.42 and/or Eqn. 3.43. Here, $b_{\rm R}$ can only increase while $b_{\rm L}$ can only decrease. We then recalculate the value of c, check the conditions in Eqn. 3.42 and Eqn. 3.43, and (if necessary) again apply corrections to $b_{\rm L}$ and $b_{\rm R}$. [2]

3.1.3 Time Integration

To increase the accuracy of the numerical algorithm, we perform a two-stage Runge-Kutta integration of the equations in time. In the first stage, we calculate the values for the intermediate timestep, $\mathcal{U}_i^{n+1/2}$, where the timestep is indicated

[2] Because we use the equation for entropy conservation instead of the equation of energy conservation, the correction of the velocities of the fast MHD discontinuities and the positivity of the approximate solution of the Riemann solver (in the sense that the density and entropy are positive in all intermediate states) is established trivially.

by the superscript:

$$\mathcal{U}_i^{n+1/2} = \mathcal{U}_i^n - \frac{\Delta t}{2\Delta x}\left(\mathcal{F}_{i+1/2}^n - \mathcal{F}_{i-1/2}^n\right). \tag{3.44}$$

Here, the fluxes $\mathcal{F}_{i+1/2}^n$ are calculated using the entropy-based HLLD algorithm described above. Formally, we can write the flux calculation procedure in the form $\mathcal{F}_{i+1/2}^n = FLUX\left(\mathcal{U}_i^n, \mathcal{U}_{i+1}^n\right)$ where we take the left and right states in the HLLD solver to be $\mathcal{U}_\mathrm{L} = \mathcal{U}_i$ and $\mathcal{U}_\mathrm{R} = \mathcal{U}_{i+1}$.

In the second stage, the values for the full timestep, $t^{n+1} = t^n + \Delta t$, are calculated as

$$\mathcal{U}_i^{n+1} = \mathcal{U}_i^n - \frac{\Delta t}{\Delta x}\left(\mathcal{F}_{i+1/2}^{n+1/2} - \mathcal{F}_{i-1/2}^{n+1/2}\right). \tag{3.45}$$

The timestep Δt is set by the Courant-Friedrichs-Levy (CFL) condition, which places an upper limit on the timestep by considering the wave crossing speeds in all cells on the grid. This timestep is typically limited by the smallest cells near the axis. For the calculation of the fluxes $\mathcal{F}_{i+1/2}^{n+1/2}$ we use values from the intermediate timestep $\mathcal{U}_i^{n+1/2}$, reconstructed on the edges of the calculated cells:

$$\mathcal{F}_{i+1/2}^{n+1/2} = FLUX\left(\mathcal{U}_{\mathrm{R},i}^{n+1/2}, \mathcal{U}_{\mathrm{L},i+1}^{n+1/2}\right). \tag{3.46}$$

The values $\mathcal{U}_\mathrm{L}$, $\mathcal{U}_\mathrm{R}$ are calculated at each grid cell boundary using one of the previously described approximate Riemann solvers. In order to increase the accuracy of our scheme, a slope limiter correction is applied to the primitive variables at the edges of each cell:

$$u_{\mathrm{L},i} = u_i - \frac{1}{2}\mathrm{minmod}(d_{i-1/2}, d_{i+1/2}) \tag{3.47}$$

and

$$u_{\mathrm{R},i} = u_i + \frac{1}{2}\mathrm{minmod}(d_{i-1/2}, d_{i+1/2}). \tag{3.48}$$

For the sake of brevity, we have define $d_{i-1/2} \equiv u_i - u_{i-1}$ and $d_{i+1/2} \equiv u_{i+1} - u_i$. Thus, the left and right solutions for each primitive variable are given by:

$$u_{\mathrm{L},i} = u_i - \begin{cases} 0 & \text{if} \quad d_{i+1/2} d_{i-1/2} \leq 0 \\ \dfrac{\epsilon+2}{6\epsilon} d_{i+1/2} & \text{if} \quad |d_{i+1/2}| < \epsilon |d_{i-1/2}| \\ \dfrac{d_{i-1/2}}{3} + \dfrac{d_{i+1/2}}{6} & \text{if} \quad \epsilon |d_{i-1/2}| \leq |d_{i+1/2}| \leq 4 |d_{i-1/2}| \\ d_{i-1/2} & \text{if} \quad |d_{i+1/2}| \geq 4 |d_{i-1/2}| \end{cases} \tag{3.49}$$

and

$$u_{\mathrm{R},i} = u_i + \begin{cases} 0 & \text{if} \quad d_{i+1/2} d_{i-1/2} \leq 0 \\ \dfrac{\epsilon+2}{6\epsilon} d_{i-1/2} & \text{if} \quad |d_{i-1/2}| < \epsilon |d_{i+1/2}| \\ \dfrac{d_{i+1/2}}{3} + \frac{d_{i-1/2}}{6} & \text{if} \quad \epsilon |d_{i+1/2}| \leq |d_{i-1/2}| \leq 4 |d_{i+1/2}| \\ d_{i+1/2} & \text{if} \quad |d_{i-1/2}| \geq 4 |d_{i+1/2}|. \end{cases} \tag{3.50}$$

Here, the top indicies are dropped and we take $\epsilon = 0.5$. In our algorithm, we reconstruct the primitive variables $p, s, v_x, v_y, v_z, B_x, B_y, B_z$.

3.2 Tests of the Code

We have performed multiple tests of the code across different grid geometries. Below we show two examples of such tests. In the first, we test the ideal MHD module (i.e., without viscosity and diffusivity). In the second, we test the diffusion module separately.

3.2.1 Cartesian geometry

In a 2D Cartesian (x, y) geometry, the MHD equations take the form

$$\frac{\partial \mathcal{U}}{\partial t} + \frac{\partial \mathcal{F}}{\partial x} + \frac{\partial \mathcal{G}}{\partial y} = 0. \tag{3.51}$$

Unlike the 1D case, the vector of the conservative variables $\mathcal{U}$ has a total of seven components. The sixth and seventh components are B_x and B_y, which must satisfy the divergence free condition

$$\frac{\partial B_x}{\partial x} + \frac{\partial B_y}{\partial y} = 0. \tag{3.52}$$

The numerical algorithm for 2D is analogous to the 1D case. The time integration is performed using the two-step Runge-Kutta method described above:

$$\mathcal{U}^{n+1/2}_{i,j} = \mathcal{U}^{n}_{i,j} - \frac{\Delta t}{2\Delta x}\left(\mathcal{F}^{n}_{i+1/2,j} - \mathcal{F}^{n}_{i-1/2,j}\right) - \frac{\Delta t}{2\Delta y}\left(\mathcal{G}^{n}_{i,j+1/2} - \mathcal{G}^{n}_{i,j-1/2}\right) \tag{3.53}$$

and

$$\mathcal{U}^{n+1}_{i,j} = \mathcal{U}^{n}_{i,j} - \frac{\Delta t}{\Delta x}\left(\mathcal{F}^{n+1/2}_{i+1/2,j} - \mathcal{F}^{n+1/2}_{i-1/2,j}\right) - \frac{\Delta t}{\Delta y}\left(\mathcal{G}^{n+1/2}_{i,j+1/2} - \mathcal{G}^{n+1/2}_{i,j-1/2}\right). \tag{3.54}$$

At the same time, $\mathcal{F}^{n}_{i+1/2,j} = FLUX\left(\mathcal{U}^{n}_{i,j}, \mathcal{U}^{n}_{i+1,j}\right)$, $\mathcal{G}^{n}_{i,j+1/2} = FLUX\left(\mathcal{U}^{n}_{i,j}, \mathcal{U}^{n}_{i,j+1}\right)$. An analogous algorithm for the flux calculation is also used during the second stage of the time integration.

To ensure that the magnetic field is divergence-free in 2D, we use the method proposed by Balsara and Spicer (1999). In application to problems in Cartesian coordinates, this approach is the following: if Eqn. 3.52 is satisfied, then one can represent the x and $y-$components of the magnetic field in the form

$$B_x = \frac{\partial A_z}{\partial y} \quad \text{and} \quad B_y = -\frac{\partial A_z}{\partial x}. \tag{3.55}$$

At the same time, $\partial A_z/\partial t = -E_z$. When the equations are discretized, the conservative variables $\mathcal{U}$ are determined in the cells while the x and y fluxes, $\mathcal{F}$

and $\mathcal{G}$, are computed on the sides of the cells. The corresponding components (indicated by numerical subscript) of the flux function vectors, $\mathcal{F}$ and $\mathcal{G}$, are

$$\begin{aligned} F_6 &= 0, \\ F_7 &= -E_z, \\ G_6 &= E_z, \\ G_7 &= 0, \end{aligned} \tag{3.56}$$

where $E_z = -\left(v_x B_y - v_y B_x\right)$ is the z component of the electric field (multiplied by the speed of light). Thus, the z component of the electric field is calculated twice using two different methods: first as $-F_{7,i+1/2,j}$ and the second as $G_{6,i,j+1/2}$. If A_z is determined on the nodes of the grid $(i + 1/2, j + 1/2)$, the components of the magnetic field can be calculated on the sides of the cells as

$$\bar{B}_{x,i+1/2,j} = \frac{A_{z,i+1,j} - A_{z,i,j}}{\Delta y} \tag{3.57}$$

and

$$\bar{B}_{y,i,j+1/2} = -\frac{A_{z,i,j+1} - A_{z,i,j}}{\Delta x}. \tag{3.58}$$

At the same time, the divergence-free condition will be satisfied if we require

$$\frac{\bar{B}_{x,i+1/2,j} - \bar{B}_{x,i-1/2,j}}{\Delta x} + \frac{\bar{B}_{y,i,j+1/2} - \bar{B}_{y,i,j-1/2}}{\Delta y} = 0. \tag{3.59}$$

The magnetic field in the cells are then computed from the calculated values on the cell boundaries:

$$B_{x,i,j} = \frac{1}{2}\left(\bar{B}_{x,i-1/2,j} + \bar{B}_{x,i+1/2,j}\right) \tag{3.60}$$

and

$$B_{y,i,j} = \frac{1}{2}\left(\bar{B}_{y,i,j-1/2} + \bar{B}_{y,i,j+1/2}\right). \tag{3.61}$$

To calculate $A_{z,i+1/2,j+1/2}$ at the $(n + 1)$-th timestep, we determine the $z-$component of the electric field at each node. The simple variant proposed

by Balsara and Spicer (1999) consists of averaging the values $-F_7$ and G_6 over the cell sides surrounding the node at $(i+1/2, j+1/2)$. For a homogeneous grid, this is

$$\begin{aligned} E^{\mathrm{BS}}_{z,i+1/2,j+1/2} &= \frac{1}{4}(E_{z,i,j+1/2} + E_{z,i+1,j+1/2} + E_{z,i+1/2,j} + E_{z,i+1/2,j+1}) \\ &= \frac{1}{4}(G_{6,i,j+1/2} + G_{6,i+1,j+1/2} - F_{7,i+1/2,j} - F_{7,i+1/2,j+1}). \end{aligned} \tag{3.62}$$

In Gardiner and Stone (2005), however, it was noted that this approach is inconsistent with the numerical integration algorithm in the case of 1D problems (where the solution does not depend either on x or on y), and that the proposed procedure does not guarantee consistency. Gardiner and Stone (2005) propose a modified form (for homogenous grids)

$$E^{\mathrm{GS}}_{z,i+1/2,j+1/2} = 2E^{BS}_{z,i+1/2,j+1/2} - \frac{1}{4}\left(E_{z,i,j} + E_{z,i+1,j} + E_{z,i+1,j+1} + E_{z,i,j+1}\right). \tag{3.63}$$

To calculate E_z, we use either Eqn. 3.62 or Eqn. 3.63.

Thus, at each stage of numerical integration of the MHD equations, the magnetic field in the (x, y) plane is calculated along the following algorithm:

1. Use an approximate Riemann solver to find the $z-$components of the electric field at the sides of cells $-F_{7,i+1/2,j}$, $G_{6,i,j+1/2}$.
2. Use Eqn. 3.62 or Eqn. 3.63 to calculate the electric field in the nodes of the grid $E_{z,i+1/2,j+1/2}$.
3. Calculate the $z-$component of the magnetic field potential in grid nodes, $A_{z,i+1/2,j+1/2}$.
4. Calculate $\bar{B}_{x,i+1/2,j}$ and $\bar{B}_{y,i,j+1/2}$.
5. Using Eqn. 3.60 and Eqn. 3.61, calculate $B_{x,i,j}$ and $B_{y,i,j}$.

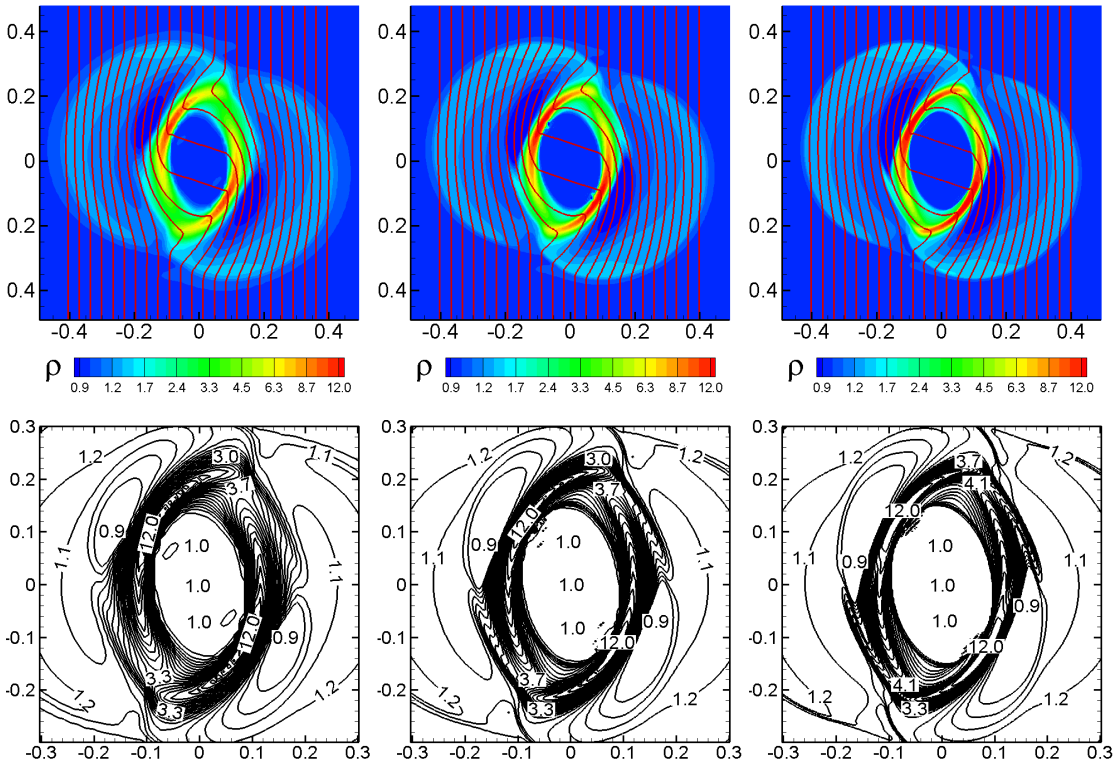

Figure 3.5 The test of the ideal MHD module of the code with the "rotor problem" at different grid resolutions. *Top Panels:* Density distribution (color background) and field lines (solid lines) with grid resolution 100×100 (left panel), 200×200 (middle panel) and 400×400 (right panel). *Bottom Panels:* The density contour lines.

3.2.2 Tests of the ideal MHD module

The 2D rotor problem

The first test is the standard "rotor problem" in Cartesian coordinates. This test has been used by a number of authors for testing MHD solvers that use the energy equation (Balsara and Spicer 1999; Tóth 2000). We use this test to check the ideal MHD module of our code (with viscosity and diffusivity switched off).

The ideal MHD equations are solved on a regular Cartesian grid in the region $-0.5 < x < 0.5$, $-0.5 < y < 0.5$ with grid sizes $\Delta x = \Delta y = 1/N$, where $N = 100, 200, 400$ for the three different tests. At the beginning of the simulations, $t = 0$, the pressure in the region is constant, $p = 1$, and the magnetic field is homogeneous, $B_x = 0$, $B_y = 5$. In the center, there is a circle of higher-density matter ($\rho_0 = 10$) with radius $r_0 = 0.1$ (where the radius is $r = \sqrt{x^2 + y^2}$). The matter in the inner circle initially rotates as a solid body with angular velocity $\omega_0 = 20$. For $r > r_1 = 0.115$, the density is $\rho_1 = 1$ and the matter is at rest. In the ring in between these two regions $r_0 < r < r_1$, the density and velocity are linearly interpolated between the values at $r = r_0$ and $r = r_1$.

The equations of ideal adiabatic MHD are solved with the previously described Godunov-type scheme. The timesteps are calculated from the condition $\Delta t = 0.4\Delta t_{CFL}$ where Δt_{CFL} is the maximum timestep allowed by the CFL condition defined previously. The results of the simulations at $t = 0.15$ are shown in Fig. 3.5. The density and the field line distributions are very similar in all three of our cases. Fig. 3.6 shows slices along the x-axis for the density, pressure, kinetic energy, and magnetic energy for each of the three grid sizes. The simulations at the highest grid resolutions give almost identical results and the convergence of the results is evident. The bottom panels of Fig. 3.5 show selected streamlines with numbers which confirm the similarity and convergence of the results.

2D Low-type analytical solutions

To test the ideal MHD module, we also compare our numerical calculations with analytic solutions found by Low (1984). One of them has been used in

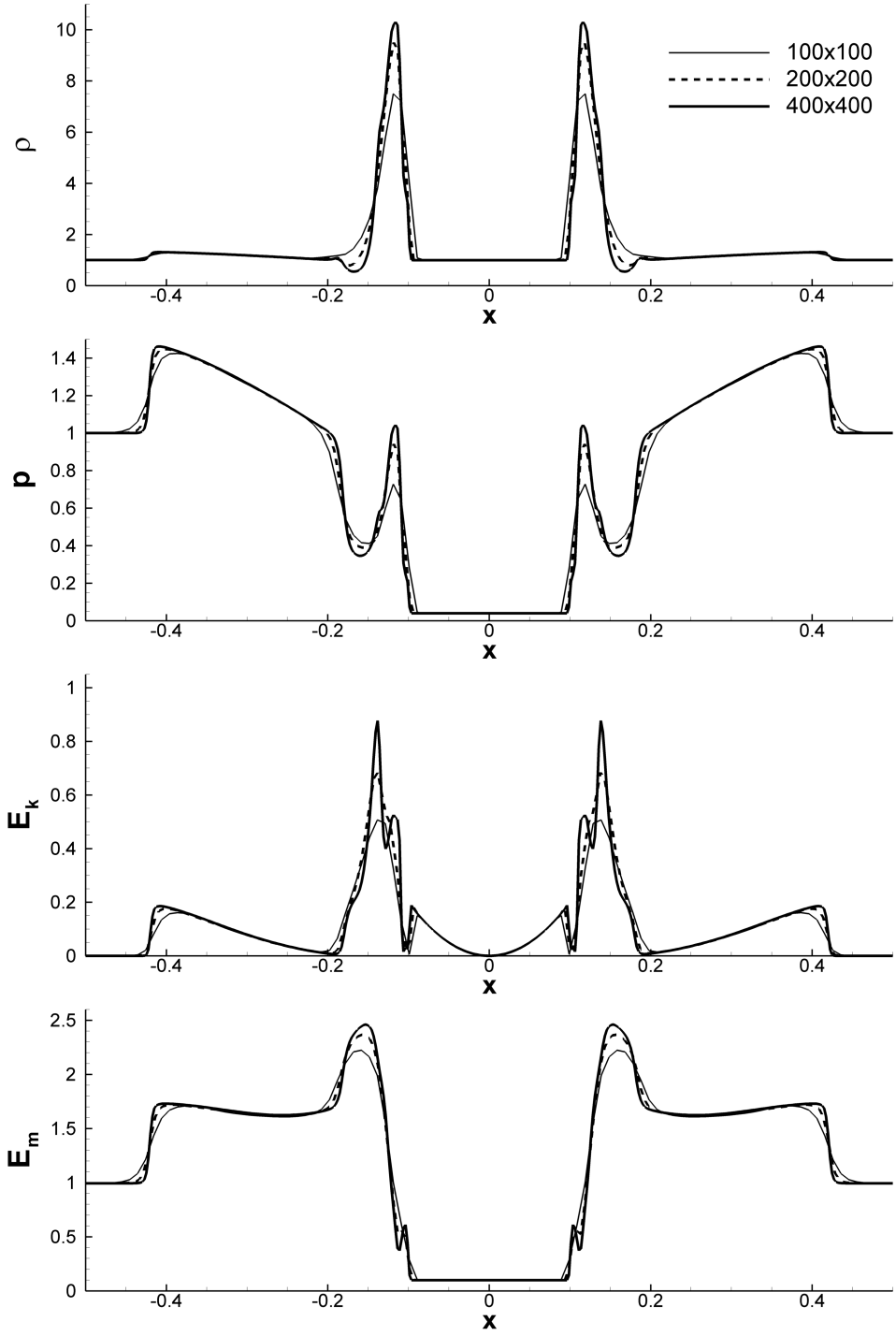

Figure 3.6 Slices of the density ρ, pressure p, kinetic energy, E_k and magnetic energy E_m along a horizontal line at the center of the rotor at time $t = 0.15$.

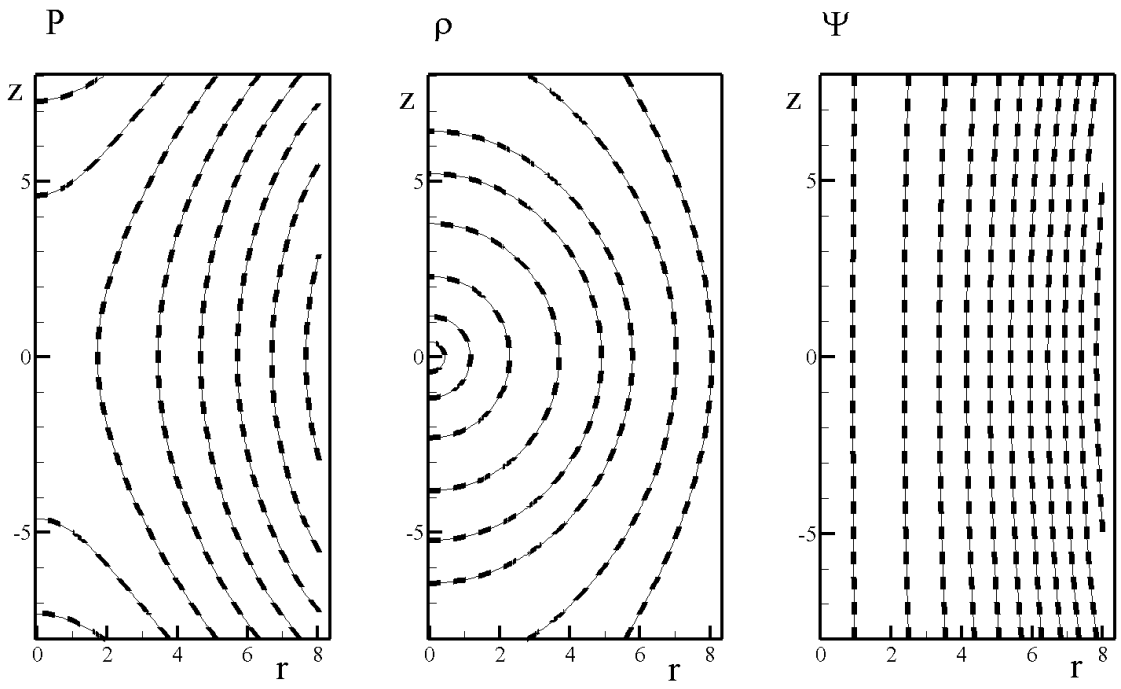

Figure 3.7 The test of the ideal MHD module with the Low-type solution using a homogeneous grid with $N_r, N_z = 80 \times 160$. From left to right: contours of the pressure, density and magnetic flux functions at the moment of time when the scaling parameter is $a = 6$. In all of the plots, the solid line shows the numerical solution while the dashed line shows the analytical Low-type solution.

Stone and Norman (1992b) for testing the corresponding module of the *ZEUS* code. It is convenient to write these solutions in spherical coordinates (as we will do below), and then to convert them to cylindrical coordinates.

These solutions are self-similar and assume that the magnetic flux function Ψ has a dependence on the time and radial coordinate of the form $\xi = R/a(t)$. Here a is a time-dependent scaling parameter and ξ is the self-similarity radius. The velocity has only a radial component (in the spherical coordinate system) which depends linearly on the radius. The function $a(t)$ satisfies the equation $\frac{1}{2}\left(\frac{da}{dt}\right)^2 + \frac{\alpha}{a} = \beta$, and the magnetic flux function satisfies the Grad-Shafranov

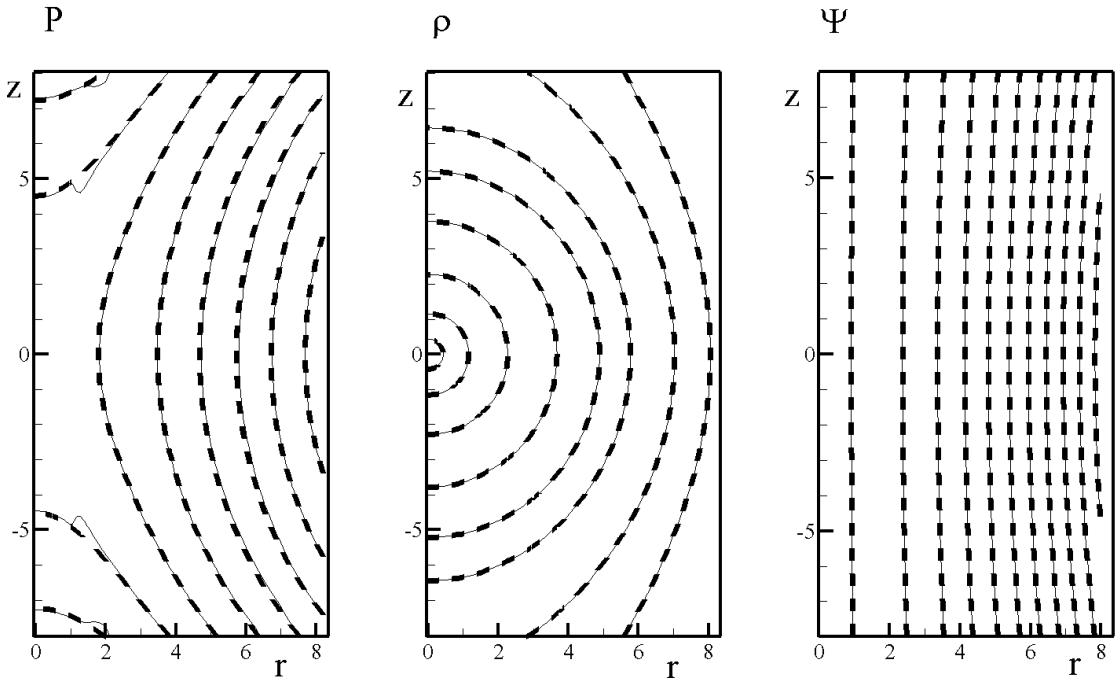

Figure 3.8 The same as in Fig. 3.7, but using an inhomogeneous grid with $N_r, N_z = 40 \times 80$.

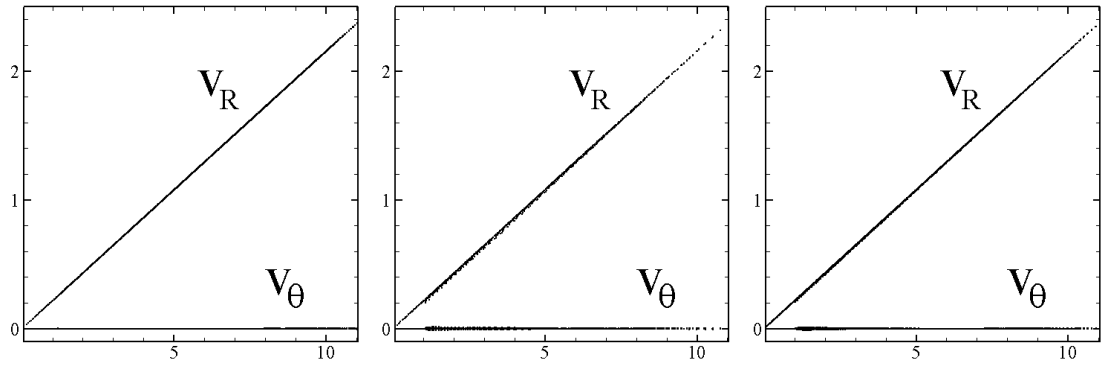

Figure 3.9 The test of the ideal MHD module using the Low-type solution on a homogeneous grid with $N_r, N_z = 80 \times 160$. The dependence of the radial component of velocities and components perpendicular to the radius on the spherical radius for all grid cells.

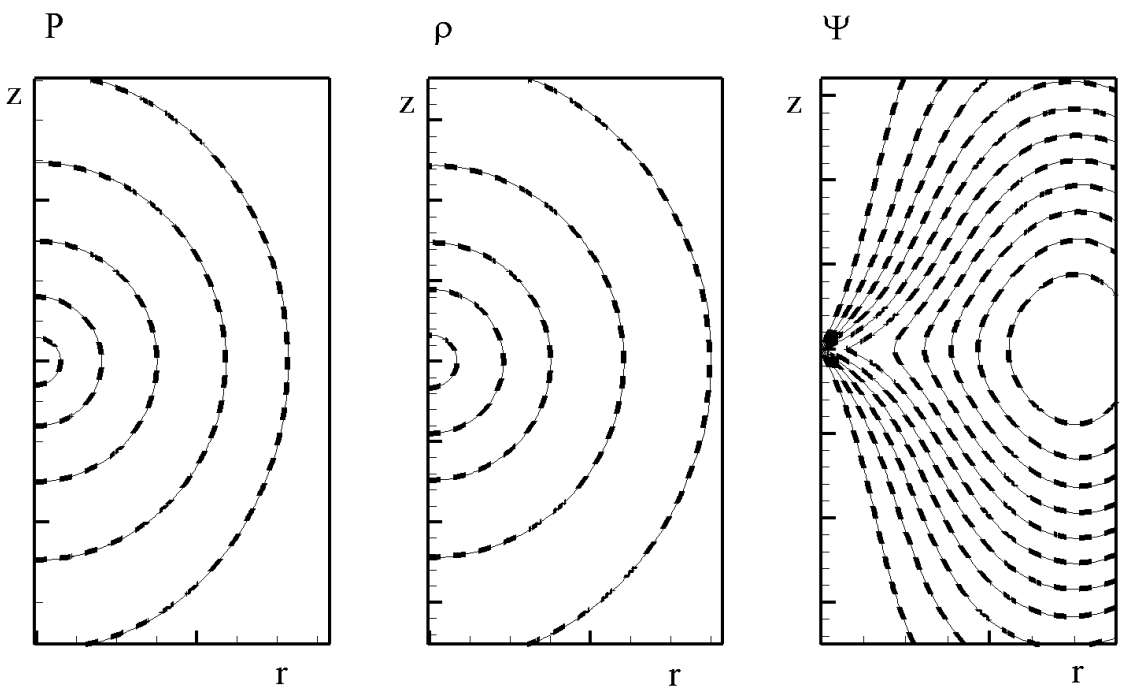

Figure 3.10 The test of the ideal MHD module with the solution of Stone and Norman (1992b) on a homogeneous grid with $N_r, N_z = 70 \times 140$. From left to right: pressure, density and magnetic flux function at the moment of time when the scaling parameter is $a = 6$. In all plots, the solid line shows the numerical solution and the dashed line shows the analytical solution.

equation[3]. The other variables are connected with $a(t)$ and Ψ and their derivatives by algebraic relationships. The first solution proposed by Lou et al. (1987) and used for testing does not have an azimuthal component of the magnetic field. The second solution used in Stone and Norman (1992b) has a non-zero azimuthal magnetic field B_ϕ, but the motion of the plasma is inertial.

In the first solution, Lou et al. (1987) chose growing solutions of the function $a(t)$

$$\frac{da}{dt} = \sqrt{2\left(\beta - \frac{\alpha}{a}\right)} \tag{3.64}$$

[3]The Grad-Shafranov equation is the equilibrium condition in a 2D MHD plasma. We do not describe it here in detail because it is outside the scope of this work.

The magnetic flux function has the form

$$\Psi = C\xi^2\left(\xi^2 - \xi_0^2\right)^2 \sin^2\theta. \tag{3.65}$$

The poloidal components of the magnetic field are calculated via:

$$B_R = \frac{2C\cos\theta}{a^2}\left(\xi^2 - \xi_0^2\right)^2 \tag{3.66}$$

and

$$B_\theta = -\frac{2C\sin\theta}{a^2}\left(\xi^2 - \xi_0^2\right)\left(3\xi^2 - \xi_0^2\right). \tag{3.67}$$

The initial pressure and density are

$$p = \frac{C^2}{\pi a^4}\left[\left(5\xi_0^2 - 7\xi^2\right)\left(\xi^2 - \xi_0^2\right)\xi^2\sin^2\theta - \xi_0^6\right]\left(\xi^2 - \xi_0^2\right) \tag{3.68}$$

and

$$\rho = \frac{2C^2\xi}{\pi a^3\left(\alpha\xi + \dfrac{GM}{\xi^2}\right)}\left[7\left(\xi^2 - \xi_0^2\right)^2\xi^2\sin^2\theta + \xi_0^6\right]. \tag{3.69}$$

The radial velocity is given by: $v_R = \xi\sqrt{2\left(\beta - \frac{\alpha}{a}\right)}$. We also take the following parameters for the problem: $GM = 1$, $C = 1$, $\alpha = 1$, $\beta = 1$, and $\xi_0 = 6$; the adiabatic index is $\gamma = 4/3$.

The solution is numerically computed over the region $0 < r < 8$, $-8 < z < 8$ with a rectangular region, $0 < r < 1$, $-1 < z < 1$ excised from the simulation. We use two grids: a homogeneous grid, with $N_r \times N_z = 80 \times 160$, and an inhomogeneous grid, 40×80. In both cases, the excised rectangular region is homogeneous, with dimensions 10×10, though values are not computed in this region. Thus, the cell sizes of the homogenous grid are $\Delta r = 0.1$ and $\Delta z = 0.1$. For the inhomogeneous grid, the grid size is increased in a geometrical progression with the power $q = 1.05$. The integration time-step has been chosen automatically such that $\Delta t = 0.5\Delta t_{CFL}$. The function $a(t)$ is determined by numerically

integrating Eqn. 3.64 with the initial condition $a(0) = 2$ at sufficiently fine grid resolution. As an initial condition, the analytical solution is used with the parameter $a = 2$. For boundary conditions, we also use the analytical solution for all variables with the parameter a corresponding to the moment of time. The simulations were performed up to the moment of time when $a = 6$. Fig. 3.7 and Fig. 3.8 from left to right show the pressure, density and magnetic flux function at the moment of time when the scaling parameter is $a = 6$. Fig. 3.7 shows the result of the simulations on a homogeneous grid, while Fig. 3.8 shows the results for the inhomogeneous grid. In all of the plots, the solid line shows the numerical solution and the dashed line shows the analytical solution. Fig. 3.9 shows the radial and transverse components of the velocities as a function of the spherical radius. One can see that the velocity is directed along the radial direction and is proportional to the radius with the high accuracy.

In the second solution (Stone and Norman 1992b) the scaling factor linearly depends on time, $a(t) = t\sqrt{\eta}$. In this case, the magnetic flux function has the form

$$\Psi = \begin{cases} A_0 \left(p_0 + \dfrac{\sin \lambda\xi}{\lambda\xi} - \cos \lambda\xi \right) \sin^2 \theta & \xi < \xi_c \\ 0 & \xi > \xi_c \, . \end{cases}$$

The poloidal components of the magnetic field (in spherical coordinates) can be calculated using the analytic solution:

$$B_R = \begin{cases} \dfrac{2A_0 \cos\theta}{R^2} \left(p_0 + \frac{\sin \lambda\xi}{\lambda\xi} - \cos \lambda\xi \right), & \xi < \xi_c \\ 0, & \xi > \xi_c. \end{cases} \tag{3.70}$$

and

$$B_\theta = \begin{cases} -\dfrac{\lambda A_0 \sin\theta}{aR} \left(\sin \lambda\xi + \frac{\cos \lambda\xi}{\lambda\xi} - \frac{\sin \lambda\xi}{\lambda^2\xi^2} \right), & \xi < \xi_c \\ 0, & \xi > \xi_c. \end{cases} \tag{3.71}$$

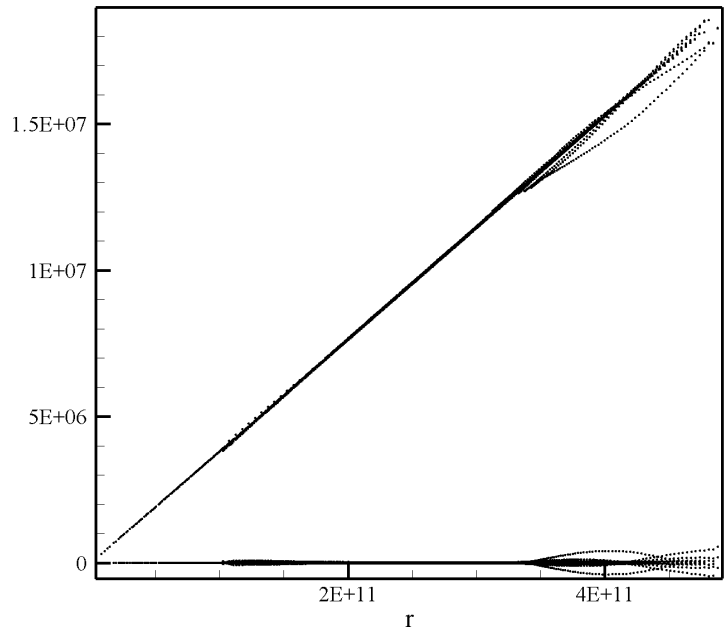

Figure 3.11 The test of the ideal MHD module using the solution of Stone and Norman (1992b) on a homogeneous grid with $N_r, N_z = 70 \times 140$. The dependence of the radial component of velocities and components is perpendicular to the radius on the spherical radius for all grid cells.

The azimuthal component of the magnetic field is

$$B_\phi = \frac{\lambda\Psi}{a^2 R \sin\theta} = \begin{cases} \frac{\lambda A_0 \sin\theta}{aR}\left(p_0 + \frac{\sin\lambda\xi}{\lambda\xi} - \cos\lambda\xi\right), & \xi < \xi_c \\ 0, & \xi > \xi_c. \end{cases} \tag{3.72}$$

The density is given by

$$\rho = \rho_s + \frac{A_0^2 p_0}{2\pi G M R^3}(4 - \lambda^2\xi^2)\left(p_0 + \frac{\sin\lambda\xi}{\lambda\xi} - \cos\lambda\xi\right)\sin^2\theta, \tag{3.73}$$

where

$$\rho_s = \begin{cases} \left(\frac{GM}{\nu R}\right)^3 & \xi < \xi_c \\ \frac{7d_0}{a^3}\left(\frac{R_0}{\xi}\right)^8 & \xi > \xi_c. \end{cases} \tag{3.74}$$

The pressure is given by

$$p = p_s + \frac{A_0^2 p_0}{4\pi R^4}(2 - \lambda^2\xi^2)\left(p_0 + \frac{\sin\lambda\xi}{\lambda\xi} - \cos\lambda\xi\right)\sin^2\theta, \tag{3.75}$$

where $d_0 = 10^8 m_p \exp\left(-\frac{2GM}{3\eta R_0^3}\right)$, $m_p = 1.673 \times 10^{-24}$ g, and

$$p_s = \begin{cases} \frac{GM\rho_s}{4R}, & \xi < \xi_c \\ \frac{7d_0\eta R_0^2}{6a^4}\exp\left(\frac{2GM}{3\eta R_0^3}\left(\frac{R_0}{\xi}\right)^9\right), & \xi > \xi_c. \end{cases} \tag{3.76}$$

The radial velocity is simply $v_r = \xi\sqrt{\eta} = R/t$.

The parameters of the problem are assigned the following values: $M = 2 \times 10^{33}$ g, $\eta = 5.24 \times 10^{-8}$ sec^{-2}, $\lambda = 5.54 \times 10^{-11}$ cm^{-1}, $\xi_c = 1.104 \times 10^{11}$ cm, $\nu = 2.42 \times 10^{20}$ cm^3 sec^{-2} g$^{-1/3}$, $A_0 = 1.5 \times 10^{21}$ G cm^2, $p_0 = \cos\lambda\xi_c - \frac{\sin\lambda\xi_c}{\lambda\xi_c} = 1.01327$, and $R_0 = 10^{11}$ cm; the adiabatic index is $\gamma = 4/3$.

The equations of ideal MHD are integrated in the region $0 < r < 3.5 \times 10^{11}$ cm, -3.5×10^{11} cm $< z < 3.5 \times 10^{11}$ cm, where an inner rectangle with size $0 < r < 10^{11}$ cm, -10^{11} cm $< z < 10^{11}$ cm has been excised from the region. We use the homogeneous grid 70×140, and the grid in the excised region is 20×20. Thus, the cell size is $\Delta r = 0.05 \times 10^{11}$ cm and $\Delta z = 0.05 \times 10^{11}$ cm. The time-step is chosen automatically such that $\Delta t = 0.5\Delta t_{CFL}$. As an initial condition, we take the analytical solution described above for $a = 2$. We use the analytical solution for the boundary conditions, taking the parameter a to correspond to the moment of time. The calculations are done up to the moment when the scaling parameter reaches the value $a = 6$. As before, Fig. 3.10 and Fig. 3.11 show the results of simulations at the moment when the scaling parameter becomes equal to $a = 6$.

3.3 2D polar geometry

To describe the interaction of the accretion disk with a planet in the presence of a magnetic field, we use a model which describes the processes in terms of surface variables (density and pressure). The equations for this model are obtained by integrating the three-dimensional MHD equations along the $z-$direction which is perpendicular to the disk plane. Again, we assume that the $z-$components of the velocity and the magnetic field are zero and there is no field outside the disk.

3.4 MHD Equations

We utilize the MHD equations to numerically evaluate the perturbative effect of the planet on the disk:

1. Continuity equation (conservation of mass)

$$\frac{\partial \Sigma}{\partial t} + \frac{1}{r}\frac{\partial}{\partial r}(r\Sigma v_r) + \frac{1}{r}\frac{\partial}{\partial \varphi}(\Sigma v_\varphi) = 0, \tag{3.77}$$

   where $\Sigma = \int \rho dz$ is the surface density (with ρ the volume density), and v_r and v_φ are the radial and azimuthal velocities, respectively.

2. Radial equation of motion (conservation of momentum)

$$\begin{aligned} \frac{\partial}{\partial t}(\Sigma v_r) &+ \frac{1}{r}\frac{\partial}{\partial r}\left[r\left(\Sigma v_r^2 + \Pi + \frac{\Psi_{rr}+\Psi_{\varphi\varphi}}{8\pi} - \frac{\Psi_{rr}}{4\pi}\right)\right] \\ &+ \frac{1}{r}\frac{\partial}{\partial \varphi}\left(\Sigma v_r v_\varphi - \frac{\Psi_{r\varphi}}{4\pi}\right) \\ &= \frac{\Pi}{r} + \frac{\Psi_{rr}+\Psi_{\varphi\varphi}}{8\pi r} - \Sigma\frac{GM_\star}{r^2} + \Sigma w_r, \end{aligned} \tag{3.78}$$

where $\Pi = \int P dz$ is the surface pressure (with P the volume pressure), Σw_r is the radial force exerted on the disk by the planet (per unit area of the disk), and Ψ_{rr}, $\Psi_{r\varphi}$, and $\Psi_{\varphi\varphi}$ are magnetic surface variables that are discussed in more detail in §3.4.

3. Azimuthal equation of motion (conservation of angular momentum)

$$\begin{aligned} \frac{\partial}{\partial t}(\Sigma v_\varphi) &+ \frac{1}{r^2}\frac{\partial}{\partial r}\left[r^2\left(\Sigma v_r v_\varphi - \frac{\Psi_{r\varphi}}{4\pi}\right)\right] \\ &+ \frac{1}{r}\frac{\partial}{\partial \varphi}\left(\Sigma v_\varphi^2 + \Pi + \frac{\Psi_{rr}+\Psi_{\varphi\varphi}}{8\pi} - \frac{\Psi_{\varphi\varphi}}{4\pi}\right) \\ &= \Sigma w_\varphi, \end{aligned} \tag{3.79}$$

where Σw_φ is the azimuthal force exerted on the disk by the planet (per unit area of the disk).

4. Radial induction equation

$$\frac{\partial \Phi_r}{\partial t} + \frac{1}{r}\frac{\partial}{\partial \varphi}\left(v_\varphi \Phi_r - v_r \Phi_\varphi\right) = 0, \tag{3.80}$$

where Φ_r and Φ_φ are magnetic surface variables, also discussed in §3.4.

5. Azimuthal induction equation

$$\frac{\partial \Phi_\varphi}{\partial t} + \frac{\partial}{\partial r}\left(v_r \Phi_\varphi - v_\varphi \Phi_r\right) = 0. \tag{3.81}$$

6. Entropy balance equation

$$\frac{\partial}{\partial t}(\Sigma S) + \frac{1}{r}\frac{\partial}{\partial r}(r \Sigma S v_r) + \frac{1}{r}\frac{\partial}{\partial \varphi}(\Sigma S v_\varphi) = 0, \tag{3.82}$$

where $S = \Pi/\Sigma^\gamma$ is a function analogous to entropy, and we use $\gamma = 1.01$ so that our disk is isothermal. We chose an isothermal disk to ease comparisons of our results with the results of other authors (e.g., by Fromang et al. 2005).

Moreover, viscosity terms were added to the equations of motion following the α prescription of Shakura and Sunyaev (1973) (see details in Koldoba et al. 2015). We use a very small viscosity ($\alpha = 0.001$), analogous to Fromang et al. (2005), to isolate the effects of slow magnetosonic waves in the disk by smoothing out the effects of fast magnetosonic waves.

Magnetic surface variables

The "volume" values for the radial and azimuthal magnetic fields are given by B_r and B_φ. Their vertically-integrated counterparts may be defined similarly to Σ and Π as

$$\Phi_r = \int B_r dz \qquad \text{and} \qquad \Phi_\varphi = \int B_\varphi dz, \tag{3.83}$$

respectively. There are also terms in the MHD equations involving magnetic flux or energy that involve products of these variables: B_r^2, B_φ^2, and $B_r B_\varphi$. We define the following vertically-integrated quantities for these products,

$$\Psi_{rr} = \int B_r^2 dz, \qquad \Psi_{\varphi\varphi} = \int B_\varphi^2 dz, \qquad \text{and} \qquad \Psi_{r\varphi} = \int B_r B_\varphi dz, \tag{3.84}$$

respectively.

As shown in Eqn. 3.78 - Eqn. 3.81, the induction equations use Φ_r and Φ_φ, while the equations of motion use Ψ_{rr}, $\Psi_{r\varphi}$, and $\Psi_{\varphi\varphi}$. As such, we need a way to relate Φ and Ψ. We can do this by introducing a "magnetic" thickness of the disk, h_m. Using the definitions of Φ and Ψ, with h_m, we find that

$$\Psi_{rr} = \frac{\Phi_r \Phi_r}{h_m}; \qquad \Psi_{r\varphi} = \frac{\Phi_r \Phi_\varphi}{h_m}; \qquad \Psi_{\varphi\varphi} = \frac{\Phi_\varphi \Phi_\varphi}{h_m}. \tag{3.85}$$

We suggest that the value of $h_m = \text{const}$ is the same in all three relations. By relating Φ and Ψ in this way, we can define a "surface magnetic field", $\mathfrak{B}$, such

that the MHD equations are parameterized with respect to a single magnetic field variable,

$$\mathfrak{B}_r = \frac{\Phi_r}{\sqrt{h_m}} \qquad \text{and} \qquad \mathfrak{B}_\varphi = \frac{\Phi_\varphi}{\sqrt{h_m}}. \tag{3.86}$$

Then, the magnetic terms in Eqn. 3.78 - Eqn. 3.81 take their usual form.

The radial equation of motion becomes

$$\begin{aligned}\frac{\partial}{\partial t}(\Sigma v_r) \quad &+ \quad \frac{1}{r}\frac{\partial}{\partial r}\left[r\left(\Sigma v_r^2 + \Pi + \frac{\mathfrak{B}_r^2 + \mathfrak{B}_\varphi^2}{8\pi} - \frac{\mathfrak{B}_r^2}{4\pi}\right)\right] + \frac{1}{r}\frac{\partial}{\partial \varphi}\left(\Sigma v_r v_\varphi - \frac{\mathfrak{B}_r \mathfrak{B}_\varphi}{4\pi}\right) \\ &= \quad \frac{\Sigma v_\varphi^2}{r} + \frac{\Pi}{r} + \frac{\mathfrak{B}_r^2 + \mathfrak{B}_\varphi^2}{8\pi r} - \Sigma\frac{GM_\star}{r^2} + \Sigma w_r,\end{aligned} \tag{3.87}$$

and the azimuthal equation of motion becomes

$$\frac{\partial}{\partial t}(\Sigma v_\varphi) + \frac{1}{r^2}\frac{\partial}{\partial r}\left[r^2\left(\Sigma v_r v_\varphi - \frac{\mathfrak{B}_r \mathfrak{B}_\varphi}{4\pi}\right)\right] + \frac{1}{r}\frac{\partial}{\partial \varphi}\left(\Sigma v_\varphi^2 + \Pi + \frac{\mathfrak{B}_r^2 + \mathfrak{B}_\varphi^2}{8\pi} - \frac{\mathfrak{B}_\varphi^2}{4\pi}\right) = \Sigma w_\varphi. \tag{3.88}$$

The radial and azimuthal induction equations become, respectively,

$$\frac{\partial \mathfrak{B}_r}{\partial t} + \frac{1}{r}\frac{\partial}{\partial \varphi}\left(v_\varphi \mathfrak{B}_r - v_r \mathfrak{B}_\varphi\right) = 0 \tag{3.89}$$

and

$$\frac{\partial \mathfrak{B}_\varphi}{\partial t} + \frac{\partial}{\partial r}\left(v_r \mathfrak{B}_\varphi - v_\varphi \mathfrak{B}_r\right) = 0. \tag{3.90}$$

3.4.1 Grid and boundary conditions

We use a polar grid that is uniform in the φ direction. In the r direction, however, the grid is non-uniform; the size of the grid cells increases with radius such that the sides are approximately square-shaped throughout the disk. N_r is defined to be the number of radial grid cells, and N_φ is the number of azimuthal grid cells. Our grid consists of $N_r = 480$ and $N_\varphi = 1200$ cells. Our inner boundary is at $r_{\rm in} = 0.4 r_{{\rm p},i}$, and our outer boundary is at $r_{\rm out} = 5 r_{{\rm p},i}$.

We apply a wave damping procedure near both boundaries similar to that used in §3.1.3 of Fromang et al. (2005) to avoid high-amplitude wave reflections that can overwhelm the migration signal. We perform damping after every time step for $r < r_{\rm damp,in}$, and $r > r_{\rm damp,out}$, where $r_{\rm damp,in} = 1.375 r_{\rm in}$ and $r_{\rm damp,out} = 0.8 r_{\rm out}$. We calculate the velocities (v_r, v_φ), as well as Σ, Π, and S, using a method similar to Fromang et al. (2005),

$$\vec{\mathcal{J}} = \begin{cases} \mathcal{J}_{\rm in} + (\mathcal{J} - \mathcal{J}_{\rm in}) \exp\left[-\left(\frac{r - r_{\rm damp,in}}{\delta_{\rm in}} \right)^2 \right] & r < r_{\rm damp,in} \\ \mathcal{J}_{\rm out} + (\mathcal{J} - \mathcal{J}_{\rm out}) \exp\left[-\left(\frac{r - r_{\rm damp,out}}{\delta_{\rm out}} \right)^2 \right] & r > r_{\rm damp,out} \\ \mathcal{J} & \text{otherwise,} \end{cases} \tag{3.91}$$

where $\vec{\mathcal{J}} = \left(v_r, v_\varphi, \Sigma, \Pi, S \right)$, $\delta_{\rm in} = 0.875 r_{\rm in}$, and $\delta_{\rm out} = 0.8 r_{\rm out}$. Furthermore, $\mathcal{J}_{\rm in}$ and $\mathcal{J}_{\rm out}$ are the values of $\mathcal{J}$ at the inner and outer disk boundaries, respectively.

3.4.2 Initial conditions

The initial conditions for the surface density, surface pressure and surface "magnetic field" are defined to be power laws

$$\Sigma = \Sigma_i \left(\frac{r}{r_i} \right)^{-n}, \tag{3.92}$$

$$\Pi = \Pi_i \left(\frac{r}{r_i} \right)^{-l}, \quad \text{and} \tag{3.93}$$

$$\mathfrak{B}_\varphi = \mathfrak{B}_{\varphi,i} \left(\frac{r}{r_i} \right)^{-k}, \tag{3.94}$$

where r_i is a characteristic radius in the disk; in most of our simulations $r_i = r_{{\rm p},i}$ is the initial location of the planet. Additionally, n, l, and k are the power laws in the density, pressure, and magnetic field distributions, respectively. We suggest that the initial pressure distribution is similar to the initial density distribution

(i.e., $n = l$). The initial sound speed in the disk at r_i, defined as a fraction of the Keplerian speed at this radius, k_s, is

$$c_i^2 = k_s \frac{GM_\star}{r_i}, \tag{3.95}$$

where $k_s = 0.01$. The initial surface pressure at r_i is $\Pi_i = \Sigma_i c_i^2$. The initial plasma parameter at r_i is then defined as

$$\beta_i = \frac{8\pi\Pi_i}{\mathfrak{B}_{\varphi,i}^2}. \tag{3.96}$$

Note again that this plasma parameter, β_i, is twice as large as the plasma parameter defined in Fromang et al. (2005). We determine the surface magnetic field distribution via

$$\mathfrak{B}_{\varphi,i} = \sqrt{\frac{8\pi\Pi_i}{\beta_i}}. \tag{3.97}$$

We determine the initial equilibrium in the disk from the force balance in the radial direction:

$$-\frac{v_\varphi^2}{r} + \frac{1}{\Sigma}\frac{d\Pi}{dr} + \frac{1}{8\pi r^2 \Sigma}\frac{d(r\mathfrak{B}_\varphi)^2}{dr} + \frac{GM_\star}{r^2} = 0. \tag{3.98}$$

It is satisfied if the initial distribution of the azimuthal velocity has the form

$$v_\varphi^2 = \frac{GM_\star}{r} + c_i^2 \left(\frac{r}{r_i}\right)^n \left[-n\left(\frac{r_i}{r}\right)^n + \frac{1-k}{\beta_i}\left(\frac{r_i}{r}\right)^{2k} \right]. \tag{3.99}$$

For all of the simulations presented here, we took $k_s = 0.01$. The thickness of the disk at r_i is $H_i = \sqrt{k_s r_i}$. The smoothing radius of the gravitational potential is $\epsilon = 0.1H$. An initial plasma parameter of $\beta_i = 1, 2$ is taken for analysis of migration in laminar MHD disks, while we increase β_i up to $\beta_i = 100$ to study migration in a turbulent disk. We consider the migration of a $5M_\oplus$ planet in most of the simulations, as well as a $20M_\oplus$ planet in a few simulations.

3.5 Planetary equation of motion

We calculate the equations of motion in the stellar reference frame, which is not inertial because the star also revolves about the center of mass of the system. So, an inertial force term is added to the equation of motion for both the disk and the planet. Assuming that the inertial acceleration is only due to the gravitational attraction between the star and the planet (but not the disk), the inertial force per unit mass (i.e., acceleration) is

$$\mathbf{w}_i = -\frac{GM_\mathrm{p}}{r_\mathrm{p}^3}\mathbf{r}_\mathrm{p}. \tag{3.100}$$

To describe the gravitational influence of the planet on the disk, we use a gravitational potential similar to that used by Fromang et al. (2005),

$$\Phi_\mathrm{p} = -\frac{GM_\mathrm{p}}{\sqrt{r^2 + r_\mathrm{p}^2 - 2rr_\mathrm{p}\cos(\varphi - \varphi_\mathrm{p}) + \epsilon^2}}, \tag{3.101}$$

where $\epsilon = 0.1H$ is the gravitational smoothing length, and H is the scale height of the disk. The total force per unit mass is

$$\mathbf{w} = \mathbf{w}_p + \mathbf{w}_i, \quad \mathbf{w}_p = -\nabla\Phi_\mathrm{p}. \tag{3.102}$$

The components of this force in polar coordinates, w_r and w_φ, are used in Eqn. 3.87 and Eqn. 3.88.

The force exerted *on* the planet by a particular fluid element with mass $dM = \Sigma r dr d\varphi$, is the acceleration given in Eqn. 3.102, with opposite sign, multiplied by the mass of the fluid element,

$$d\mathbf{f}_{\mathrm{disk}\to\mathrm{p}} = -dM\mathbf{w}_p = dM\nabla\Phi_\mathrm{p}. \tag{3.103}$$

We then calculate the total force exerted on the planet by the disk by integrating over the disk within the computational domain,

$$\mathbf{F}_{\mathrm{disk}\to\mathrm{p}} = \int_\mathrm{disk} d\mathbf{f}_{\mathrm{disk}\to\mathrm{p}} = \int_\mathrm{disk} dM\nabla\Phi_\mathrm{p}, \tag{3.104}$$

which we use to find the position ($\mathbf{r}_\mathrm{p}$) and velocity ($\mathbf{v}_\mathrm{p}$) of the planet at each time step via the planet's equation of motion:

$$M_p \frac{d\mathbf{v}_\mathrm{p}}{dt} = -\frac{GM_\star M_\mathrm{p}}{r_\mathrm{p}^3}\mathbf{r}_\mathrm{p} - \frac{GM_\mathrm{p}^2}{r_\mathrm{p}^3}\mathbf{r}_\mathrm{p} + \mathbf{F}_{\mathrm{disk}\to\mathrm{p}}. \tag{3.105}$$

The gravitational torque in the z direction on the planet is the sum over the torques from each fluid element:

$$T_z = \int_\mathrm{disk} \left[\mathbf{r} \times d\mathbf{f}_{\mathrm{disk}\to\mathrm{p}}\right]_z. \tag{3.106}$$

We also calculate the planet's orbital energy and angular momentum per unit mass (e.g., Murray and Dermott 1999) via

$$E = \frac{1}{2}|\mathbf{v}_\mathrm{p}|^2 - \frac{GM_\star}{r_\mathrm{p}} \qquad \text{and} \qquad L = \mathbf{r}_\mathrm{p} \times \mathbf{v}_\mathrm{p}, \tag{3.107}$$

respectively. We use these relationships to calculate the semimajor axis and eccentricity of the planet's orbit at each time step,

$$a = -\frac{1}{2}\frac{GM_\star}{E} \qquad \text{and} \qquad e = \sqrt{1 - \frac{L^2}{GM_\star a}}, \tag{3.108}$$

respectively.

3.6 Reference Units

Our simulations are performed using dimensionless units $\widetilde{A} = A/A_0$ where A_0 are the reference units. We first choose some reference distance, r_0. The results of our simulations are applicable to multiple regions in a protoplanetary disk, because r_0 can be chosen to correspond to different regions of the disk. In Table 3.1, we show examples of reference values for scale distances of $r_0 = 0.1$ AU and $r_0 = 1$ AU. The thickness of the disk is $H = 0.1r_0$. We take the mass of the star,

Variable Definitions	
r_0	Reference distance
v_0	Reference velocity
P_0	Reference orbital period
$M_{\rm d0}$	Reference disk mass
Σ_0	Reference surface density
B_0	Reference magnetic field strength
T_0	Reference torque per unit mass

(a)

Standard reference values		
	r_0 = 0.1 AU	r_0 = 1 AU
v_0	94.1 km s^{-1}	29.8 km s^{-1}
P_0	11.6 days	367 days
$M_{\rm d0}$	$1 M_\odot$	$1 M_\odot$
Σ_0	8.84×10^8 g cm^{-2}	8.84×10^6 g cm^{-2}
B_0	228 kG	2.28 kG
T_0	8.85×10^{13} cm^2 s^{-2}	8.85×10^{12} cm^2 s^{-2}

(b)

Rescaled reference values		
	r_0 = 0.1 AU	r_0 = 1 AU
v_0	94.1 km s^{-1}	29.8 km s^{-1}
P_0	11.6 days	367 days
$M_{\rm d0}$	$10^{-3} M_\odot$	$10^{-3} M_\odot$
Σ_0	8.84×10^5 g cm^{-2}	8.84×10^3 g cm^{-2}
B_0	7.22 kG	72.2 G
T_0	8.85×10^{13} cm^2 s^{-2}	8.85×10^{12} cm^2 s^{-2}

(c)

Table 3.1 Example reference units calculation. The stellar mass is $M_\star = 1 M_\odot$. (a) Definitions of the variables used. (b) Standard reference values, corresponding to $\widetilde{\Sigma} = 1$. (c) Rescaled reference values, corresponding to $\widetilde{\Sigma} = 0.001$, which is the value used in the code.

$M_\star = 1 M_\odot$, and determine the reference velocity, which is the Keplerian velocity at r_0, $v_0 = \sqrt{GM_\star/r_0}$. The reference time is $t_0 = r_0/v_0$, and we use the reference orbital period $P_0 = 2\pi t_0$ as the unit of time in our plots.

We next define the reference mass of the disk M_{d0}: $M_{\rm d0} = M_\star$. We then introduce the reference surface density, Σ_0, such that $M_{\rm d0} = \Sigma_0 r_0^2$. When the disk is homogeneous (i.e., $\Sigma = {\rm const}$), $M_{\rm d0}$ is the mass of the disk inside $r = r_0$. The reference surface pressure is $\Pi_0 = \Sigma_0 v_0^2$.

The reference surface magnetic field is derived from the condition $\Sigma_0 v_0^2 = \mathfrak{B}_0^2$. Hence, $\mathfrak{B}_0 = \sqrt{\Sigma_0 v_0^2}$. Taking into account our definitions of the surface magnetic field (see Eqn. 3.83 and Eqn. 3.84), we obtain the reference volume magnetic field: $B_0 = \mathfrak{B}_0/\sqrt{r_0}$. The reference torque per unit mass is defined as $T_0 = r_0^2/t_0^2$. These reference units are used to convert equations from dimensionless units. We show examples in Table 3.1b.

In our model, we use a small value of the dimensionless density $\widetilde{\Sigma} = 0.001$; as a result, our dimensional characteristic disk mass is $M_{d0} = 10^{-3} M_\odot$. The other characteristic values are closer to realistic values and are much smaller than the reference values shown in Table 3.1b. We show in Table 3.1c the typical dimensional values corresponding to our simulations. One can see that, in the case of $r_0 = 1$ AU, the surface density and other parameters are close to those expected in real protoplanetary disks. The values shown for $r_0 = 0.1$AU are too large, but we keep these model parameters for all distances in order to compare our results with those in Fromang et al. (2005) and others.[4] From this point forward, we will use only dimensionless units and remove tildes from variables.

[4]It is often the case that the disk mass and the surface density are taken to be larger than in realistic disks. This leads to more rapid migration and thus shorter computational times (see, e.g., Armitage and Rice 2008).

CHAPTER 4

2D SIMULATIONS OF PLANET MIGRATION

4.1 Parameter Space

We calculated a number of models at different initial parameters, which are described below (see also Table 4.1):

Simulation type: The simulations are performed in a hydrodynamic disk or an MHD disk, or to study the interaction between the planet and waves in the disk.

Planet mass: We explored two different planet masses – $5M_{\oplus}$ and $20M_{\oplus}$.

Surface density exponent, n: This defines the initial surface density distribution in the disk, according to $\Sigma \propto r^{-n}$.

Surface magnetic field exponent, k: This defines the initial surface magnetic field distribution in the disk, according to $\mathfrak{B} \propto r^{-k}$.

Matter-to-magnetic pressure ratio, β_i: This defines the value of β_i at the initial location of the planet.

Initial planet location, $r_{\mathrm{p},i}$: This defines the initial orbital radius of the planet.

The last column of Table 4.1 shows the names of the simulations presented in subsequent sections. These names are referenced in the figure captions and related discussion.

Type	$M_{\rm p}$ ($M_\oplus$)	n	k	β_i	$r_{{\rm p},i}$	Name
Hydro	5	−1	–	–	1	H5n-1r1
Hydro	5	−0.5	–	–	1	H5n-0.5r1
Hydro	5	0	–	–	1	H5n0r1
Hydro	5	1	–	–	1	H5n1r1
Hydro	20	−1	–	–	1	H20n-1r1
Hydro	20	−0.5	–	–	1	H20n-0.5r1
Hydro	20	0	–	–	1	H20n0r1
MHD	5	0	0	1	1	M5n0k0β1r1
MHD	5	0	0	2	1	M5n0k0β2r1
MHD	5	0	1	2	1	M5n0k1β2r1
MHD	5	0	2	2	1	M5n0k2β2r1
MHD	5	0	0	10	1	M5n0k0β10r1
MHD	5	0	0	100	1	M5n0k0β100r1
MHD	5	1	0	2	1	M5n1k0β2r1
MHD	5	1	1	1	1	M5n1k1β1r1
MHD	5	1	1	2	1	M5n1k1β2r1
MHD	5	1	1	10	1	M5n1k1β10r1
MHD	5	1	2	2	1	M5n1k2β2r1
MHD	20	0	0	2	1	M20n0k0β2r1
MHD	20	0	1	2	1	M20n0k1β2r1
MHD	20	0	2	2	1	M20n0k2β2r1
Waves	5	0	–	–	2	W5n0k0r2
Waves	5	0	0	100	2	W5n0k0β100r2

Table 4.1 Simulation names and their respective distinguishing variables. See a more detailed description in §4.1.

4.2 Migration in Hydrodynamic Disks

As a first step, we investigated the migration of a planet in a hydrodynamic disk with an initially homogeneous density distribution ($n = 0$); these simulations are used as a base for studying migration in magnetic disks. Fig. 4.1 shows the surface density distribution in the disk after 10 orbits of the planet. The planet excites two density waves at the inner and outer Lindblad resonances (which are shown as black circles in the figure).

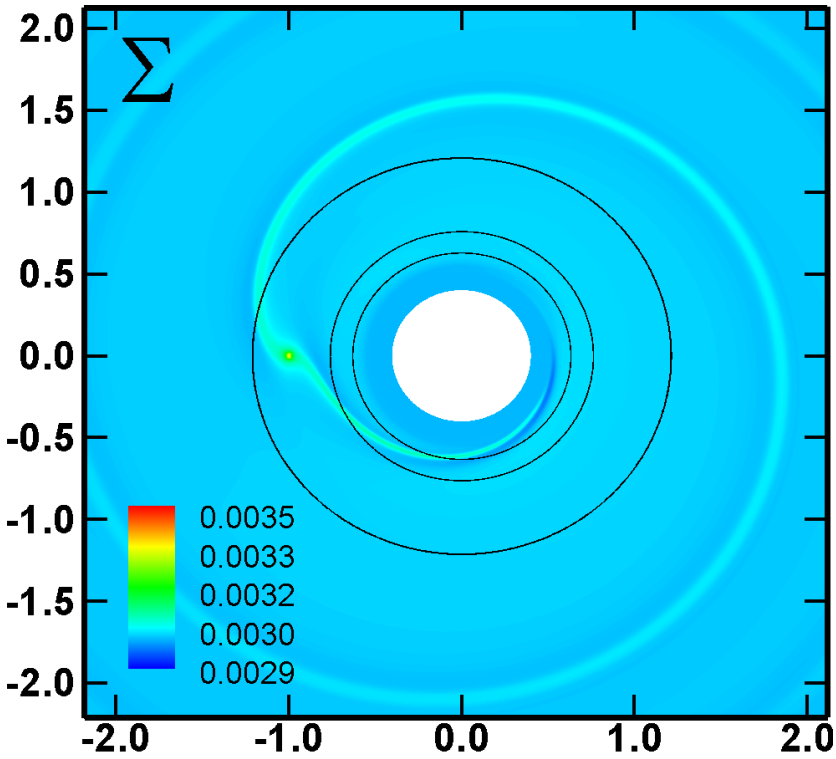

Figure 4.1 An example of a hydrodynamic simulation of migration corresponding to the model H5n0r1 after 10 orbits of the planet. The color background shows the surface density distribution. The $m = 1, 2$ Lindblad resonances are indicated by the solid black circles.

As a next step, we considered different initial density distributions in the disk, $\Sigma \sim r^{-n}$, including those where the density is homogeneous ($n = 0$), increases towards the star ($n = 1$), or decreases toward the star ($n = -0.5, -1$). Fig. 4.2 (top panel) shows the variation of the planet's semimajor axis over time for these cases. We observed inward migration when $n = 0$ and more rapid inward migration when $n = 1$. When $n = -0.5$, the migration almost stalls (where only slow outward migration has been observed), and we observed more rapid outward migration when $n = -1$.

The migration rate and its direction are determined by the cumulative value

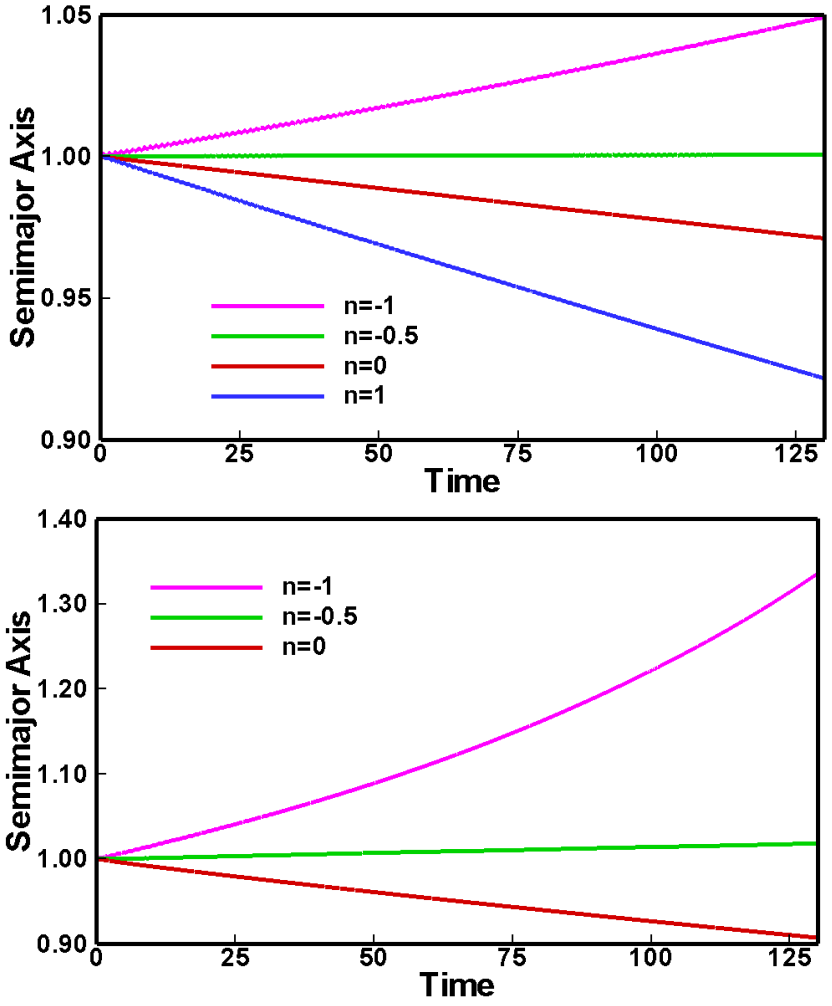

Figure 4.2 *Top Panel:* The variation in semimajor axis versus time for a $5M_{\oplus}$ planet embedded in a hydrodynamic disk for different values of n (where $\Sigma \propto r^{-n}$). The models shown include: H5n0r1, H5n1r1, H5n-1r1, H5n-0.5r1. *Bottom Panel:* A similar plot, but for a $20M_{\oplus}$ planet. The models shown include: H20n-1r1, H20n0r1, H20n-0.5r1.

of the Lindblad and corotation torques, as described in Sec. 2.3. When the density increases towards the star ($n = 1$) or the density is constant in the disk ($n = 0$), the Lindblad torque is larger than the corotation torque, and the planet migrates towards the star. However, when the density *decreases* towards the star, $n = -1$, the corotation torque is larger than the Lindblad torque, and the planet migrates outwards. In the case of a more shallow positive density distribution, $n = -0.5$, the Lindblad and corotation torques are almost equal, and the cumulative torque is small. This results for $n = -0.5$ obtained from our simulations is very close to the value $n = -0.41$ corresponding to zero torque derived by Tanaka et al. (2002) for two dimensions.

We also performed simulations of the migration of a $20M_\oplus$ planet. Fig. 4.2 (bottom panel) shows that the planet migrates inward when $n = 0$; almost no migration is observed when $n = -0.5$ (as with the $5M_\oplus$ planet); and the migration direction is outward when $n = -1$. These results are in accord with that of a $5M_\oplus$ planet, while the migration rate is faster in the $20M_\oplus$ case. This is expected according to Eqn. 2.9, which states that the total Lindblad torque increases with the mass of the planet.

Our simulations of hydrodynamic disks are in accord with theoretical studies (e.g., Tanaka et al. 2002) and simulations performed by others (see review by Kley and Nelson 2012).

4.3 Migration in Laminar MHD disks due to magnetic resonances

4.3.1 Magnetic resonances in the case of a constant density distribution

We performed a series of simulations to investigate the influence of an ordered azimuthal magnetic field in the disk on a planet's migration. We started by investigating migration in disks with a homogeneous surface density distribution (i.e., $n = 0$), with initial and boundary conditions very similar to those used by Fromang et al. (2005). In particular, we considered an isothermal disk (i.e., $\gamma = 1.01$) and set the strength of the magnetic field near the planet such that $\beta_i = 2$. Our goal was to see whether our code can reproduce the results presented by Fromang et al. (2005).

First, we investigated a homogeneous magnetic field (i.e., $k = 0$). Fig. 4.3 shows an example simulation after 10 orbital periods of the planet. We observed that the planet excites ring-like waves at which the azimuthal magnetic field is stronger and the surface density is lower than in other nearby regions in the disk. These locations correspond to the magnetic resonances that are excited by slow magnetosonic waves propagating along the field lines. Fig. 4.3 shows two rings of lower density (top left panel), corresponding to two rings of enhanced azimuthal field (top right panel). The position of the magnetic resonances is similar to that found in the simulations by Fromang et al. (2005), and they correspond to the theoretical resonance locations predicted by Terquem (2003) (see the dashed-line circles in Fig. 4.3). The bottom panels show the linear distribu-

tion of B_φ and Σ in the radial direction.

According to the theory presented by Terquem (2003), these waves exert a torque on the planet that can reverse the planetary migration direction if the magnetic field distribution is steep enough. We varied the steepness of the magnetic field, k (see Eqn. 3.94), taking $k = 0, 1, 2$, and we obtained different migration rates. Fig. 4.4 (top panel) shows that, for a constant magnetic field distribution ($k = 0$), the planet migrates inwards but more slowly than in the purely hydrodynamic case. When $k = 1$, the planet slowly migrates outward, while the planet migrates outward more rapidly when $k = 2$. These simulations confirm the result presented by (Fromang et al. 2005): in disks with a relatively strong azimuthal magnetic field, the magnetic resonances can slow or reverse a planet's migration.

4.3.2 Migration due to magnetic resonances for different density distributions

Next, we investigated the action of the magnetic resonances at different surface density distributions. First, we took a density distribution such that the density in the disk increases towards the star, $n = 1$, and repeated the above simulations at $k = 0, 1, 2$. Fig. 4.4 (middle panel) shows that the planet migrates inward in all three cases and, therefore, that the torque from the magnetic resonances is small compared with the differential Lindblad torque. The migration rate in the case of $k = 1$ almost exactly coincides with the purely hydrodynamic case. For a very steep magnetic field distribution, $k = 2$, the accretion rate is only slightly slower than for $k = 1$. Overall, we conclude that, in the case of this density distribution

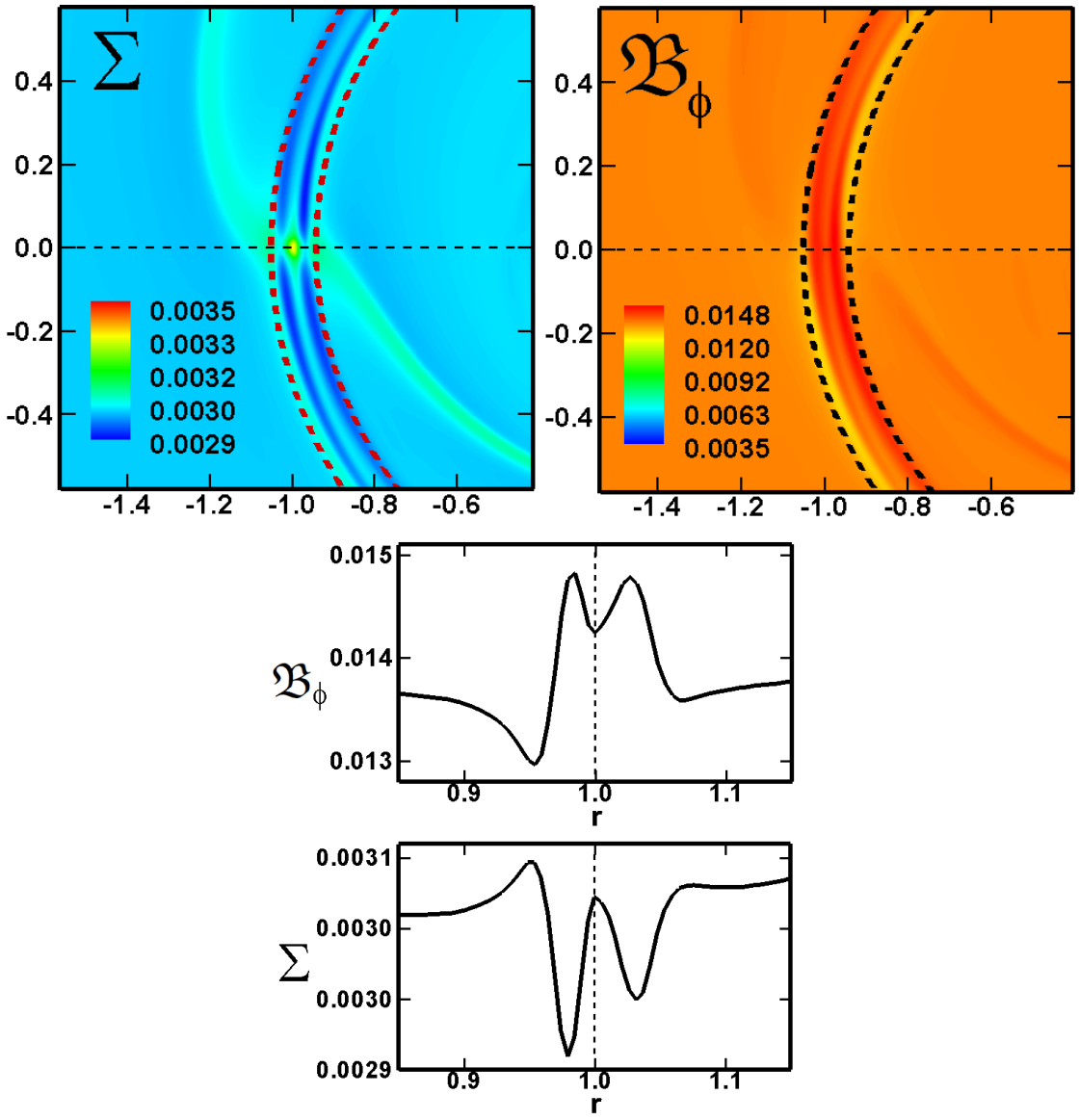

Figure 4.3 The surface density and surface azimuthal magnetic field distributions for the model M5n0k0β2r1 at $t = 10$. *Top Left Panel:* The two-dimensional surface density distribution. The dashed red lines show the positions of the magnetic resonances. *Top Right Panel:* The two-dimensional surface azimuthal magnetic field distribution. The dashed black lines show the positions of the magnetic resonances. *Middle Panel:* The one-dimensional surface azimuthal magnetic field distribution, taken along the horizontal dashed line in the top two panels. *Bottom Panel:* The one-dimensional surface density distribution, taken along the horizontal dashed line in the top two panels. The vertical dashed line shows the location of the planet.

($n = 1$), the positive torque associated with the magnetic resonances is not strong enough to overcome the negative differential Lindblad torque.

In another example, we considered a disk whose density decreases towards the star, $n = -0.5$. This situation is possible, for example, at the inner edge of the disk where the expanding magnetosphere or erosion of the disk may push the inner disk away from the star (e.g., Lovelace et al. 2008). When $n = -0.5$, the migration rate in the hydrodynamic case is very low (see Fig. 4.2, top panel) because the negative differential Lindblad torque is approximately compensated by the positive corotation torque. For this surface density distribution ($n = -0.5$), the positive torque associated with the magnetic resonances leads to outward migration of the planet, even for a flat magnetic field distribution, $k = 0$ (see Fig. 4.4, bottom panel). For a steeper magnetic field distribution, $k = 1$, the planet migrates outward even more rapidly. It appears, then, that magnetic torques may play a significant role at the disk-cavity boundaries, as well as other regions where the surface density in the disk is flat or decreases towards the star.

We conclude that the rate and direction of migration are determined by the steepnesses of both the magnetic field distribution and the surface density distribution. If the surface density *increases* radially towards the star (e.g., $n = 1$), then the magnetic resonances do not exert enough torque to drive outward migration for any value of k. By contrast, when the surface density in the disk *decreases* toward the star (e.g., $n = -0.5$), the torque from the magnetic resonances is large enough to drive outward migration for different values of k. When the surface density is constant (i.e., $n = 0$), the magnetic resonances drive outward migration when $k = 1, 2$, and inward migration when $k = 0$.

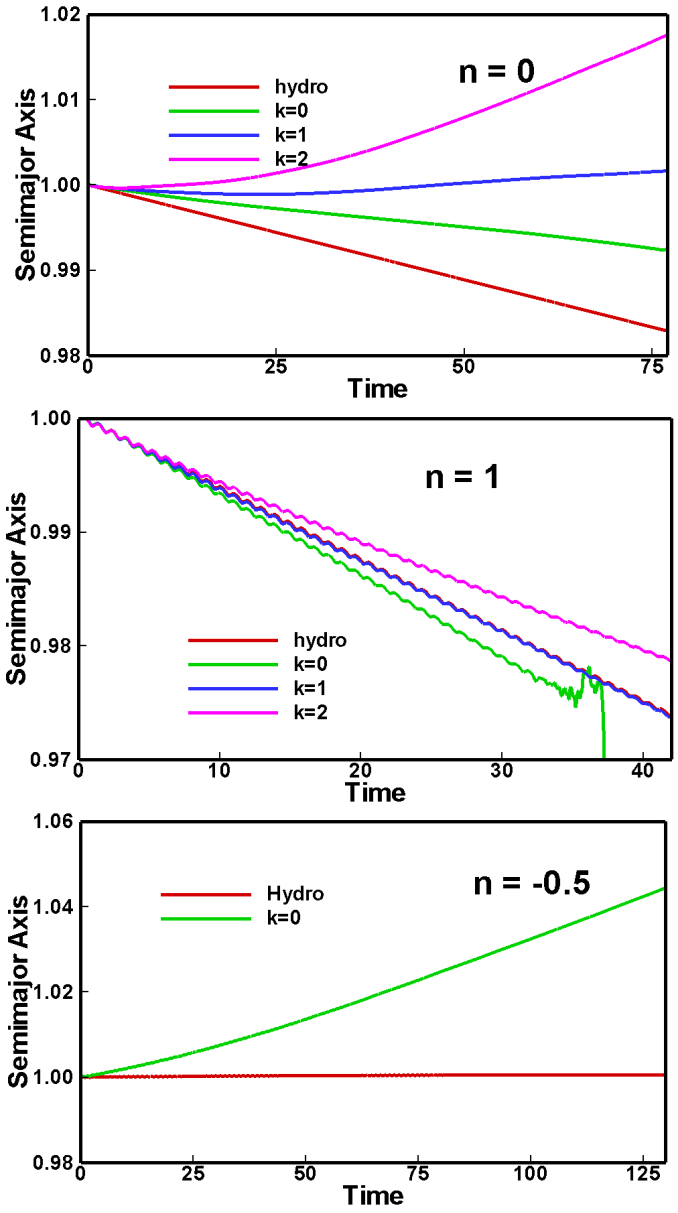

Figure 4.4 Change in semimajor axis versus time for a $5M_{\oplus}$ planet embedded in an MHD disk for different values of k (where $\mathfrak{B} \propto r^{-k}$) and $\beta_i = 2$. The result for a hydrodynamic disk is shown for reference. *Top Panel:* Result shown for $n = 0$, corresponding to models H5n0r1, M5n0k0β2r1, M5n0k1β2r1, and M5n0k2β2r1. *Middle Panel:* Result shown for $n = 1$, corresponding to models H5n1r1, M5n1k0β2r1, M5n1k1β2r1, M5n1k2β2r1. *Bottom Panel:* Result shown for $n = -0.5$, corresponding to models H5n-0.5r1 and M5n-0.5k0β2r1.

4.3.3 Migration of a $20M_\oplus$ planet

The above analysis shows that the effect of an azimuthal magnetic field on a planet's migration strongly depends on both the surface density and magnetic field distributions in the disk. It is also interesting to investigate whether the magnetic resonances also depend on the mass of the planet. To investigate this issue, we simulated the migration of a $20M_\oplus$ planet in a magnetized disk with a flat surface density distribution ($n = 0$) and different steepnesses in the distribution of the magnetic field ($k = 0, 1, 2$). Fig. 4.5 (top panel) shows that, for a constant magnetic field in the disk, $k = 0$, the migration rate is slower than in the hydrodynamic case. For a steeper magnetic field distribution, $k = 1$, the inward migration is even slower, and the direction of the migration reverses at an even steeper field distribution, $k = 2$. These results are in general agreement with those obtained for a smaller-mass planet: the magnetic resonances are strong enough to reverse the migration. Note that, at $k = 2$, the outward migration of the more massive planet is much faster than the migration of the lower-mass planet.

However, longer simulation runs have shown that, for a $20M_\oplus$ planet, the laminar stage of the disk does not last long, $\lesssim 10 - 40$ planetary orbits. At later times, the disk becomes turbulent. Fig. 4.5 (bottom panel) shows that, after a relatively brief stage of slow migration in the laminar disk, the migration becomes stochastic in the turbulent disk. We also see such a transition to stochastic migration for a $5M_\oplus$ planet, though at much later times ($t_{\rm turb} \approx 80$ when $n = 0$, $k = 0$, and $\beta_i = 2$). In both cases, the disk becomes turbulent, and the semimajor axis varies in time stochastically due to the planet's interaction with turbulent cells in the disk.

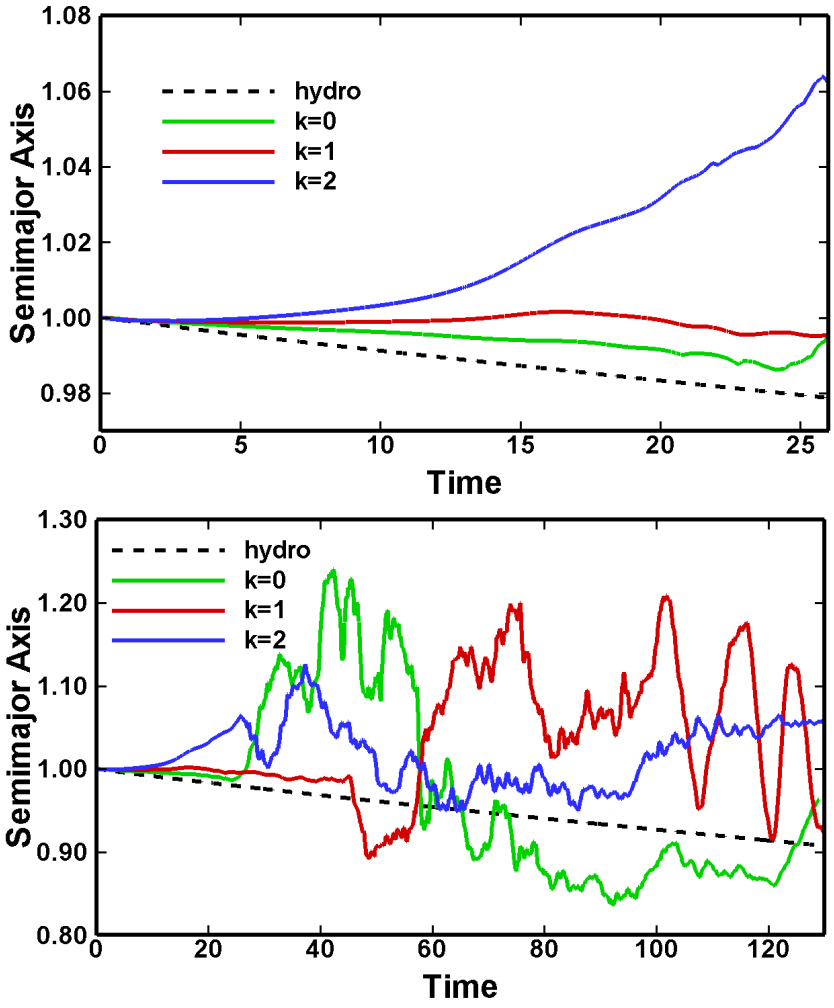

Figure 4.5 *Top Panel:* Variation of the semimajor axis of a $20M_{\oplus}$ planet under the influence of Lindblad and magnetic resonances for various values of initial surface magnetic field exponent, k, for the case $n = 0$ and $\beta_i = 2$, corresponding to models M20n0k0β2r1, M20n0k1β2r1, M20n0k2β2r1, and the hydrodynamic case H5n0r1. *Bottom Panel:* Same as in the top panel, but over a longer interval of time.

We found that the observed turbulence is an interesting phenomenon and investigated the migration of planets in turbulent disks. Earlier, such migration was studied by Nelson and Papaloizou (2004) in 3D simulations; they observed that the migration becomes stochastic and the migration rate may be strongly modified or reversed due to interaction with turbulent cells in the disk. In this paper, we performed 2D simulations in polar coordinates, and we see similar stochastic migration of the planet due to interaction with turbulent cells in the disk. While 2D simulations of the MRI are somewhat restricted, they allow us an opportunity to investigate the details of the interaction between the planet and inhomogeneities in the disk. Below, we investigate migration in turbulent disks.

4.4 Migration in Turbulent MHD disks

In this section, we investigate the transition from the laminar to the turbulent disk, the formation of turbulent disks, and the migration of a low-mass $5M_{\oplus}$ planet in disks with different strengths of the magnetic field. According to the theory of the MRI (see Sec. 2.5), instability is expected in magnetized disks with $\beta_i > 1$; that is, in disks in which the Alfvén velocity $v_A = B/\sqrt{4\pi\rho}$ is smaller than the sound speed c_s (e.g., Balbus and Hawley 1991, 1998; Terquem and Papaloizou 1996). Below, we show the results of simulations at different initial values of β_i (see Sec. 4.4.1) and the details of migration in the turbulent disk (see Sec. 4.4.2).

4.4.1 Migration in a turbulent disk with different β_i

We studied the migration of the planet in disks with different initial plasma parameters, $\beta_i = 1, 2, 10, 100$. Fig. 4.6 (left panel) shows that the disk is initially laminar, and the planet migrates smoothly. This period of smooth migration is longest when $\beta_i = 1$ and 2, but it is shorter for $\beta_i = 10$ and even shorter at $\beta_i = 100$. This is understandable, because the magnetic field is more easily tangled by the disk matter when the matter strongly dominates, such as when $\beta_i = 10$ and 100. The right panel of the same figure shows the semi-major axis of the planet at later times. One can see that the disk is still laminar when $\beta_i = 1$. In all other cases, the disk becomes turbulent. Note that the migration often changes direction from inward to outward and vice versa; this reflects the stochastic nature of the migration process in a turbulent disk, as discussed below in Sec. 4.4.2.

4.4.2 Migration in a turbulent disk with $\beta_i = 100$

In this section, we consider the development of the MRI, as well as the migration of a planet in a turbulent disk, in greater detail. As a base, we consider a model where the initial value of plasma parameter is large, $\beta_i = 100$ (model M5n0k0β100), so that the MRI instability starts easily.

We observed that the origin of the radial component of the field, which is required for the instability, is in the fact that the planet excites non-axisymmetric waves in the disk. These waves lead to non-axisymmetric motion of the gas in the disk and, subsequently, to the formation of a radial component of the magnetic field, which is further stretched by the differential rotation in the disk.

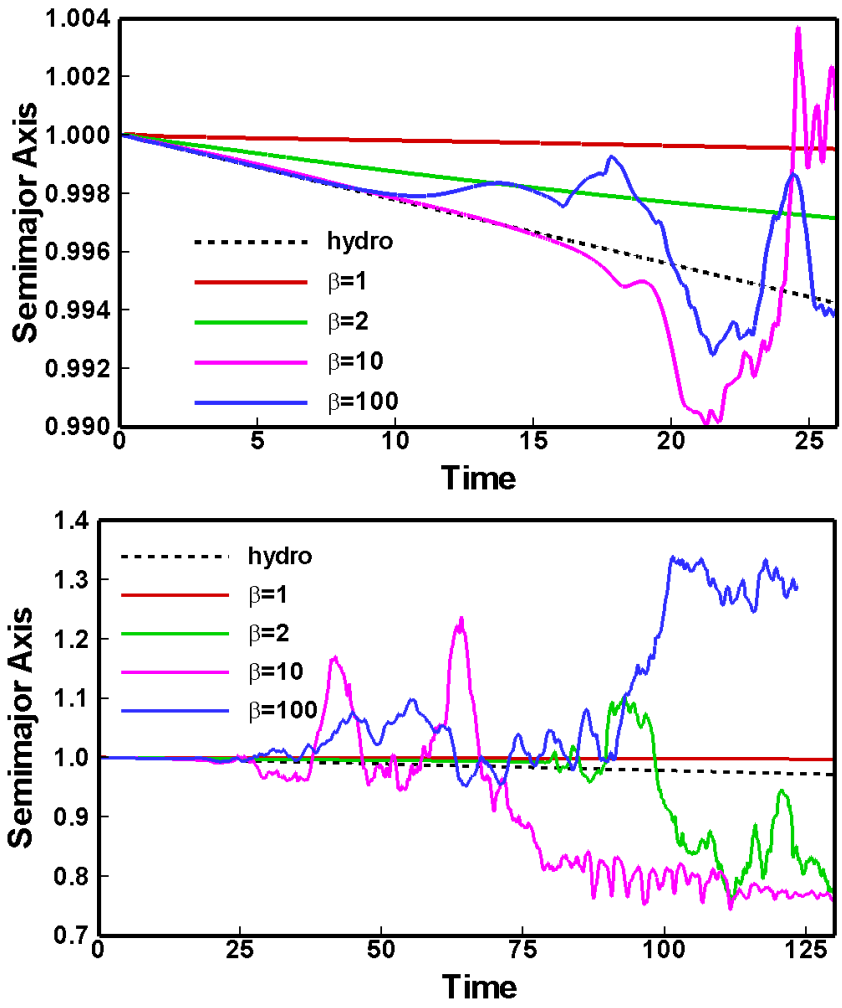

Figure 4.6 *Top Panel:* Variation of the semimajor axis of a $5M_{\oplus}$ planet for in models with different values of β_i when $n = 0$ and $k = 0$, corresponding to models H5n0r1, M5n0k0β1r1, M5n0k0β2r1, M5n0k0β10r1, and M5n0k0β100r1. *Bottom Panel:* Same as in the top panel, but over a longer interval of time.

Fig. 4.7 shows how parts of the initially azimuthal magnetic field near the planet (left panel) acquire a radial component and are subsequently stretched by the differential rotation in the disk, eventually forming a loop (middle panel). Later, this process occurs at larger distances from the planet, many more field lines are stretched in the radial direction (such that different inhomogeneities and loops form), and the disk becomes globally inhomogeneous and turbulent.

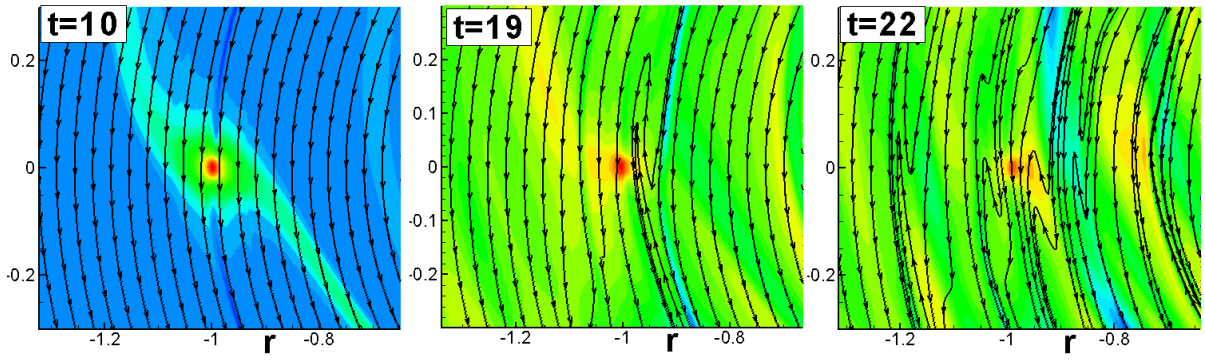

Figure 4.7 Surface density distribution and magnetic field lines corresponding to model M5n0k0β100r1 at $t = 10, 19, 22$. This figure demonstrates how initially-azimuthal field lines (left panel) acquire a radial component from non-axisymmetric matter flow near the planet (density waves) and start forming loops (middle panel). Later on, the process spreads to larger distances from the planet, forming an inhomogeneous distribution of matter and magnetic field in the disk (right panel).

Fig. 4.8 (left panel) shows that the disk consists of azimuthally-stretched turbulent cells. The middle panel of the same figure shows that the total magnetic field, $B_{\rm tot}$, becomes strongly inhomogeneous, with some regions have the original polarity and others reversing polarity. The distribution of the plasma parameter, β_i, shows that the simulation region splits into regions that are either magnetically- or matter-dominated (right panel). Therefore, in the MRI regime, the disk becomes strongly inhomogeneous both in the density and in the magnetic field.

We investigated the density distribution, torque, and semimajor axis evolution of the planet in this case in greater detail. Fig. 4.9 (top panels) shows the surface density distribution in the disk at $t = 5, 40$ and 60. At $t = 5$, the disk is still laminar and two Lindblad density waves are clearly seen. However, after $t \approx 10$, non-axisymmetric motions start to "tangle" the field lines of the weak

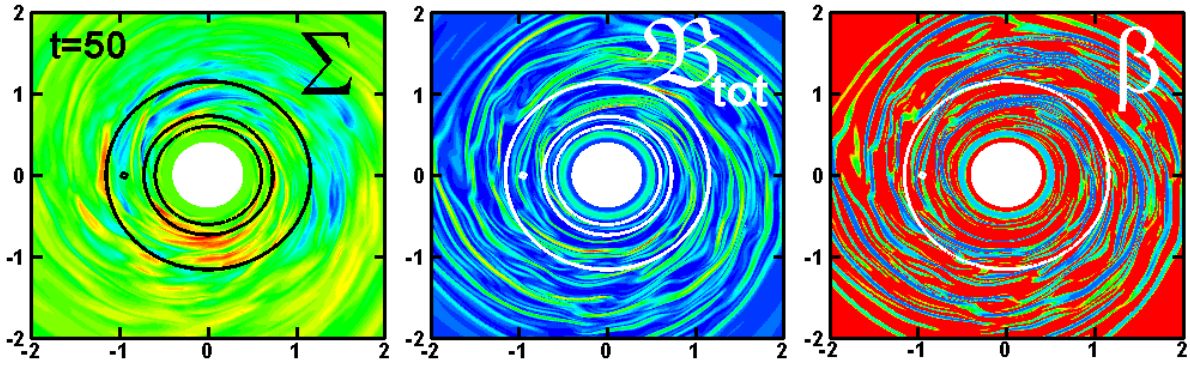

Figure 4.8 Planet migration in an MRI-turbulent disk in the model M5n0k0β100r1 at $t = 50$. *Left Panel:* The surface density variation in the inner part the disk. The planet's location and the $m = 1$ and $m = 2$ Lindblad resonances are shown via the black circles. *Middle Panel:* The variation of the magnetic field magnitude ($B_{\rm tot}$) in the inner part of the disk. The planet's location and the $m = 1$ and $m = 2$ Lindblad resonances are shown via the white circles. *Right Panel:* The variation of the plasma parameter (β_i) in the inner part of the disk. The planet's location and the $m = 1$ and $m = 2$ Lindblad resonances are shown via the white circles.

magnetic field, and an MRI-type turbulence gradually develops. MRI-type turbulence is observed during the time interval $10 \lesssim t \lesssim 60$.

The middle column ($t = 40$) shows small-scale turbulent cells that persist for many orbits. However, later (at $t = 60$), the turbulent cells become larger in size because "islands" of stronger magnetic field also become larger in size, and often one or two main density waves form in the inner parts of the disk. The beginning of this process is seen in the right column of Fig. 4.9. We suggest that the finite life of the MRI turbulence and formation of these larger-scale waves may be connected with the 2D nature of our MRI turbulence. However, the low-amplitude MRI turbulence proceeds over long periods of time, which is sufficient to study the migration of a planet in the turbulent disk. Formation of

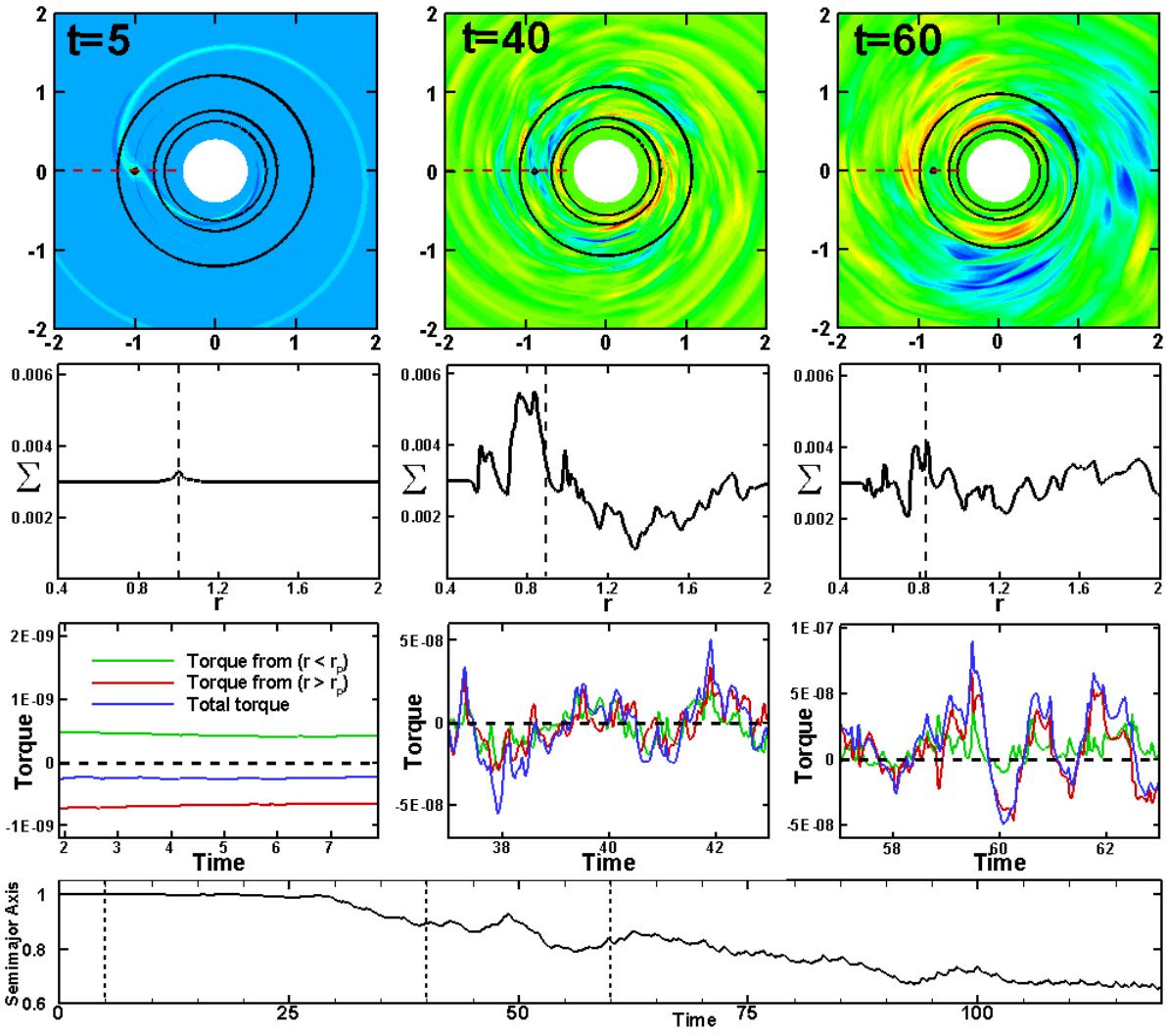

Figure 4.9 Planet migration in the model M5n0k0β100r1 shown for $t = 5, 40, 60$. *Top Panels:* The variation of the surface density (Σ) in the inner part of the simulation region. The location of the planet, and the $m = 1$ and $m = 2$ Lindblad resonances, are shown via the black circles. *Second Row of Panels from the Top:* The one-dimensional variation of the surface density along the red line in the panel above each respective plot. The vertical dashed black line shows the location of the planet. *Third Row of Panels from the Top:* The torques acting on the planet from the disk. The green line shows the torque on the planet from the disk where $r < r_p$, the red line shows the torque on the planet from the disk where $r > r_p$, and the blue line shows the total torque on the planet. The dashed black line marks zero torque. *Bottom Panel:* The change in the semimajor axis of the planet over time.

large-scale waves is possible in realistic disks; we use these waves to study the interaction of a planet with waves in the disk in Sec. 4.5.

The second row in Fig. 4.9 shows the 1D density distribution along the line connecting the planet and the center of the star at the same times as the top row. When the disk is laminar, we see only a small bump in density associated with matter accumulation near the planet. However, as the disk becomes more and more turbulent, larger and larger variations in the surface density of the disk are observed.

The 3rd row in Fig. 4.9 shows the torques acting on the planet at the same times as the top two rows. When the disk is laminar (left column), the planet migrates due to the excitation of density waves at the Lindblad resonances: the inner torque is positive and smaller than the negative outer torque, so that the total torque is negative (the blue line in Fig. 4.9). In this case, the planet slowly migrates inward (see the slow variation of the semimajor axis up to time $t \approx 30$ in the bottom row). However, when the disk is turbulent ($t = 40, 60$), we observe that both the inner and outer torques can be either positive or negative; they both vary rapidly and the resulting torque also changes sign.

The *magnitudes* of these turbulent torques are much larger than those seen in the laminar case (note the torque magnitudes shown on the y-axes in the third row of Fig. 4.9). The torques become stochastic and correspond to the interaction of the planet with individual turbulent cells. The variation of the sign of the net torque shows also that the total averaged torque may be either negative or positive (i.e., that the direction of migration may change). In the shown example, the average total torque is negative and the planet migrates inward overall. Note that, in other cases, the direction of the migration may be

either inward or outward (see, e.g., Fig. 4.5 and Fig. 4.6).

4.5 Interaction between a planet and waves in the disk

The interaction between a planet and turbulent cells in a disk is a complex process. The planet interacts with a set of turbulent cells gravitationally, but the Lindblad density waves are not homogeneous. The closest cell may contribute to the torque more strongly than more remote cells, and the torque becomes more stochastic. Additionally, the planet passes through individual cells, and each cell may exert a corotation torque on the planet. It is difficult to track the interaction of a planet with individual turbulent cells. That is why we developed conditions in which a planet interacts with inhomogeneities (in the form of waves in the disk). We consider two types of waves: (1) low-amplitude ordered waves generated in a hydrodynamic disk by a force at the inner boundary (Sec. 4.5.1), and (2) high-amplitude waves that form at later times in simulations using an MHD disk (Sec. 4.5.2.)

4.5.1 Interaction between a planet and low-amplitude waves in a hydrodynamic disk

To better understand the interaction between a planet and individual turbulent cells, we created a model in which an ordered density wave is generated at the inner disk boundary by a periodic force that decreases with the radius as r^{-3}. This force generates density waves with a small amplitude, for which the density contrast between the wave and the disk is small, about 5 – 7%. The density

wave then propagates through the simulation region. We placed a planet at an initial radius of $r_{\mathrm{p},i} = 2$, away from the action of this force at the boundary.

We observed that the planet moves faster than the wave and it interacts differently with different parts of the wave. Fig. 4.10 (top panels) shows slices of the surface density at $t = 12, 13, 14, 15, 16$. We show the moments when the planet is located at the inner or outer edge of a wave (i.e., where the surface density either decreases or increases toward the star, respectively). The corotation torque is larger than the differential Lindblad torque when the density slope in the disk corresponds to that in Eqn. 2.9; that is, the slope of the density distribution is either positive or only slightly negative toward the star (see Sec. 4.2). This is expected when the planet is at the inner edge of a wave.

The middle row of Fig. 4.10 shows the torques acting on the planet; the times from the top panels marked with vertical dashed lines. The total torque has maxima at $t = 12$ and $t = 15$. The top panels show that, at these moments of time, the planet is located at the inner edge of the wave and, therefore, that the positive torque acting on the planet is the corotation torque (which appears due to the positive density gradient at the inner edge of the wave). The bottom panel of Fig. 4.10 shows that the planet migrates inward overall, because the differential Lindblad torque dominates overall. However, at $t = 12$ and $t = 15$, the planet migrates outward due to the temporarily dominant corotation torque.

At $t = 13$ and $t = 16$, the planet is located at the outer edge of the density wave, where the density increases towards the star. At these moments of time, the total torque is negative and the planet migrates inward. We suggest that, at the outer edge of a wave, a planet excites density waves at the Lindblad resonances, and the differential Lindblad torque drives overall inward migration.

However, when the planet is at the inner edge of the wave, the positive corotation torque is large, and the planet migrates outward.

4.5.2 Interaction between a planet and high-amplitude waves in an MHD disk

In this subsection, we analyze the passage of a planet through waves with much higher amplitudes. These high-amplitude waves often form at later times in simulations of MRI-turbulent disks, where the non-axisymmetry of the gravitational potential leads to the formation of the inner density waves. We chose the model where the initial plasma parameter $\beta_i = 100$ and a planet is placed at $r_{\mathrm{p},i} = 2$. At later moments in time, after the wave forms, the planet migrates to a radius of $r_{\mathrm{p}} \approx 0.9 - 1$. Fig. 4.11 (top panels) shows the density distribution in the wave and the position of the planet for several representative moments in time, where the planet is located at the inner edge of a wave (left and right panels, $t = 180.25, 184.75$), the planet is in the middle of a wave ($t = 181.5$), and the planet is in the low-density region ($t = 183$). The density contrast between the wave and the rest of the disk is $\sim 70\%$, which is about 10 times higher than the low-amplitude waves discussed in the previous subsection.

The middle and bottom rows of Fig. 4.11 show the torques acting on the planet and the variation of the planet's semimajor axis in time. The dashed vertical lines show the four moments in time corresponding to the top four panels. One can see that, at $t = 180.25$, the planet is located at the inner edge of the wave, where the density decreases towards the star, and the positive corotation torque is expected to be larger than the differential Lindblad torque. Indeed, the

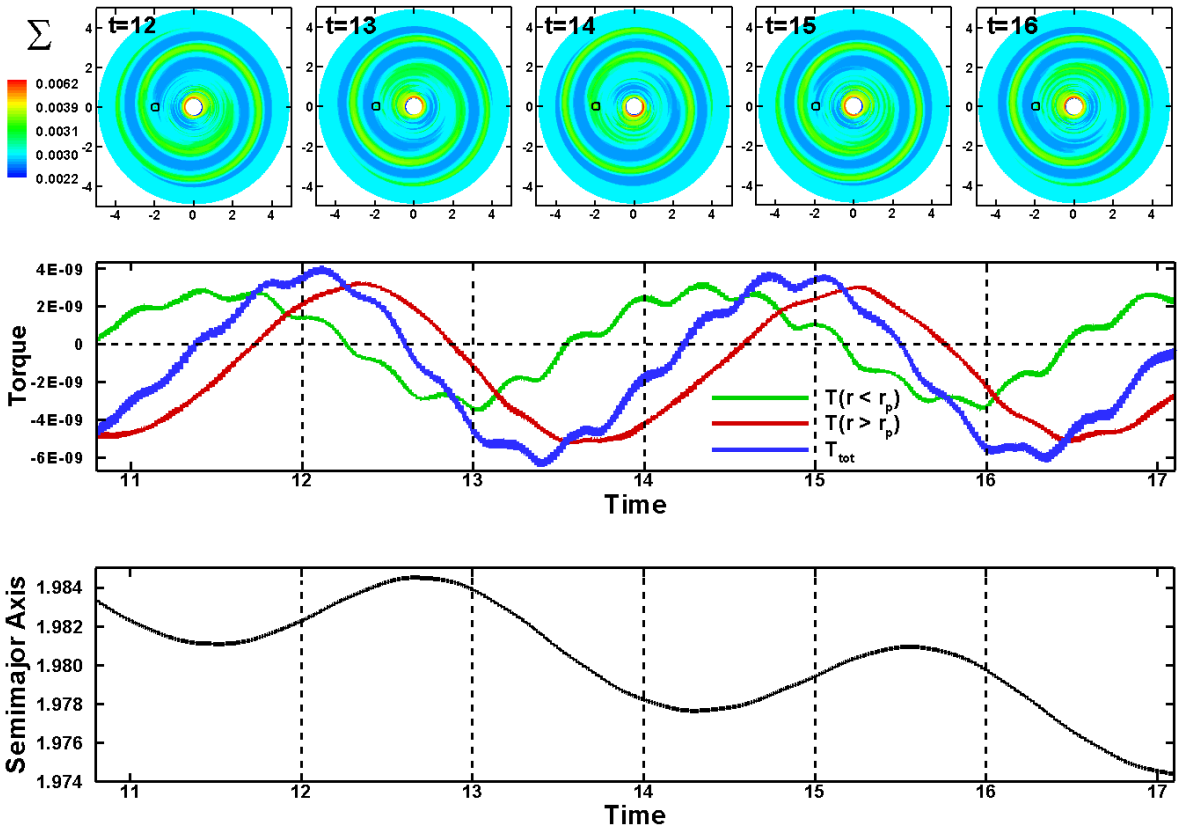

Figure 4.10 Migration of a $5M_{\oplus}$ planet in a hydrodynamic disk in the model W5n0r2, for which low-amplitude ordered density waves are propagated through the disk, at $t = 12, 13, 14, 15, 16$. The bottom two panels mark these times with vertical black dashed lines. *Top Panels:* The surface density (Σ) variation in the disk; the small black circle shows the location of the planet. *Middle Panel:* The torque on the planet from the disk. The green line shows the torque on the planet from the disk where $r < r_p$; the red line shows the torque on the planet from the regions of the disk where $r > r_p$, and the blue line shows the total torque on the planet. The horizontal dashed black line shows zero torque. *Bottom Panel:* The change in the semi-major axis of the planet over time.

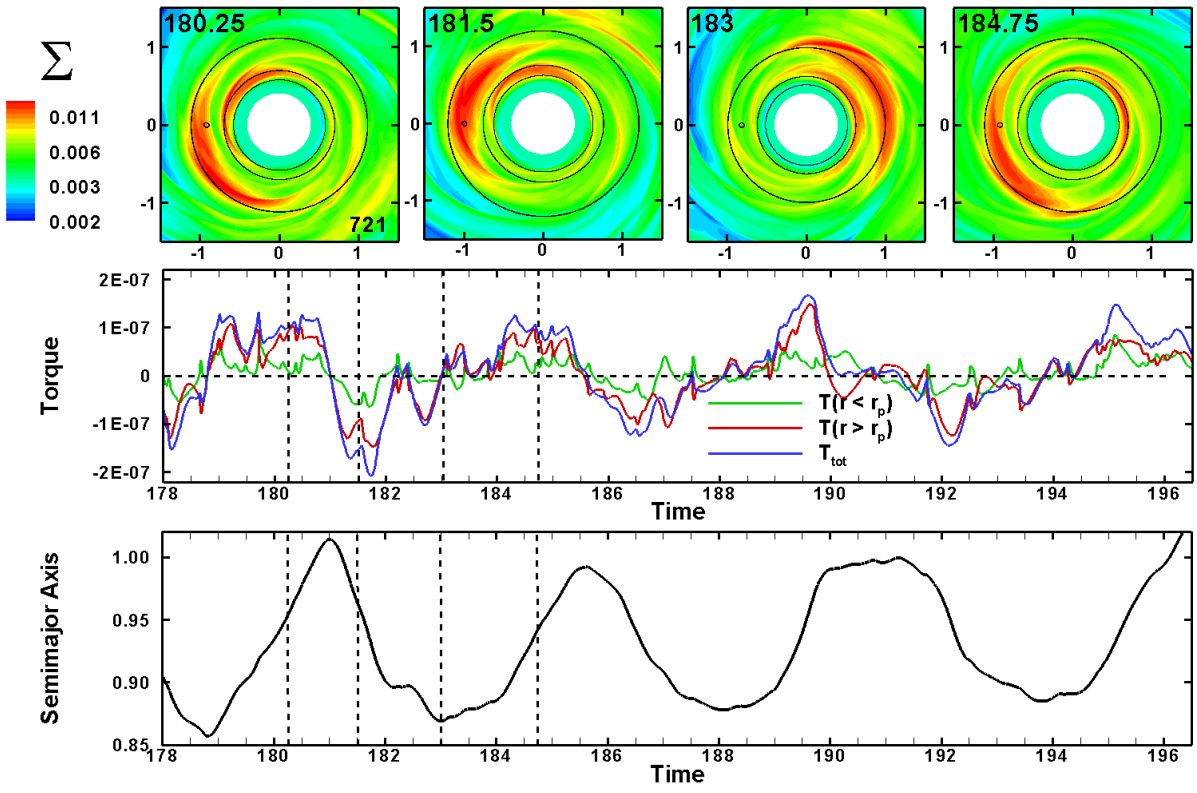

Figure 4.11 Planet migration in high-amplitude waves in the model W5n0k0β100r2 for $t = 180.25, 181.5, 183, 184.75$. In the two bottom panels, these times are shown by vertical black dashed lines. *Top Panels:* Surface density variation in the inner part of the simulation region. The large black circles show the positions of the Lindblad resonances, while the small black circle shows the position of the planet. *Middle Panel:* The torque on the planet from the disk. The green line shows the torque on the planet from the part of the disk where $r < r_p$; the red line shows the torque on the planet from the disk where $r > r_p$. The blue line shows the total torque on the planet. The horizontal dashed black line shows zero torque. *Bottom Panel:* The variation of the semimajor axis of the planet over time.

middle row shows that the total torque is positive at this moment of time, and the planet migrates outward.

At the second moment in time, $t = 181.5$, the planet is located in the middle of the density wave. The middle row shows that, at this moment, a strongly negative torque dominates, and the planet migrates inward. This large negative torque is primarily comprised of the differential Lindblad torque. This torque is proportional to the surface density in the disk, and therefore it is large when the planet is located inside the high-density wave. The positive corotation torque is relatively small. At $t = 183$, the planet is located away from the wave in the low-density part of the disk, and both torques are small. At the last considered moment ($t = 184.75$), the planet is again at the inner edge of the wave, where the corotation torque is positive and larger than the differential Lindblad torque, and the planet migrates outward.

In this example, the density wave is an analog of a large turbulent cell, where the total torque is either positive or negative and acts onto the planet depending on the position of the planet relative to the wave. We expect that the interaction with smaller-sized turbulent cells is similar to the observed interaction with MHD waves, but that the duration of the interaction is shorter. As a result of such interactions, a torque is exerted on the planet during short intervals of time, and the planet's semimajor axis varies stochastically under the action of these torques.

Based on our observations with both the low- and high-amplitude waves we can schematically describe the interaction between a planet and a turbulent cell (see Fig. 4.12). When the planet is at the outer edge cell (the side that is farther from the star), the density is increasing toward the planet ($n > 0$), and so we

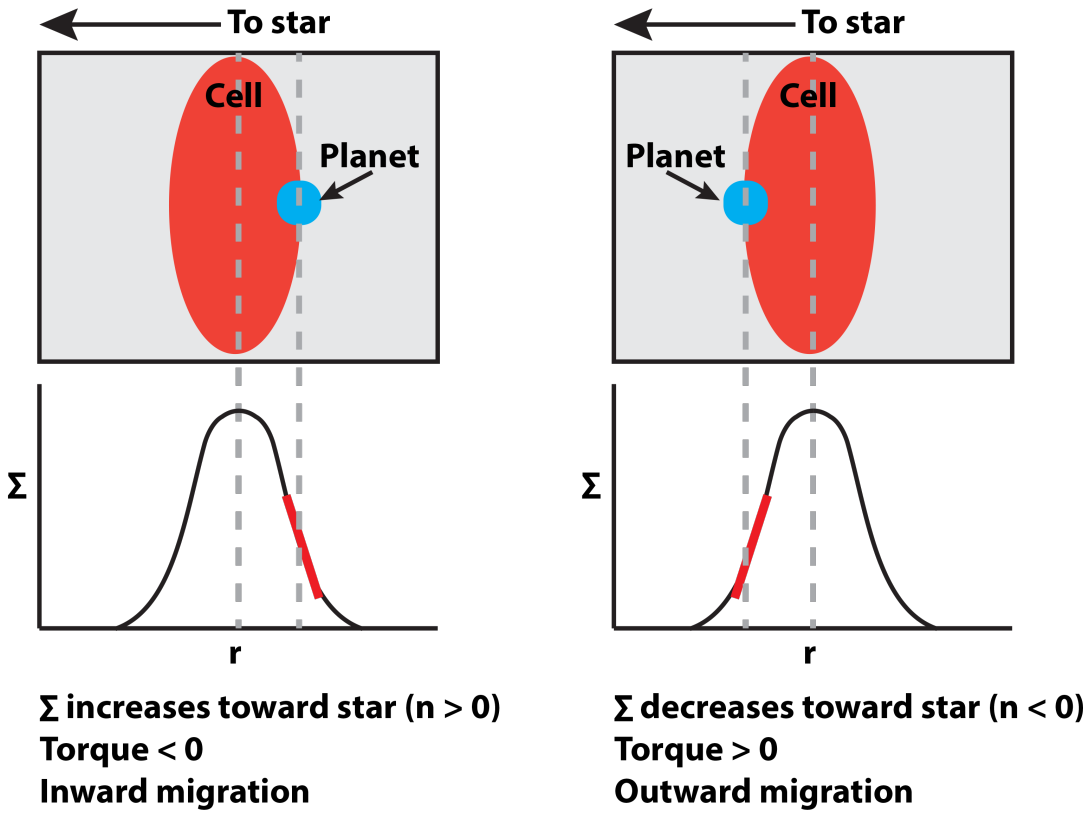

Figure 4.12 Schematic showing the interaction between a planet and a turbulent cell.

expect the torque to be negative and the planet to migrate inward. Conversely, when the planet is on the inner edge of the cell (the side that is closer to the star), the density decreases toward the star ($n < 0$), and so we expect the torque to be positive and the planet to migrate outward. This inward-outward migration does not "trap" the planet, because the cell is moving away from the star, so this is a transient process.

CHAPTER 5

CONCLUSION

We investigated the migration of a low-mass planet ($5M_{\oplus}$) in magnetized disks using a Godunov-type HLLD MHD code in polar coordinates (Koldoba et al. 2015). The initial surface magnetic field is azimuthal, with different radial distributions $B_{\varphi} \sim r^{-k}$, and different strengths determined by the initial plasma parameter at the planet's location, β_i, which varied between $\beta_i = 1$ and 100. We also varied the initial radial surface density distribution in the disk, $\Sigma \sim r^{-n}$. Our main conclusions are as follows:

1. In strongly-magnetized disks ($\beta_i = 1, 2$), and where the density distribution in the disk is flat ($n = 0$), the planet's migration is strongly influenced by magnetic resonances, which are excited near the planet and exert a positive torque on the planet. The migration slows down when the magnetic field distribution is flat ($k = 0$); it slows down more strongly when the magnetic field increases towards the star ($k = 1$); and the migration reverses when the field steeply increases towards the star ($k = 2$). These results are in accord with theoretical predictions by Terquem (2003) and simulations by Fromang et al. (2005).

2. Compared with Fromang et al. (2005), we investigated the effect of magnetic resonances on the migration of a planet in disks with different density distributions. We observed that the steepness of the density distribution strongly influences the rate and direction of the migration. When the density increases towards the star ($n = 1$) the planet migrates inward at any steepness of the magnetic field ($k = 0, 1, 2$) and the effect of the magnetic resonances is negligibly small. This is because, at larger den-

sity steepness, the negative differential Lindblad torque is much larger than the positive corotation or magnetic torques. In the opposite situation, when the density in the disk decreases toward the star ($n = -0.5$), and the positive corotation torque almost balances the negative Lindblad torque, the role of the positive magnetic torque becomes very significant. The planet migrates outward due to magnetic resonances at all values of the magnetic field steepness ($k = 0, 1, 2$).

3. Experiments with a larger mass planet, $20M_{\oplus}$, show that the action of the magnetic resonances is similar to that in the case of a lower-mass planet: the positive torque increases with the steepness of the field, as predicted by the theory. We also observed that, at $k = 2$, the more massive planet migrates outward more rapidly than the lower-mass planet. This is in accord with Eqn. (65) of Terquem (2003), in which the migration time scale is shown to be $\propto M_{\rm p}^{-1}$.

4. We investigated weakly-magnetized disks with initial plasma parameter $\beta_i = 10 - 100$. We observed that non-axisymmetric motions in the disk lead to the formation of a radial component of the magnetic field, its stretching by the differential rotation in the disk, and subsequent MRI-driven turbulence in the disk. Interaction between the planet and turbulent cells leads to stochastic migration, similar to that observed in 3D disks by, e.g., Nelson and Papaloizou (2004). We investigated the transition from the laminar to turbulent disk that often starts near vicinity of the planet, where non-axisymmetric density waves are excited by the planet. The turbulence starts more rapidly when the planet is more massive.

5. The torques acting on the planet are larger in turbulent disks than in laminar disks, leading to more rapid migration. However, the direction of

the migration is also stochastic, and outward migration is frequently observed.

6. To understand how planets interact with individual turbulent cells, we investigated the propagation of a planet through density waves in the disk. We observed that a planet experiences a strong negative torque when it is located inside the wave or at the outer edge of the wave (where the density increases towards the star). However, when the planet is located at the inner edge of the wave (where the density decreases towards the star), then it experiences a positive corotation torque, and it migrates away from the star. We conclude that the stochastic motion of the planet is connected with the alternating action of these positive and negative torques.

There is much room to expand upon this work. Our group has also developed a three dimensional version of this code, albeit with the planetary module only partially complete. Because the MRI is an inherently three dimensional phenomenon, completing development of this 3D version of the code will provide valuable insight into the details of migration in a turbulent MHD disk. Furthermore, the 3D version of the code has the ability to simulate the effect of a tilted magnetosphere on the inner disk: it tends to drive the creation of bending waves. The effects of these bending waves on planet migration has not yet been well studied, although they could potentially increase the inclination of a planet. Finally, our code is able to robustly simulate magnetospheric cavities around stars with varying magnetic field configurations, and studying how planets interact in 3D with these different magnetospheres can provide insight into how planets not only can cross the magnetospheric boundary but also migrate close to the star within the cavity.

BIBLIOGRAPHY

P. Armitage. 2007. arXiv: astro-ph/0701485.

P. Armitage. *Astrophysics of Planet Formation*. Cambridge University Press, Cambridge, 2010.

P. Armitage. *ARA&A*, 49:195–236, 2011.

P. J. Armitage and W. K. M. Rice. In M. Livio, K. Sahu, and J. Valenti, editors, *A Decade of Extrasolar Planets around Normal Stars: Proceedings of the Space Telescope Science Institute Symposium held in Baltimore, Maryland, May 2-5, 2005*, 19, pages 66–83, Cambridge, 2008. Cambridge University Press. arXiv: astro-ph/0507492v2.

S. A. Balbus and J. F. Hawley. *ApJ*, 376:214–222, 1991.

S. A. Balbus and J. F. Hawley. *Rev. Mod. Phys.*, 70:1–53, 1998.

D. Balsara and D. Spicer. *J. Comp. Phys.*, 149:270–292, 1999.

C. Baruteau and F. Masset. *ApJ*, 672:1054–1067, 2008.

C. Baruteau, S. Fromang, R. P. Nelson, and F. Masset. *A&A*, 533:A84–A89, 2011.

G. Basri, G. Marcy, and J. Valenti. *ApJ*, 390:622–633, 1992.

M. Brio and C. Wu. *J. Comp. Phys.*, 75:400–422, 1988.

B. Cockburn, S.-Y. Lin, and C.-W. Shu. *J. Comp. Phys.*, 84:90–113, 1989.

M. Comins, M. Romanova, A. Koldoba, G. Ustyugova, and R. Lovelace. *MNRAS*, 2015. submitted.

W. Dai and P. Woodward. *J. Comp. Phys.*, 111:354–372, 1994a.

W. Dai and P. Woodward. *J. Comp. Phys.*, 115:485–514, 1994b.

S. Dyda, R. Lovelace, G. Ustyugova, M. Romanova, and A. Koldoba. *MNRAS*, 446:613–621, 2015.

E. Feigelson and T. Montmerle. *ARA&A*, 37:363–408, 1999.

S. Fromang, C. Terquem, and R. Nelson. *MNRAS*, 363:943–953, 2005.

B. Fryxell, K. Olson, P. Ricker, F. Timmes, M. Zingale, D. Lamb, P. MacNeice, R. Rosner, J. Truran, and H. Tufo. *ApJS*, 131:273–334, 2000.

W. Fu and D. Lai. *MNRAS*, 410:399–416, 2011.

T. Gardiner and J. Stone. *J. Comp. Phys.*, 205:509–539, 2005.

P. Goldreich and S. Tremaine. *ApJ*, 222:850–858, 1978.

P. Goldreich and S. Tremaine. *ApJ*, 233:857–871, 1979.

P. Goldreich and S. Tremaine. *ApJ*, 241:425–441, 1980.

P. Goldreich and W. W.R. *ApJ*, 183:1051–1062, 1973.

S. Gregory, M. Jardine, C. Gray, and J.-F. Donati. *Rep. Prog. Phys.*, 73:126901, 2010.

J. Guilet, C. Baruteau, and J. C. B. Papaloizou. *MNRAS*, 430:1764–1783, 2013.

K. Gurski. *SIAM J. Sci. Comp.*, 25:2165–2187, 2004.

A. Harten, P. Lax, and B. van Leer. *SIAM Rev.*, 25:35–61, 1983.

F. Hoyle and J. Ireland. *MNRAS*, 120:173–186, 1960.

C. Johns-Krull and J. Valenti. In R. Pallavicini, G. Micela, and S. Sciortino, editors, *Stellar Clusters and Associations: Convection, Rotation, and Dynamos. Proceedings from ASP Conference*, 198, pages 371–380, 2000.

C. Johns-Krull, J. Valenti, and C. Koresko. *ApJ*, 516:900–915, 1999.

S. Kato. *PASJ*, 56:905–922, 2004.

S. Kato. *PASJ*, 59:451–455, 2007.

S. Kato. *PASJ*, 61:1237–1245, 2010.

W. Kley and R. P. Nelson. *ARA&A*, 50:211–249, 2012.

W. Kley, B. Bitsch, and H. Klahr. *A&A*, 506:971–987, 2009.

A. Koldoba, M. Romanova, G. Ustyugova, and R. Lovelace. *ApJ*, 576:L53–L56, 2002.

A. Koldoba, G. Ustyugova, P. Lii, M. Comins, S. Dyda, M. Romanova, and R. Lovelace. *New Astronomy*, submitted, 2015.

Y. Kozai. *AJ*, 67:591–598, 1962.

D. Lai. *ApJ*, 524:1030–1047, 1999.

D. Lai and H. Zhang. *ApJ*, 683:949–956, 2008.

H. Levison, A. Morbidelli, R. Gomes, and D. Backman. *Protostars and Planets V*, volume 951, chapter Planet Migration in Planetesimal Disks, pages 669–684. University of Arizona Press, Tucson, 2007.

S. Li. *J. Comp. Phys.*, 203:344–357, 2005.

M. Lidov. *Planet. Space Sci.*, 9:719, 1962.

P. S. Lii, M. M. Romanova, G. Ustyugova, A. Koldoba, and R. Lovelace. *MNRAS*, 441:86–100, 2014.

D. Lin and S. Ida. *ApJ*, 477:781–791, 1997.

D. Lin and J. Papaloizou. *MNRAS*, 191:37–48, 1980.

J. Lissauer, D. Fabrycky, E. Ford, W. Borucki, F. Fressin, G. Marcy, J. Orosz, J. Rowe, G. Torres, W. Welsh, N. Batalha, S. Bryson, L. Buchhave, D. Caldwell, J. Carter, D. Charbonneau, J. Christiansen, W. Cochran, J.-M. Desert, E. Dunham, M. Fanelli, J. Fortney, T. Gautier, J. Geary, R. Gilliland, M. Haas, J. Hall, M. Holman, D. Koch, D. Latham, E. Lopez, S. McCauliff, N. Miller, R. Morehead, E. Quintana, D. Ragozzine, D. Sasselov, D. Short, and J. Steffen. *Nature*, 470:53–58, 2011.

J. Lissauer, D. Jontof-Hutter, J. Rowe, D. Fabrycky, E. Lopez, E. Agol, G. Marcy, K. Deck, D. Fischer, S. Fortney, J.J.; Howell, H. Isaacson, J. Jenkins, R. Kolbl, D. Sasselov, D. Short, and W. Welsh. *ApJ*, 770:131–145, 2013.

M. Long, M. Romanova, and R. Lovelace. *MNRAS*, 374:436–444, 2007.

M. Long, M. Romanova, and R. Lovelace. *MNRAS*, 386:1274–1284, 2008.

M. Long, M. Romanova, A. Kulkarni, and J.-F. Donati. *MNRAS*, 413:1061–1071, 2011.

Y. Lou, R. Rosner, and P. Ulmschneider. *ApJ*, 315:349–370, 1987.

R. V. E. Lovelace, M. M. Romanova, and A. W. Barnard. *MNRAS*, 389:1233–1239, 2008.

B. Low. *ApJ*, 281:392–412, 1984.

S. Lubow. *ApJ*, 245:274–285, 1981.

G. Marcy, R. Butler, E. Williams, L. Bildsten, J. Graham, A. Ghez, and J. Jernigan. *ApJ*, 481:926–935, 1997.

F. S. Masset and J. Casoli. *ApJ*, 703:857–876, 2009.

F. S. Masset and J. Casoli. *ApJ*, 723:1393–1417, 2010.

M. Mayor and D. Queloz. *Nature*, 378:355–359, 1995.

H. Meheut and M. Tagger. *MNRAS*, 399:794–800, 2009.

A. Mignone, G. Bodo, S. Massaglia, T. Matsakos, O. Tesileanu, C. Zanni, and A. Ferrari. *ApJS*, 170:228–242, 2007.

T. Miyoshi and K. Kusano. *J. Comp. Phys.*, 208:315–344, 2005.

T. Miyoshi, N. Terada, Y. Matsumoto, K. Fukazawa, T. Umeda, and K. Kusano. *IEEE Trans. Plasma Sci.*, 38:2236–2242, 2010.

C. D. Murray and S. F. Dermott. *Solar System Dynamics*. Cambridge University Press, Cambridge, 1999.

R. P. Nelson and J. C. B. Papaloizou. *MNRAS*, 350:849–864, 2004.

S. J. Paardekooper and G. Mellema. *A&A*, 459:L17–L20, 2006.

S. J. Paardekooper and J. C. B. Papaloizou. *A&A*, 485:877–895, 2008.

S. J. Paardekooper, C. Baruteau, A. Crida, and W. Kley. *MNRAS*, 401:1950–1964, 2010.

S. J. Paardekooper, C. Baruteau, and K. W. *MNRAS*, 410:293–303, 2011.

J. Papaloizou and D. Lin. *ApJ*, 285:818–834, 1984.

E. Parker. *ApJ*, 145:811–833, 1966.

F. Rasio and E. Ford. *Science*, 274:954–956, 1996.

M. Romanova, G. Ustyugova, A. Koldoba, and R. Lovelace. *ApJ*, 578:420–438, 2002.

M. Romanova, O. Toropina, Y. Toropin, and R. Lovelace. *ApJ*, 588:400–407, 2003a.

M. Romanova, G. Ustyugova, A. Koldoba, J. Wick, and R. Lovelace. *ApJ*, 595: 1009–1031, 2003b.

M. Romanova, G. Ustyugova, A. Koldoba, and R. Lovelace. *ApJ*, 610:920–932, 2004.

M. Romanova, A. Kulkarni, and R. Lovelace. *ApJ*, 673:L171–L174, 2008.

M. Romanova, G. Ustyugova, A. Koldoba, and R. Lovelace. *MNRAS*, 416:416–438, 2011.

M. Romanova, G. Ustyugova, A. Koldoba, and R. Lovelace. *MNRAS*, 421:63–77, 2012.

M. Romanova, G. Ustyugova, A. Koldoba, and R. Lovelace. *MNRAS*, 430:699–724, 2013.

D. Ryu and T. Jones. *ApJ*, 442:228–258, 1995.

N. I. Shakura and R. A. Sunyaev. *A&A*, 24:337–355, 1973.

M. Skinner and E. Ostriker. *ApJS*, 188:290–311, 2010.

J. Stone and M. Norman. *ApJS*, 80:753–790, 1992a.

J. Stone and M. Norman. *ApJS*, 80:791–818, 1992b.

J. Stone, T. Gardiner, P. Tauben, J. Hawley, and J. Simon. *ApJS*, 178:137–177, 2008.

H. Tanaka, T. Takeuchi, and W. R. Ward. *ApJ*, 565:1257–1274, 2002.

C. Terquem. *MNRAS*, 341:1157–1173, 2003.

C. Terquem and J. Papaloizou. *MNRAS*, 279:767–784, 1996.

C. Terquem and J. Papaloizou. *A&A*, 360:1031–1042, 2000.

E. Toro. *Riemann Solvers and Numerical Methods for Fluid Dynamics: A Practical Introduction*. Springer-Verlag, Berlin, 2009.

G. Tóth. *J. Comp. Phys.*, 161:605–652, 2000.

A. L. Uribe, H. Klahr, M. Flock, and T. Henning. *ApJ*, 736:85–96, 2011.

S. Ustyugov, M. Popov, A. Kritsuk, and M. Norman. *J. Comp. Phys.*, 228:7614–7633, 2009.

G. Ustyugova, A. Koldoba, M. Romanova, and R. Lovelace. *ApJ*, 646:304–318, 2006.

W. R. Ward. *Icarus*, 67:164–180, 1986.

W. R. Ward. *Icarus*, 126:261–281, 1997.

S. Weidenschilling and F. Marzari. *Nature*, 384:619–621, 1996.

J. Wright, O. Fakhouri, G. Marcy, E. Han, Y. Feng, J. Johnson, A. Howard, D. Fischer, J. Valenti, J. Anderson, and N. Piskunov. *PASP*, 123:412–422, 2011.

Y. Wu and N. Murray. *ApJ*, 589:605–614, 2003.